BERICHT

aus dem

INSTITUT FÜR MEERESKUNDE

an der

CHRISTIAN-ALBRECHTS-UNIVERSITÄT KIEL

DOI 10.3289/IFM_BER_216

Nr. 216

A RADIATION BUDGET INDEX AT THE TOP OF THE ATMOSPHERE DERIVED FROM METEOSAT CLIMATE DATA SET

von

Quanhua Liu

Kopien dieser Arbeit können bezogen werden von

Institut für Meereskunde

Abteilung Maritime Meteorologie

Düsternbrooker Weg 20

2300 Kiel 1

ISSN 0341-8561

Diese Arbeit wurde von der Mathematisch-
Naturwissenschaftlichen Fakultät der
Christian-Albrechts-Universität Kiel
als Dissertation angenommen

Abstract

A method is developed to calculate the two components of the radiation budget at the top of the atmosphere: outgoing longwave radiation (OLR) and planetary albedo (α). The basic data to which the method is applied, is the METEOSAT Climate Data Set (CDS). Since OLR and α are planned to be part of the CDS, a fast and simple operational method had to be developed. For the OLR a regression equation is derived with the radiances measured in the IR and WV channels as independent variables. A somewhat different procedure was carried out to derive the shortwave part. Look-up tables were calculated for the broadband radiances and α from standard situations for cloud types which are given by the CDS. For the final estimation of α only the deviations of the actual observations from these mean values are used in approximated equations.

The regression equation and its corresponding coefficients were derived by an analysis of the results of "exact" radiative transfer models: Two-Stream-Approximation for the longwave part without scattering, and a Matrix-Operator-Method for the shortwave part and for the longwave scattering.

In order to test the results a comparative study was performed with the data of ERBE for April 1985. The comparison for the single values of the OLR shows a high correlation (0.98) between the two data sets and a small RMS of 10.0 W/m^2 and a bias of 3.7 W/m^2 (in this report: bias = mean value from CDS - mean value from ERBE). For monthly mean OLR, the RMS is 5.0 W/m^2 and the bias 0.0 W/m^2 for clear cases, and the RMS 6.9 W/m^2 and the bias 4.0 W/m^2 for cloud cases, respectively. Comparison of the single values of the planetary albedo gives a correlation coefficient of 0.94 and a RMS of 4.3% and a BIAS of -0.1%, which is acceptable considering the 10% calibration error for the METEOSAT visible channel and other uncertainties. For the monthly mean planetary albedo we ontained 3.6% absolute or 12% relative deviation and a bias of -2.4%. For a few examples the applicability of the new data is demonstrated: e.g. diurnal variations of the radiative fluxes and cloud radiative-forcing.

Contents

Zusammenfassung

Die vorliegenden Arbeit stellt eine Methode vor mit der die Strahlungsbilanz am Oberrand der Atmosphäre mit den beiden Komponenten planetare Albedo (α) und terrestrische Ausstrahlung (OLR) abgeschätzt werden kann. Die Methode erlaubt es, die Strahlungsflüsse mit einem aus den Beobachtungen des europäischen Satelliten METEOSAT operationell erstellten Klimadatensatz abzuleiten. Da die Strahlungsflüsse selbst Teil des Klimadatensatzes werden sollen, war eine schnelle und operationell anzuwendende Methode zu entwickeln. Die terrestrische Ausstrahlung berechnet sich mit einer Regressionsgleichung, in die die am Satelliten gemessenen Strahldichten im Infrarot- und Wasserdampfkanal eingehen. Die Gleichung basiert auf einer Analyse der Ergebnissen der Zweistromapproximation. Die Methode für die planetare Albedo beruht auf zuvor berechneten Tabellenwerten für Standardsituationen mit den Wolkentypen, die in dem Klimadatensatz gegeben sind. Zur Abschätzung von α werden dann Näherungsgleichungen für die Abweichungen der aktuellen Beobachtungen von den Tabellenwerten benutzt. Die Tabellenwerte werden mit der Matrix-Operator-Methode berechnet. Dieses Modell wurde auch angewandt, wenn im terrestrischen Bereich Streuung berücksichtigt wurde.

Zur Verifikation werden die mit der neuen Methode berechneten Ergebnisse mit denen des Experimentes ERBE (Earth Radiation Budget Experiment) für den April 1985 verglichen. Für die Einzelwerte der terrestrische Ausstrahlung ergibt sich eine hohe Korrelation (0.98) der beiden Datensätze. Der RMS-Fehler beträgt 10.0 W/m^2 und der BIAS 3.7 W/m^2. Für die monatlichen Mittelwerte der OLR für wolkenfreie Gebiete reduziert sich der RMS-Fehler auf 5.0 W/m^2 und der BIAS auf 0.0 W/m^2. Für bewölkte Gebiete erhöht sich der RMS-Fehler nur leicht auf 6.9 W/m^2 und der BIAS auf 4.0 W/m^2 . Ein Vergleich der Einzelwerte der planetaren Albeden liefert einen Korrelationskoeffizienten von 0.94. Der RMS-Fehler von 4.3% und der BIAS von -0.1% sind unter Berücksichtigung des Kalibrationsfehler des sichtbaren Kanals von METEOSAT und anderer Unsicherheiten noch

akzeptabel. Die monatlichen Mittelwerte ergeben 3.6% absolute oder 12% relative Abweichung (RMS) mit einem BIAS von -2.4% . Als Anwendung wird der neue Datensatz zur Berechnung des Tagesganges der Strahlungsflüsse und des "cloud-forcing" herangezogen.

1. Introduction

The radiation budget or energy balance at the top of the atmosphere is defined as the difference between the absorbed solar radiation and the thermal radiation emitted to space. In the solar region between 0.2 and 4.0 μm one has the incident and reflected fluxes, the main contribution of the thermal emission lies between 4.0 and 400 μm. Mathematically, it reads

$$Q = E_o \mu_o - E_{\odot,out} - E_{l,out}$$

$$= E_o \mu_o (1 - \alpha) - E_{l,out} \qquad (1.1)$$

Where Q : net radiation flux or radiation balance index at the top of the atmosphere.

E_o: incoming solar radiation flux at the top of the atmosphere (here E_o = 1357 W/m^2, solar constant).

$E_{l,out}$: outgoing longwave radiation flux (OLR) at the top of the atmosphere.

$E_{\odot,out}$: reflected solar radiation flux at the top of the atmosphere.

α : planetary albedo.

$\mu_o = \cos(\theta_o)$, θ_o : solar zenith angle.

For the earth, being in radiative equilibrium with the energy input from the sun , the globally and annually averaged energy loss through reflected solar and outgoing longwave radiation equals the solar input, that is Q = 0. The nonuniform distribution of the energy gain by solar radiation and of the energy sink by longwave emission leads to Q $\neq$ 0 locally and to energy fluxes in both atmosphere and ocean which determine weather and climate on earth. Thus, monitoring the geographical distribution of sources and sinks of the radiative energy is crucially important for the understanding of the global circulation and their changes on various time scales.

In order to study the radiation budget it is necessary to get a sufficient of amount measurements for all seasons and the whole globe to satisfy sampling requirements. The only way to achieve this at present is by satellites (Barkstrom and Smith, 1986). House et al. (1986) reviewed the satellite missions and measurements performed to determine the earth radiation budget (ERB). The history of ERB measurements closely parallels the overall effort in space technology. The first observations of weather from space were taken in the late 1940s from cameras that viewed the earth from suborbital rockets. Three ERB measurement milestones during the first-generation missions were: Explorer 7 with the first usable ERB data, TIROS* 2, which provided the first scanning radiometer measurements, and TIROS 7, which gave the scientific community the first full year of radiation balance data. In the second-generation missions measurements from research and operational satellites provided global data sets by nonscanning radiometers: the MRIR radiometer on NIMBUS 3 satellite (Raschke and Bandeen, 1970; Raschke et al., 1973; Jacobowitz et al., 1979, 1984) monitored the detailed global radiation balance for 1 year; and scanning radiometers mounted on the operational NOAA and TIROS-N satellites (Gruber and Winston, 1978) yielded combined data sets for 10 years of observations. The third-generation missions since 1975 were the NIMBUS 6 and NIMBUS 7 ERB experiments, which performed a complete monitoring of the radiation balance. Observations included the solar constant and the solar spectrum for 6 years, the angular

* Acronyms and Abbreviations see Annex

distribution of shortwave and longwave radiances as measured by four telescopes operating in biaxial scanning modes for 19 months. The fourth-generation missions was the ERBE in operation from December 1984 to 1990 with the three satellites ERBS + NOAA-9 + NOAA-10; one of its particular aim was to complete our knowledge about the diurnal cycle of ERB. Finally, observations from geostationary platforms are particularly useful, since they provide a regular sample of the atmosphere diurnal cycle over limited areas of the earth.

The state of knowledge of the ERB is given by the following numbers as determined from NIMBUS 7 observations by Jacobowitz et al. (1984) for the time period spanning November 1978 through October 1979: solar constant of about 1371 W m^{-2}, global albedo of 30.6%, LW exitance of 228.8 W m^{-2} , and a net radiation flux of 10.9 W/m^2 from nonscanning measurements. Scanning measurements differ somewhat, indicating a larger albedo of 33.1% and larger LW exitance of 232.7 W/m^2, and a net radiation flux of -3.4 W/m^2 . However, Arking and Vemury (1984) suggested that the procedures of data processing biased the scanning albedo to larger than expected values when compared to the nonscanning values. That means we cannot precisely quantify the greenhouse effect due to the limits of the algorithms, of data sampling problems, and of the present technology.

Many authors have focused on the study of the diurnal cycle of the radiation budget. It is known (Slingo et al., 1987) that a

failure in the diurnal cycle can lead to substantial errors in climate simulations using general circulation models. To cover the sampling requirements for such a study, at least three polar orbiting satellites are needed to determine the diurnal variation of radiation balance components in sufficient detail. Unfortunately, except for a period of three months at the end of 1986, ERBE narrow-field-of-wiew scanner observations have been available from only two satellites at a time (ERBS and NOAA-9 in 1985 and 1986, ERBS and NOAA-10 from October 1986 to May 1989, ERBS only from May 1989 to February 1990 and failure at the present). That gives generally only two or four observations per 24 hours. Over tropical areas where diurnal variations are often strong, geostationary satellites can give much better time sampling, as often as half hour. The European geostationary satellite METEOSAT provides such observations for the African continent, the tropical and subtropical Atlantic ocean, and eastern South America, as well as for Europe. To use METEOSAT observations for the study of radiation balance and its diurnal variation, it is necessary to develop algorithms for the estimation of shortwave and longwave radiation components from the narrowband and single viewing angle observations of METEOSAT. Gube (1982), Kandel and Duvel (1987), Wiegner and Raschke (1987), Rieland (1989), and Schmetz et al. (1990) have already successfully applied METEOSAT data for climate and local diurnal variations studies.

The incentive to this study was to develop a tool operationally applicable to monitor from METEOSAT observations the earth radiation budget components at the top of the atmosphere: outgoing

longwave radiation flux(OLR) and planetary albedo (α). It is recognized that the present generation of operational geostationary satellites suffers from the shortcomings in the calibration and uncertainties related to the conversion of narrowband radiation fluxes to the broadband fluxes. In spite of these limitations the continuity of observations from operational satellites provides a unique tool for studying regional features of the radiation budget and for monitoring interannual variability.

In view of the above mentioned shortcomings we are inclined to call the METEOSAT - derived quantities a " Radiation Budget Index", indicating that it is an estimate rather than direct measurement. However, as comparisons with " state - of - the - art " radiation budget measurements from ERBE (Hartmann et al., 1986) show, there is a good agreement with ERBE. In fact the better diurnal sampling from the geostationary platform suggests that a synergy of both observing systems should be the ultimate goal for a permanent monitoring system.

The structure of the paper is as follows: The second chapter summarizes the radiation transfer models used in this study. Chapter 3 describe the METEOSAT and ERBE data. Chapter 4 outlines the methods for estimating the outgoing longwave radiation flux and the planetary albedo from METEOSAT radiance observations. Chapter 5 contains the important validation of the METEOSAT algorithms by comparisons with ERBE results for April 1985 and chapter 6 illustrates the potential of the METEOSAT observations with some examples. Chapter 7 summarizes the present study and chapter 8 presents suggestions for further work.

2. Radiation transfer models

The outgoing longwave and shortwave radiation fluxes are the integration of the radiances at the top of the atmosphere over all viewing angles. To obtain the fluxes from the radiances at a single viewing angle as given by satellite observations, a statistical method is developed based on regression equations for the OLR and on look-up tables for the reflected shortwave radiation flux (planetary albedo α is the ratio of the reflected shortwave radiation flux and the incoming solar radiation). The regression coefficients are determined from a statistical analysis based on the data from radiation model calculations. The look-up tables are also created from radiation model calculations. In scattering cases the Matrix-Operator-Method (MOM) is used for both the shortwave and the longwave parts. Analytical expressions for the transmission, the reflection, and the internal thermal source function matrices are incorporated into the MOM. A general form of the surface reflection matrix is also incorporated into the MOM in the longwave part. Since information on optical properties of clouds is not available together with METEOSAT data and scattering effects of aerosols and molecules can be neglected in the longwave part, a non-scattering radiation model is used to determine the regression coefficients. The MOM is used in the longwave part only for the purpose of an error analysis and sensitivity tests for cloudy cases.

2.1 A model for the longwave flux

The radiative transfer model(RTM) used here is a non-scattering narrowband model developed by Schmetz (1986). For a non-scattering horizonally homogeneous atmosphere which is in local thermodynamic equilibrium, the upward radiance at the top of the atmosphere can be written as

$$R(0,\theta) = B(T_s)\,\tau(P_s,\theta) + \int_0^{P_s} B(T(p))\,\frac{\partial\,\tau\,(p,\theta)}{\partial\,p}\,d\,p \qquad (2.1.1)$$

with surface emissivity $\varepsilon = 1$.

Where $\tau(p,\theta)$ is the transmittance of the atmosphere between the top of the atmosphere and the pressure level p, θ is the satellite viewing zenith angle relative to the surface, B the Planck function dependent on temperature T, and the index s denotes the values at the earth surface. The outgoing longwave radiation flux (OLR) can be calculated according to its definition:

$$F = 2\,\pi \int_0^{\pi/2} R(0,\theta)\,\cos(\theta)\,\sin(\theta)\,d\,\theta \qquad (2.1.2a)$$

or (see Eq.(19) of Liu and Schmetz, 1988)

$$F = B(T_s)\,D(t_s,q) + \int_0^{P_s} B(T(p))\,\frac{\partial\, D\,(t,q)}{\partial\, p}\,d\,p \qquad (2.1.2b)$$

where

$$D(t,q) = \exp[-q(t)\,t]$$

$$= 2\,\pi \int_0^{\pi/2} \exp(-t/\cos(\theta)\,)\,\sin(\theta)\,\cos(\theta)\,d\,\theta \qquad (2.1.3)$$

is known as the diffuse transmission function, t is the optical depth and q the diffusivity factor. The diffusivity factor q can be calculated from the following equations (Liu and Schmetz, 1988)

$$q(t) = -\frac{1}{t}\ln\left[-t^2(\Gamma+\ln(t))+(1-t)\,\exp(-t)-\sum_{n=1}^{6}\frac{(-t)^{n+2}}{n\;n!}\right] \qquad (2.1.4)$$

for $t < 1$, and

$$q(t) = 1 + 0.51684/\,t^{0.35882} \qquad (2.1.5)$$

for $t \geq 1$,

with Euler's constant $\Gamma = 0.5772$.

The downward flux at the surface and the outgoing flux at the top of the atmosphere are calculated with these relationships for q, with the constant value q = 1.66, and by an integration method of 5, 6 ... to up to 160 discrete basic points (table 1). Assuming that the last row at table 1 (160 discrete points) gives the

correct results, the accuracies are better than 0.01% using equations 2.14 and 2.15 and better than 0.5% with q = 1.66. The results of the analytical solution are much better than the numerical integration with only a few basic points. Thus the constant value of q is used for the further calculations.

Table 1. Comparison of longwave radiation downward fluxes at the surface and upward fluxes at the top of the atmosphere using a constant diffussivity factor q = 1.66, diffussivity factor function q(t) (see Eqs. 2.1.4-2.1.5) and a discrete integration method. (Flux in unit W/m^2)

	Midlatitude Summer		Tropical Summer Dry	
	Downward	Upward	Downward	Upward
q = 1.66	342.879	286.263	391.815	294.646
q(t)	341.213	286.543	388.590	295.086
5 discrete points	345.251	288.505	392.831	297.047
6 discrete points	343.941	287.768	391.433	296.310
8 discrete points	342.690	287.087	390.134	295.632
10 discrete points	342.132	286.805	389.561	295.335
20 discrete points	341.437	286.644	388.829	295.188
40 discrete points	341.294	286.583	388.677	295.127
80 discrete points	341.230	286.545	388.607	295.089
160 discrete points	341.213	286.535	388.590	295.079

The radiation transfer within a cloudy atmosphere depends on the clouds microphysical and optical properties. Since a true characterization of cloud microphysical properties is nearly impossible, even with a most sophisticated experimental design (Stone et. al.,1990), we assume that water clouds are composed of equivalent spherical particles distributed according to the stratocumulus cloud model of Hansen (1971):

$$n(r) = N_o A r^{6.474} \exp(-1.5899\, r) \qquad (2.1.6)$$

with $n(r)$ in $cm^{-3}\mu m^{-1}$, $A = 0.07318\ \mu m^{-1}$ the normalization constant; N_o is the total number droplets per cm^3. Although r is the droplet radius in μm, the function $r^{6.474} \exp(-1.5899\, r)$ is treated as a dimensionless function. In the thermal infrared radiation, the scattering effects on the radiation field in opaque water clouds are small and can be neglected in most cases (Liu, Simmer and Ruprecht, 1990). Figure 1 shows the vertical distribution of the upward and downward fluxes calculated by the Matrix-Operator-Method. It can be seen that the calculated fluxes without scattering agree almost exactly with those with scattering. Therefore, the scattering effects of water clouds can be neglected. The situation is different for ice clouds. The effects of reflection and scattering of high cirrus clouds can reduce the outgoing longwave radiation up to 20% (Platt and Stephens, 1980). The effects, however, strongly depend on the size distribution of cloud particles and wavelength. The following drop size distribution is typical for high cirrus clouds (Deirmendjian, 1969):

$$n(r) = N_o\ A\ r^{6} \exp(-1.89736 \sqrt{r}) \qquad (2.1.7)$$

with $A = 6.29 \times 10^{-7}\mu m^{-1}$. The mode radius of this distribution is 40 μm . The reflection effect is less than 2% for the thermal radiation region 4 - 40 μm and increases to more than 30% for wavelength larger than 200 μm (Fig. 2).

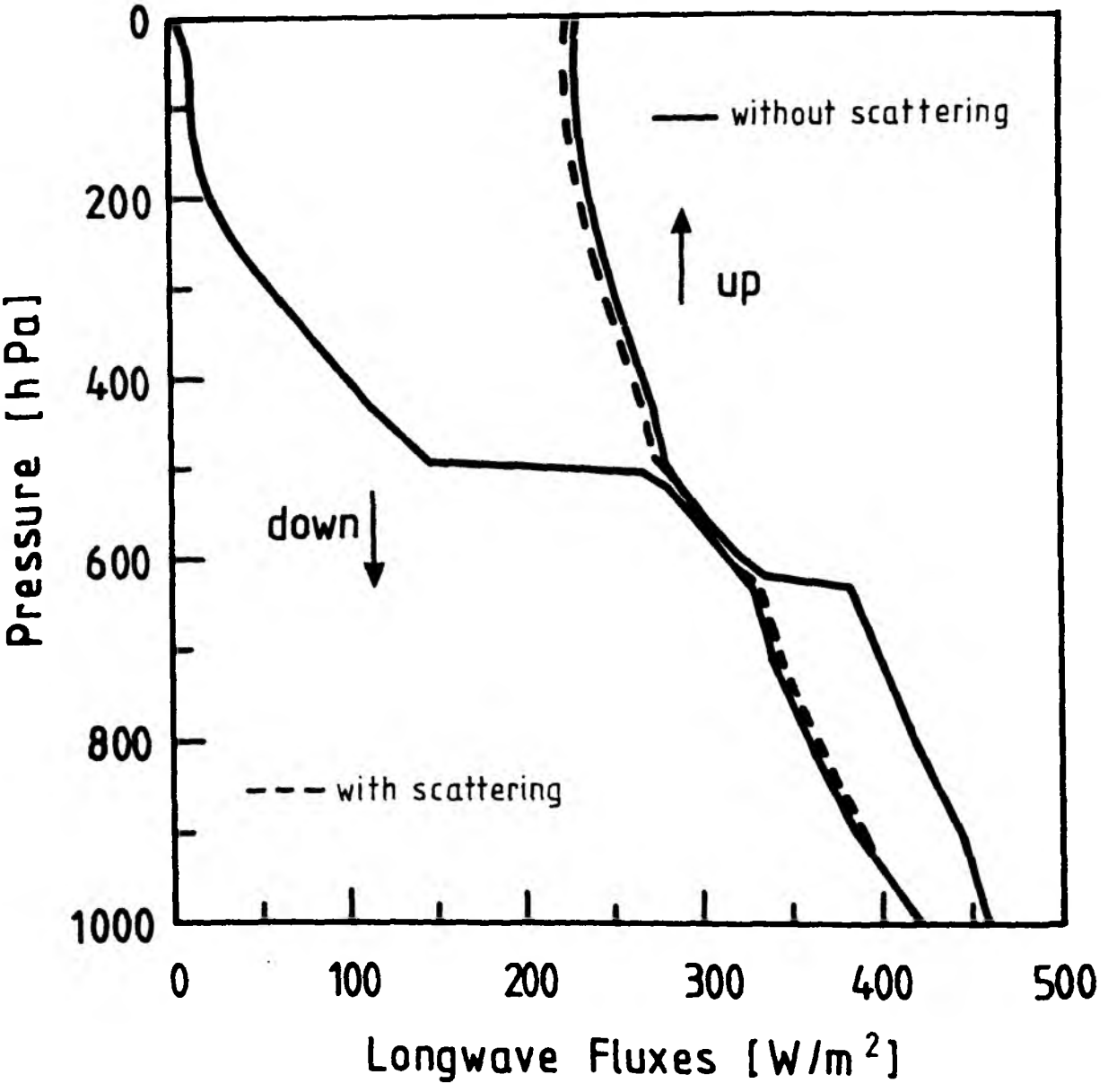

Figure 1. Vertical distribution of the longwave fluxes calculated for a tropical summer, dry stratosphere, standard atmospheric profile with a water cloud layer of spheric cloud particles. The cloud extends from 500 to 630 hPa, the cloud droplet concentration is 500 cm^{-3}.

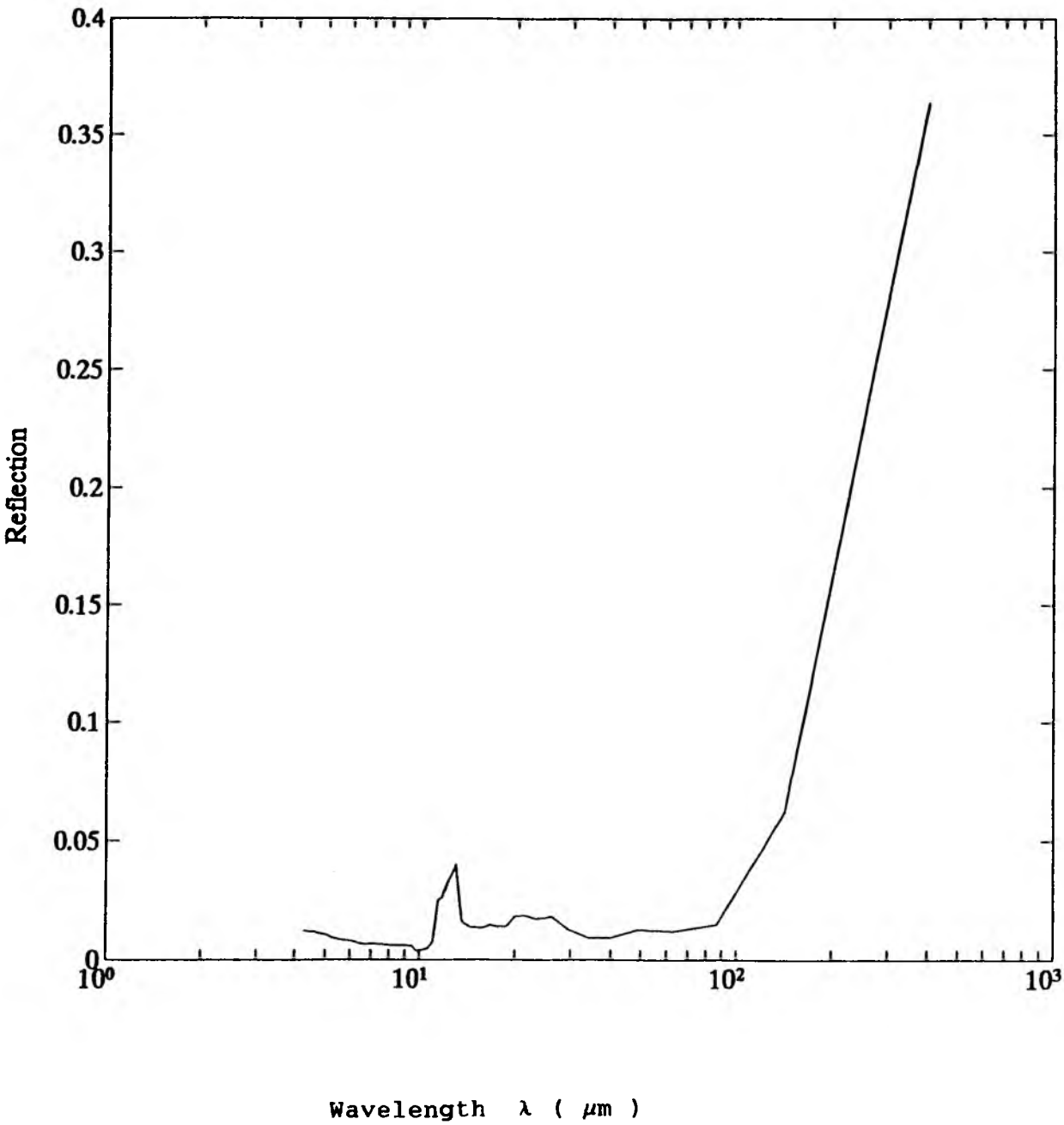

Figure 2. Variation of reflectance of an ice cloud layer with wavelength λ (unit: μm) for particle concentration N_o = 500 cm^{-3} at zenith angle θ = 61 degree. The cloud extends from 183 hPa to 247 hPa.

2.2 Matrix-Operator-Method

The Matrix-Operator-Method is one of the most commonly used methods for solving radiative transfer problems (Plass, et al., 1973; Zdunkowski and Korb, 1985). A description of the MOM and its algorithms can be found in the literature (Fischer and Grassl, 1984; Zdunkowski and Korb, 1985). The extensions , which were incorporated into the MOM (the original programme by Dr. J.Fischer, GKSS, Geesthacht), are described below as well as the algorithms to evaluate the MOM. In the following, the indices for wavelength and Fourier component are omitted. Therefore, all the following formulations are suitable for single Fourier component and single wavelength.

The inhomogeneous atmosphere can be divided into N homogeneous layers (Fig. 3). The upward intensity matrix I_o^+ at the top of the atmosphere and downward intensity matrix I_i^- at level i can be written as

$$\begin{bmatrix} I_o^+ \\ I_i^- \end{bmatrix} = \begin{bmatrix} t_{io} & r_{oi} \\ r_{io} & t_{oi} \end{bmatrix} \begin{bmatrix} I_i^+ \\ I_o^- \end{bmatrix} + \begin{bmatrix} J_{io}^+ \\ J_{oi}^- \end{bmatrix} \qquad (2.2.1)$$

Where t_{io} , t_{oi} are the transmission matrices for the radiances which traverse layer oi from level i to level o, level o to level i, respectively. r_{io} , r_{oi} are the reflection matrices of the layer oi for the radiation which emerges from level i, level o, respectively. J^+_{io} , J^-_{oi} are the thermal source matrices of the layer oi at level o with upward direction, at level i with downward direction, respectively. Eq.(2.2.1) can be rewritten as

$$\begin{bmatrix} I_o^+ \\ I_o^- \end{bmatrix} = \begin{bmatrix} E & -r_{oi} \\ o & t_{oi} \end{bmatrix}^{-1} \left\{ \begin{bmatrix} t_{io} & o \\ -r_{io} & E \end{bmatrix} \begin{bmatrix} I_i^+ \\ I_i^- \end{bmatrix} + \begin{bmatrix} J_{io}^+ \\ -J_{oi}^- \end{bmatrix} \right\} \qquad (2.2.2)$$

Similarly, we have for the other layers ij

$$\begin{bmatrix} I_i^+ \\ I_j^- \end{bmatrix} = \begin{bmatrix} t_{ji} & r_{ij} \\ r_{ji} & t_{ij} \end{bmatrix} \begin{bmatrix} I_j^+ \\ I_i^- \end{bmatrix} + \begin{bmatrix} J_{ji}^+ \\ J_{ij}^- \end{bmatrix} \tag{2.2.3}$$

or

$$\begin{bmatrix} I_i^+ \\ I_i^- \end{bmatrix} = \begin{bmatrix} E & -r_{ij} \\ o & t_{ij} \end{bmatrix}^{-1} \left\{ \begin{bmatrix} t_{ji} & o \\ -r_{ji} & E \end{bmatrix} \begin{bmatrix} I_j^+ \\ I_j^- \end{bmatrix} + \begin{bmatrix} J_{ji}^+ \\ -J_{ij}^- \end{bmatrix} \right\} \tag{2.2.4}$$

E = unity matrix.

Substituting Eq.(2.2.4) into (2.2.2), yields

$$\begin{aligned} \begin{bmatrix} I_o^+ \\ I_o^- \end{bmatrix} = & \begin{bmatrix} E & -r_{oi} \\ o & t_{oi} \end{bmatrix}^{-1} \begin{bmatrix} t_{io} & o \\ -r_{io} & E \end{bmatrix} \\ & \times \begin{bmatrix} E & -r_{ij} \\ o & t_{ij} \end{bmatrix}^{-1} \begin{bmatrix} t_{ji} & o \\ -r_{ji} & E \end{bmatrix} \begin{bmatrix} I_j^+ \\ I_j^- \end{bmatrix} \\ & + \begin{bmatrix} E & -r_{oi} \\ o & t_{oi} \end{bmatrix}^{-1} \begin{bmatrix} t_{io} & o \\ -r_{io} & E \end{bmatrix} \begin{bmatrix} E & -r_{ij} \\ o & t_{ij} \end{bmatrix}^{-1} \begin{bmatrix} J_{ji}^+ \\ -J_{ij}^- \end{bmatrix} \\ & + \begin{bmatrix} E & -r_{oi} \\ o & t_{oi} \end{bmatrix}^{-1} \begin{bmatrix} J_{io}^+ \\ -J_{oi}^- \end{bmatrix} \end{aligned} \tag{2.2.5}$$

On the other hand, for the whole layer oj we have

$$\begin{bmatrix} I_o^+ \\ I_j^- \end{bmatrix} = \begin{bmatrix} t_{jo} & r_{oj} \\ r_{jo} & t_{oj} \end{bmatrix} \begin{bmatrix} I_j^+ \\ I_o^- \end{bmatrix} + \begin{bmatrix} J_{jo}^+ \\ J_{oj}^- \end{bmatrix} \tag{2.2.6}$$

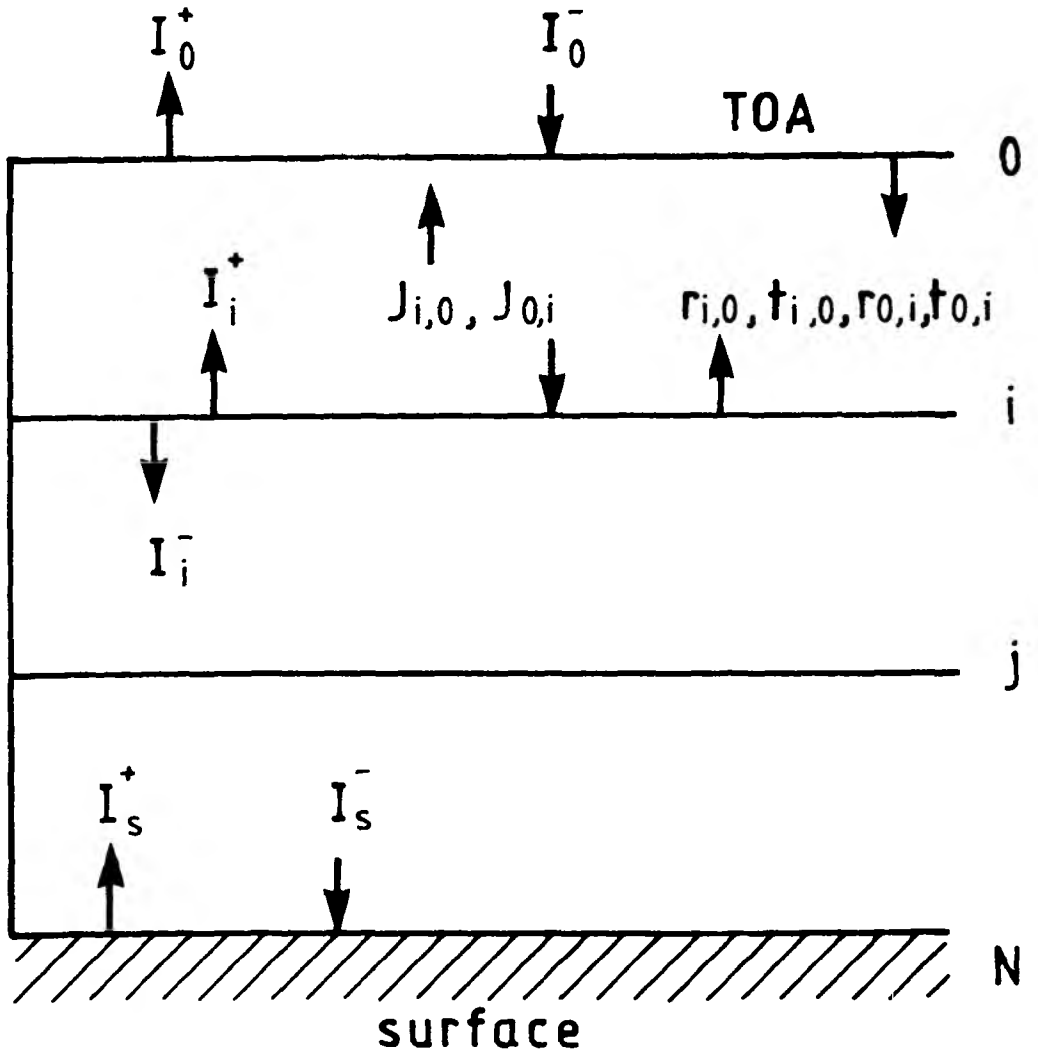

Figure 3. Scheme of the layered atmosphere for the radiation transfer calculation (symbols see text).

or

$$\begin{bmatrix} I_o^+ \\ I_o^- \end{bmatrix} = \begin{bmatrix} E & -r_{oj} \\ o & t_{oj} \end{bmatrix}^{-1} \left\{ \begin{bmatrix} t_{jo} & o \\ -r_{jo} & E \end{bmatrix} \begin{bmatrix} I_j^+ \\ I_j^- \end{bmatrix} + \begin{bmatrix} J_{jo}^+ \\ -J_{oj}^- \end{bmatrix} \right\} \tag{2.2.7}$$

A comparison of the first term of the right side of Eqs.(2.2.7) and (2.2.5) gives

$$r_{jo} = r_{ji} + t_{ij} \left(E - r_{io}\, r_{ij} \right)^{-1} r_{io}\, t_{ji} \tag{2.2.8}$$

$$r_{oj} = r_{oi} + t_{io} \left(E - r_{ij}\, r_{io} \right)^{-1} r_{ij}\, t_{oi} \tag{2.2.9}$$

$$t_{jo} = t_{io} \left(E - r_{ij}\, r_{io} \right)^{-1} t_{ji} \tag{2.2.10}$$

$$t_{oj} = t_{ij} \left(E - r_{io}\, r_{ij} \right)^{-1} t_{oi} \tag{2.2.11}$$

Comparing the second and third terms of Eq.(2.2.5) with the second term of Eq.(2.2.7) gives

$$\begin{bmatrix} J_{jo}^+ \\ J_{oj}^- \end{bmatrix} = \begin{bmatrix} t_{io} \left(E - r_{ij}\, r_{io}\right)^{-1} & o \\ t_{ij} \left(E - r_{io}\, r_{ij}\right)^{-1} r_{io} & E \end{bmatrix} \begin{bmatrix} J_{ji}^+ \\ J_{ij}^- \end{bmatrix}$$

$$+ \begin{bmatrix} E & t_{io} \left(E - r_{ij}\, r_{io}\right)^{-1} r_{ij} \\ o & t_{ij} \left(E - r_{io}\, r_{ij}\right)^{-1} \end{bmatrix} \begin{bmatrix} J_{io}^+ \\ J_{oi}^- \end{bmatrix} \tag{2.2.12}$$

Equations (2.2.8-2.2.12) are also referred to as the star product algorithm (Redheffer, 1962; Zdunkowski and Korb, 1985). The Fourier component of the radiation field at atmospheric level i can be derived from Eqs.(2.2.1) and (2.2.6):

$$\begin{bmatrix} I_i^+ \\ I_i^- \end{bmatrix} = \begin{bmatrix} (E - r_{ij}\, r_{io})^{-1} r_{ij}\, t_{oi} & (E - r_{ij}\, r_{io})^{-1} t_{ji} \\ (E - r_{io}\, r_{ij})^{-1} t_{oi} & (E - r_{io}\, r_{ij})^{-1} r_{io}\, t_{ji} \end{bmatrix} \begin{bmatrix} I_o^- \\ I_j^+ \end{bmatrix}$$

$$+\begin{bmatrix} (E-r_{ij}\ r_{io})^{-1}\ (J^{+}_{ji} + r_{ij}\ J^{-}_{oi}) \\ r_{io}\ (E-r_{ij}\ r_{io})^{-1}\ J^{+}_{ji} + (E-r_{io}\ r_{ij})^{-1}\ J^{-}_{oi} \end{bmatrix} \qquad (2.2.13)$$

By definition of the surface reflection matrix the radiances at the surfaces (index s) are:

$$I^{-}_{s} = R_{so}\ I^{+}_{s} + T_{os}\ I^{-}_{o} + J^{-}_{os} \qquad (2.2.14)$$

$$I^{+}_{s} = \varepsilon_{g}\ B(Ts) + r_{g}\ I^{-}_{s} \qquad (2.2.15)$$

From Eqs.(2.2.14) and (2.2.15), the boundary condition at the surface can be written as

$$I^{+}_{s} = \varepsilon_{g}\ B(Ts) + r_{g}\ (E-R_{so}\ r_{g})^{-1} \times \left\{ R_{so}\ \varepsilon_{g}\ B(Ts) + T_{os} I^{-}_{o} + J^{-}_{os} \right\} \qquad (2.2.16)$$

Where t_{oo} is the unity matrix, r_{oo} and J_{oo} are the null-matrices, ε_{g} is the surface emissivity matrix, it is defined as

$$\varepsilon_{g} = \begin{bmatrix} \varepsilon_1 & & \varepsilon_1 \\ \varepsilon_2 & & \varepsilon_2 \\ . & . & . \\ . & . & . \\ \varepsilon_n & & \varepsilon_n \end{bmatrix} \qquad (2.2.17)$$

with

$$\begin{bmatrix} \varepsilon_1 \\ \varepsilon_2 \\ . \\ . \\ \varepsilon_n \end{bmatrix} = \begin{bmatrix} 1 \\ 1 \\ 1 \\ 1 \\ 1 \end{bmatrix} - r_{g} \begin{bmatrix} 1 \\ 1 \\ . \\ . \\ 1 \end{bmatrix} \qquad (2.2.18)$$

for zeroth Fourier component,

and

$$\varepsilon_{g} = 0, \quad J^{+} = J^{-} = 0 \quad \text{(null-matrix)}$$

for non-zeroth Fourier component.

2.3 Equations for the different boundary conditions and processes used in MOM

In this section a short review is given about radiative processes. The aim of including this section is to describe the equation which are used in MOM and in what form they are used.

2.3.1 Surface reflection factor

For a Lambert surface the reflected radiation field is isotropic. The surface reflection factors with a surface albedo ω_g are

$$r_g = \frac{\omega_g}{\pi} \qquad (2.3.1.1)$$

The zeroth Fourier component of the surface reflection matrix can then be calculated as

$$r_g^o = 2\,\omega_g \begin{bmatrix} 1 & 1 & . & 1 \\ 1 & 1 & . & 1 \\ . & . & . & . \\ 1 & 1 & . & 1 \end{bmatrix} \begin{bmatrix} c_1\,\mu_1 & & & \\ & c_2\,\mu_2 & & \\ & & . & \\ & & & c_n\,\mu_n \end{bmatrix} \qquad (2.3.1.2)$$

or to compensate for the error of the discrete integration:

$$r_g^o = \omega_g\, A^* \begin{bmatrix} 1 & 1 & . & 1 \\ 1 & 1 & . & . \\ . & . & . & . \\ 1 & 1 & . & 1 \end{bmatrix} \begin{bmatrix} c_1\,\mu_1 & & & \\ & c_2\,\mu_2 & & \\ & & . & \\ & & & c_n\,\mu_n \end{bmatrix} \qquad (2.3.1.3)$$

with

$$(A^*)^{-1} = \sum_{i=1}^{n} c_i\,\mu_i$$

and μ_i, quadrature points; c_i, integration weights.

Surfaces with reflection factors departing from ω_g/π are called anisotropic surfaces. Nearly all surfaces have a strong anisotropic behaviour at large viewing zenith angles and large sun zenith angles. Some fundamental measurements over vegetated land have been made. Their results will be used here, but this data set is far from being complete (e.g. Koepke and Kriebel, 1978; Kriebel, 1979;

Eaton and Dirmhirn, 1979) . For the ocean surface, we adopt the reflection model of Ulaby et al. (1986) in which the probability of occurence of a wave slope follows a Gaussian distribution . The surface reflection model is assumed to be the Fresnel model under stationary-phase approximation. In order to take into consideration the anisotropic geometry of the sea surface, the model is generalized to allow for different rms slopes along the upwind and downwind directions. Thus, if we choose the y-axis in the upwind direction, the unpolarized surface reflection factor averaged over the x and y components depends on the relative azimuth angle rather than absolute azimuth angle, and takes the form

$$r(\hat{n}_s, \hat{n}_i) = \frac{q^2 U^2}{g^2 q_z^4 \cos(\theta)} \exp\left[-\frac{q_x^2 + q_y^2}{2 g^2 q_z^2}\right] \qquad (2.3.1.4)$$

with the scattering direction

$$\hat{n}_s = \hat{x} \sin(\theta_s) \cos(\phi_s) + \hat{y} \sin(\theta_s) \sin(\phi_s) + \hat{z} \cos(\theta_s)$$

and the incident direction

$$\hat{n}_i = \hat{x} \sin(\theta) \cos(\phi) + \hat{y} \sin(\theta) \sin(\phi) + \hat{z} \cos(\theta)$$

$\hat{x}$, $\hat{y}$, $\hat{z}$ = unit in vectors in the x, y, z directions

g is calculated according to Cox and Munk(1954) for sea model without foam.

$$g^2 = g_x^2 + g_y^2$$

$$g_x^2 = 0.003 + 0.00192\ u + 0.002$$

$$g_y^2 = 0.00316\ u + 0.004$$

u is the surface wind speed at 12.5 m above sea in m/s . In the present calculation, we select u = 5 m/s. For the parameters U and q we refer to the work of Ulaby et al. (1986). For desert, the surface reflection factors are not available. The Lambert surface is adopted for the desert surface and bare land.

2.3.2 Boundary condition at top of the atmosphere

The solar radiation reaching the top of the atmosphere can be treated as unidirectional. The solar downward flux at top of the atmosphere is

$$S = So\ \mu o = So\ \cos(\theta o) \qquad (2.3.2.1)$$

where So is the solar constant, θo the sun zenith angle. The downward radiance $I\bar{o}(\mu,\phi;\mu o,\phi o)$ at the top of the atmosphere can be expressed as

$$I\bar{o}\ (\mu,\phi;\mu o,\phi o) = So\ \delta(\mu-\mu o)\ \delta(\phi-\phi o) \qquad (2.3.2.2)$$

and can be calculated according to (Simmer, 1987)

$$S = So\ \mu o = \int_0^{2\pi}\int_0^1 I\bar{o}(\mu,\phi;\mu o,\phi o)\ \mu\ d\ \mu\ d\ \phi \qquad (2.3.2.3)$$

Where $\delta(\mu-\mu o)$ and $\delta(\phi-\phi o)$ are the delta function. The delta function $\delta(\mu-\mu o)$ can be approximately expressed as

$$\delta(\mu-\mu o) = \frac{1}{|d\mu|}\,\delta\mu\mu o = \frac{1}{Co}\,\delta\mu\mu o \qquad (2.3.2.4)$$

with zenith angle integration weight Co, and

$$\delta\mu o\,\mu o = 1, \qquad \delta\mu\mu o = 0 \text{ for } \mu \neq \mu o.$$

Thus Eq.(2.3.2.2) can be rewritten as

$$I\bar{o}\ (\mu,\phi;\mu o,\phi) = So\ \frac{1}{Co}\,\delta\mu\mu o\ \delta(\phi-\phi o) \qquad (2.3.2.5)$$

Expanding $I\bar{o}(\mu,\phi;\mu o,\phi o)$ in a Fourier series

$$I\bar{o}\ (\mu,\phi;\mu o,\phi o) = \sum_{m=0} I\bar{o}_m\ (\mu,\mu o)\ \cos m(\phi-\phi o) \qquad (2.3.2.6)$$

we get its Fourier component in a matrix form

$$I^{-}_{om} = \frac{So}{(1+\delta om)\ \pi} \begin{bmatrix} c_1 & & & 0 \\ & c_2 & & \\ & & \ddots & \\ 0 & & & c_n \end{bmatrix}^{-1} \qquad (2.3.2.7)$$

2.3.3 Scattering and absorption by particles

Mie scattering is electromagnetic scattering by spheric particles. The exact solution to the scattering problem for a sphere of radius r at wave length λ was given by Mie in 1908 and elaborated by Debye in 1909. A details description of Mie theory is referred to Van de Hulst's (1957) and Liou (1980).

The intensity function for the perpendicular and parallel components can be respectively written as

$$i_1(\theta) = | s_1(\theta) |^2 \qquad (2.3.3.1)$$

$$i_2(\theta) = | s_2(\theta) |^2 \qquad (2.3.3.2)$$

With

$$s_1(\theta) = \sum_1^{\infty} \frac{2n+1}{n(n+1)} \left[a_n\ \pi_n(\cos\theta) + b_n\ \tau_n(\cos\theta) \right] \qquad (2.3.3.3)$$

$$s_2(\theta) = \sum_1^{\infty} \frac{2n+1}{n(n+1)} \left[b_n\ \pi_n(\cos\theta) + a_n\ \tau_n(\cos\theta) \right] \qquad (2.3.3.4)$$

where $$\pi_n(\cos\theta) = \frac{1}{\sin\theta} P^1_n(\cos\theta) \qquad (2.3.3.5)$$

$$\tau_n(\cos\theta) = \frac{d}{d\theta} P^1_n(\cos\theta) \qquad (2.3.3.6)$$

here P^1_n : Legendre polynomial defined as

$$P_n^1 = \frac{(1-\mu^2)^{1/2}}{2^n n!} \frac{d^{n+1}}{d\mu^{n+1}} (\mu^2 - 1)^n \qquad (2.3.3.7)$$

($\mu = \cos\theta$)

Their recurrence formulations are

$$\pi_n(\cos\theta) = ((2n-1)\ \mu\ \pi_{n-1} - n\ \pi_{n-2})/(n-1) \qquad (2.3.3.8)$$

and

$$\tau_n(\cos\theta) = \frac{d}{d\theta} P_n^1 = -\sin\theta \frac{d}{d\mu} P_n^1 = -\sin\theta \left[\frac{d}{d\mu}(\sin\theta \frac{d}{d\mu} P_n\right]$$

$$= -\sin^2\theta \frac{d^2}{d\mu^2} P_n + \cos\theta \frac{d}{d\mu} P_n = -P_n^2 + \frac{\cos\theta}{\sin\theta} P_n^1$$

$$= -P_n^2 + \cos\theta\ \pi_n \qquad (2.3.3.9)$$

From Eq.(2.3.3.9) it yields (Abramowitz and Stegun, 1965)

$$\tau_n(\cos\theta) - \tau_{n-2}(\cos\theta) = -(P_n^2 - P_{n-2}^2) + \cos\theta\ (\pi_n(\cos\theta) - \pi_{n-2}(\cos\theta))$$

$$= -(2n-1)\ \sin\theta\ P_{n-1}^1 + \cos\theta\ (\pi_n(\cos\theta) - \pi_{n-2}(\cos\theta))$$

$$= -(2n-1)\ \sin^2\theta\ \pi_{n-1} + \cos\theta\ (\pi_n(\cos\theta) - \pi_{n-2}(\cos\theta))$$

thus

$$\tau_n(\cos\theta)$$
$$= -(2n-1)\ \sin^2\theta\ \pi_{n-1} + \cos\theta\ (\pi_n(\cos\theta) - \pi_{n-2}(\cos\theta)) + \tau_{n-2}(\cos\theta)$$

(2.3.3.10)

Therefore, the functions τ_n and π_n can be obtained from Eqs.(2.3.3.8) and (2.3.3.10) with

$$\tau_o = \pi_o = 0$$
$$\tau_1 = \cos(\theta) \quad , \text{ and } \quad \pi_1 = 1$$

The above calculations need only to be done for scatterings between 0 and 90 degrees. The values for scattering angles between 90 and 180 degrees can be obtained according to

$$\pi_n (\cos(180-\theta)) = (-1)^{n+1} \pi_n (\cos\theta)$$

$$\tau_n (\cos(180-\theta)) = (-1)^{n} \tau_n (\cos\theta)$$

The Mie coefficients a_n and b_n can be calculated from an iterative procedure using the recurssion formula for Bessel function (Deirmendjian, 1969; Quenzel and Müller, 1978). The iterative procedure leads to the expressions

$$a_n = \frac{\left\{ \frac{A_n}{m} + \frac{n}{x} \right\} \mathrm{Re}\{ W_n \} - \mathrm{Re}\{ W_{n-1} \}}{\left\{ \frac{A_n}{m} + \frac{n}{x} \right\} W_n - W_{n-1}} \qquad (2.3.3.11)$$

$$b_n = \frac{\left\{ m\, A_n + \frac{n}{x} \right\} \mathrm{Re}\{ W_n \} - \mathrm{Re}\{ W_{n-1} \}}{\left\{ m\, A_n + \frac{n}{x} \right\} W_n - W_{n-1}} \qquad (2.3.3.12)$$

where

$$W_n = \left\{ \frac{2n-1}{x} \right\} W_{n-1} - W_{n-2} \qquad (2.3.3.13)$$

with

$$W_0 = \sin(x) + i \cos(x)$$

$$W_{-1} = \cos(x) - i \sin(x)$$

and

$$A_n = \left\{ \frac{n}{m\, x} - A_{n-1} \right\}^{-1} - \frac{n}{m\, x} \qquad (2.3.3.14)$$

with

$$A_o = \cot(m\varkappa)$$

Here m is the refractive index of the particles and $\varkappa = \frac{2\pi r}{\lambda}$;

r is the radius of the particles.For the homogeneous and isotropic sphere, the extinction cross section is

$$\sigma_e = \frac{4\pi}{k^2} \mathrm{Re}(s(0)) = \frac{2\pi}{k^2} \mathrm{Re} \sum_1^\infty (2n+1)(an+bn) \qquad (2.3.3.15)$$

where $s(0) = s_1(0) = s_2(0)$. The fact that there is only one s(0) is because of the foward scattering in which the extinction is independent of the state of polarization of the incident light. It should be noted that Eq.(2.3.3.15) is only valid when the sphere is isotropic and homogeneous. Since the geometrical cross section of a sphere with radius r = a is

$$\sigma = \pi a^2$$

The extinction efficiency is defined as

$$Q_e = \frac{\sigma_e}{\pi a^2} = \frac{2}{(ka)^2} \sum_1^\infty (2n+1)\,\mathrm{Re}(an+bn) \qquad (2.3.3.16)$$

Similarly, scattering cross section is defined as

$$\sigma_s = \frac{\pi}{k^2} \int_0^\pi (i_1(\theta) + i_2(\theta)) \sin(\theta) d\theta$$

$$= \frac{2\pi}{k^2} \sum_1^\infty (2n+1)(|an|^2 + |bn|^2) \qquad (2.3.3.17)$$

Scattering efficiency is

$$Q_s = \frac{2}{(ak)^2} \sum_1^\infty (2n+1)(|an|^2 + |bn|^2) \qquad (2.3.3.18)$$

Absorption cross section is represented as

$$a_a = \sigma_e - \sigma_s \qquad (2.3.3.19)$$

Absorption efficiency is written as

$$Q_a = Q_e - Q_s \qquad (2.3.3.20)$$

2.3.4 The scattering phase matrix

The Stokes parameters which determine the state of polarization can be written in following matrix form

$$\begin{bmatrix} I \\ Q \\ U \\ V \end{bmatrix} = \begin{bmatrix} M_{11} & M_{12} & 0 & 0 \\ M_{12} & M_{11} & 0 & 0 \\ 0 & 0 & M_{33} & -M_{34} \\ 0 & 0 & M_{34} & M_{33} \end{bmatrix} \begin{bmatrix} I_o \\ Q_o \\ U_o \\ V_o \end{bmatrix} \qquad (2.3.4.1)$$

and $$M_{11} = \frac{1}{2(kr)^2} \left(s_1(\theta)\, s_1^*(\theta) + s_2(\theta)\, s_2^*(\theta) \right) \qquad (2.3.4.2)$$

$$M_{12} = \frac{1}{2(kr)^2} \left(-s_1(\theta)\, s_1^*(\theta) + s_2(\theta)\, s_2^*(\theta) \right) \qquad (2.3.4.3)$$

$$M_{33} = \frac{1}{2(kr)^2} \left(s_2(\theta)\, s_1^*(\theta) + s_1(\theta)\, s_2^*(\theta) \right) \qquad (2.3.4.4)$$

$$-M_{34} = \frac{1}{2(kr)^2} \left(s_1(\theta)\, s_2^*(\theta) - s_2(\theta)\, s_1^*(\theta) \right) \qquad (2.3.4.5)$$

For unpolarized incident radiation($Q_o = U_o = V_o = o$), equation(2.3.4.1) reduces to

$$I = M_{11}\, I_o = C\, P(\theta)\, I_o \qquad (2.3.4.6)$$

where $P(\theta)$ the normalized phase function which satisfies

$$\int_o^{2\pi} \int_o^{\pi} \frac{P(\theta)}{4\pi} \sin\theta \, d\theta \, d\phi = \frac{1}{2} \int_o^{\pi} P(\theta) \sin\theta \, d\theta = 1 \qquad (2.3.4.7)$$

$$C = \frac{1}{2} \int_o^{\pi} M_{11}(\theta) \sin\theta \, d\theta = \frac{1}{4(kr)^2} \int_o^{\pi} (i_1(\theta) + i_2(\theta)) \sin\theta d\theta$$

$$= \sigma_s \,/\, 4\pi r^2 \qquad (2.3.4.8)$$

Therefore, phase function may be written as

$$P(r,\theta) = \frac{4\pi r^2}{\sigma_s} M_{11}(r,\theta) = \frac{2\pi}{\sigma_s k^2}(i_1(\theta)+i_2(\theta)) \qquad (2.3.4.9)$$

Asymmetry factor g, which is the first moment of the phase function, is defined as

$$g = \frac{1}{2}\int_0^{\pi} \frac{P(\theta)}{4\pi} \cos\theta \sin\theta \, d\theta$$

$$= \frac{4}{(kr)^2 Q_s} \sum_1^{\infty} \frac{n(n+1)}{n+1} \mathrm{Re}(a_n a_{n+1}^* + b_n b_{n+1}^*$$

$$+ \frac{2n+1}{n(n+1)} \mathrm{Re}(a_n b_n^*) \;) \qquad (2.3.4.10)$$

All above formalations are only suitable for a single particle of radius r. For aerosol and clouds, which have a particle distribution of

$$n(r) = \frac{d\,N(r)}{d\,r} \qquad (2.3.4.11)$$

where N(r) the number of particles having radii smaller than r. The volume scattering coefficient is defined as

$$a_s = \pi \int_0^{\infty} Q_s(r)\, n(r)\, r^2\, dr \qquad (\text{unit: } m^{-1}) \qquad (2.3.4.12)$$

The volume extinction coefficient is defined as

$$a_e = \pi \int_0^{\infty} Q_e(r)\, n(r)\, r^2\, dr \qquad (\text{unit: } m^{-1}) \qquad (2.3.4.13)$$

The volume absorption coefficient is represented as

$$a_a = a_e - a_s \qquad (\text{unit: } m^{-1}) \qquad (2.3.4.14)$$

Single scattering albedo is defined as

$$\omega = \frac{a_s}{a_e}$$

The phase function is defined as

$$P(\theta) = \frac{\int_0^\infty n(r)\ \sigma_s(r)\ P(r,\theta)\ dr}{\int_0^\infty n(r)\ \sigma_e(r)\ dr} \qquad (2.3.4.15)$$

2.3.5 Rayleigh scattering

Rayleigh scattering is a non-absorption scattering by very small particles. It is an approximate approach of Mie scattering for small particles. For non-absorption scattering one can expand Mie coefficients with Mie parameter $\varkappa = 2\pi r/\lambda$ as follows (see section 2.3.3)

$$Q_e = Q_s = \frac{8}{3}\varkappa^4 \left[\frac{m^2 - 1}{m^2 + 2}\right]^2 \left[1 + \frac{6m^2 - 1}{5m^2 + 2}\varkappa^2 + \ldots\right] \qquad (2.3.5.1)$$

$$i_1(\theta) = \varkappa^6 \left[\frac{m^2 - 1}{m^2 + 2}\right]^2 + o(\varkappa^6) \qquad (2.3.5.2)$$

$$i_2(\theta) = \varkappa^6 \left[\frac{m^2 - 1}{m^2 + 2}\right]^2 \cos^2\theta + o(\varkappa^6) \qquad (2.3.5.3)$$

For small particles, $\varkappa \ll 1$, or $r \ll \lambda/2\pi$, we have

$$\sigma_s = \pi r^2 Q_s = \frac{128}{3}\pi^5 r^6 \lambda^{-4} \left[\frac{m^2 - 1}{m^2 + 2}\right]^2$$

$$= \frac{128}{3}\pi^5 \alpha^2 \lambda^{-4} \qquad (2.3.5.4)$$

with the polarizability of the particle (Hulst, 1957)

$$\alpha = \frac{3}{4\pi}\frac{m^2 - 1}{m^2 + 2} V \qquad (2.3.5.5)$$

and V, the volume of the particle. For the entire medium, α can be calculated from the Lorentz-Lorenz formula

$$\alpha = \frac{3}{4\pi} \frac{\bar{m}^2 - 1}{\bar{m}^2 + 2} \frac{1}{No} \qquad (2.3.5.6)$$

with $\bar{m}$, the refractive index of the medium, No the total number of molecules. In the solar visible spectrum imaginary parts of refractive indices for air molecules may be neglected in the scattering discussion, while the real part of $\bar{m}$ is close to 1. The approximation of $\bar{m}$ may be written as (Liou, 1980):

$$\bar{m} = 1 + (6432.8 + \frac{2949810}{146 - \lambda^{-2}} + \frac{25540}{41 - \lambda^{-2}}) \times 10^{-8} \qquad (2.3.5.7)$$

$$\alpha = \frac{1}{4\pi\ No} (\bar{m}^2 - 1), \quad (\lambda \text{ in } \mu m \text{ unit }) \qquad (2.3.5.8)$$

Therefore the scattering coefficient for Rayleigh scattering is

$$\sigma_s = \frac{8\pi^3 (\bar{m}^2 - 1)^2}{3 \lambda^4 N^2} \times 1.0608 \qquad (2.3.5.9)$$

A correction factor is included in Eq.(2.3.5.9) to consider the anisotropic property of molecules. The optical depth by Rayleigh scattering between height z_1 and z_2 is

$$\tau(\lambda) = \sigma_s(\lambda) \int_{z_1}^{z_2} N(z)\, dz \qquad (2.3.5.10)$$

By using Eq.(2.3.4.9) we get the phase function for Rayleigh scattering

$$P(r,\theta) = \frac{4\pi r}{\sigma_s} M_{11}(r,\theta) = \frac{2\pi}{\sigma_s k^2} (i_1(r,\theta) + i_2(\theta))$$

$$= \frac{3}{4} (1 + \cos^2 \theta) \qquad (2.3.5.11)$$

2.3.6. Calculations of transmission, reflection and thermal radiative source matrices

The overall reflection matrix R and transmission matrix T can be derived from the reflection matrix r and transmission matrix t of the single homogeneous atmospheric layers. The two are calculated by an analytical expression (Liu, 1990)

$$t = 2\,[\,ch(H\tau)-Vsh(H\tau)+ch(F\tau)-Ush(F\tau)\,]^{-1} \qquad (2.3.6.1)$$

$$r = -\frac{1}{2}\,[\,ch(H\tau)+Vsh(H\tau)-ch(F\tau)-Ush(F\tau)\,]^{-1}\ t \qquad (2.3.6.2)$$

where $sh(x) = 1/2\,\{\exp(x)-\exp(-x)\}$

$ch(x) = 1/2\,\{\exp(x)+\exp(-x)\}$

$$U = (\alpha_1 - \alpha_2)\,F^{-1}$$

$$V = (\alpha_1 + \alpha_2)\,H^{-1}$$

$$F^2 = (\alpha_1 + \alpha_2)\,(\alpha_1 - \alpha_2)$$

$$H^2 = (\alpha_1 - \alpha_2)\,(\alpha_1 + \alpha_2)$$

$$\alpha_1 = \omega\, M^{-1} P^{++}\, C - M^{-1}$$

$$\alpha_2 = \omega\, M^{-1} P^{+-}\, C$$

ω the single scattering albedo, P^{++} the forward scattering phase matrix, P^{+-} the backward scattering phase matrix,

$$M = (\mu_i\ \delta_{ij}),\quad C = (C_i\ \delta_{ij}).$$

The analytical expressions(Eqs. (2.3.6.1) and (2.3.6.2)) are suitable for all orders of scattering and any optical depth. For an 8 by 8 matrix form, the computation time by using the analytical expressions is one third of that by using a doubling or adding method.

The thermal radiative source function is the internal contribution from each atmospheric layer to the upward and downward radiation intensity. For an emitting and no scattering homogeneous atmospheric layer, the source function is a product of the Planck function B(T) with the emissivity ε of the atmospheric layer. It reads

$$J = J^{+} = J^{-} = \varepsilon\, B(T) = \{\, 1 - \exp(-\delta/\mu) \,\}\, B(T) \qquad (2.3.6.3)$$

for zeroth Fourier component, and

$$J = J^{+} = J^{-} = 0$$

for non-zeroth Fourier component.

If scattering is included, the analytical expression for the source function within the Matrix-Operator-Method can be written as (Liu, Simmer, and Ruprecht , 1991)

$$J = J^{+} = J^{-} = (E-t-r)\, \{E-\omega\, (P^{++} + P^{+-})\, C\, \}^{-1}\, (1-\omega)\, B(T) \qquad (2.3.6.4)$$

Since the internal source (thermal radiation) is independent of the sun zenith angle and sun/satellite azimuth angle, Eq.(2.3.6.4) can be reduced to

$$J = J^{+} = J^{-}$$

$$= (E-t-r)\, \{E-\omega\, (P^{++} + P^{+-})\, C\, \}^{-1}\, (1-\omega)\, B(T) \begin{bmatrix} 1 & \dots & 1 \\ 1 & \dots & 1 \\ . & \dots & . \\ . & \dots & . \\ 1 & \dots & 1 \end{bmatrix}$$

$$= (E-t-r)\, B(T) \begin{bmatrix} 1 & \dots & 1 \\ 1 & \dots & 1 \\ . & \dots & . \\ . & \dots & . \\ 1 & \dots & 1 \end{bmatrix} \qquad (2.3.6.5)$$

for zeroth Fourier component,

and

$$J = J^{+} = J^{-} = 0$$

for non-zeroth Fourier component.

In the present model, the optical depth δ, the single scattering albedo ω, and the phase function $P(\theta)$ are calculated for each homogeneous atmospheric layer. The optical depth is calculated according to

$$\delta = \{ a + \beta ext + \gamma \} \Delta z = \{ a + \beta sca + \beta abs + \gamma \} \Delta z \quad (2.3.6.6)$$

with a: the sum of the absorption coefficients for the absorbing gases H2O, and CO2, and O3.

β: the sum of the extinction, scattering and absorption coefficients, respectively for aerosols and clouds, if clouds exist.

γ: the Rayleigh scattering coefficient.

Δz: the geometrical thickness of the layer in km.

The single scattering albedo is defined as

$$\omega = \frac{\beta sca + \gamma}{\beta ext + a + \gamma}$$

and the total phase function is defined as weighted mean of the individual phase functions:

$$P(\theta) = \frac{\beta sca(aer)\ Paer(\theta) + \gamma\ Pray(\theta)}{\beta sca(aerosol) + \gamma} \quad (2.3.6.7)$$

for the clear case, and

$$P(\theta) = \frac{\beta sca(aer)\ Paer(\theta) + \gamma\ Pray(\theta) + \beta sca(clo)\ Pclo(\theta)}{\beta sca(aerosol) + \gamma + \beta sca(cloud)} \quad (2.3.6.8)$$

for the cloudy atmosphere.

2.3.7 Aerosol and clouds

Knowledge about the aerosol size distributions has increased over the last few years, since more data have become available covering the entire size range from 0.001 μm to 200 μm in radius.

It was found that the aerosol size distribution showed various modes which are not confined to certain fixed radii as believed earlier; and that the size distribution could be approximated by many different analytical functions. One simple method is to assume a power law size distribution with variable power (Junge, 1963), i.e,

$$n(r) = \frac{d\,N(r)}{d\,r} = A\,r^{\nu} \qquad (2.3.7.1)$$

However, a commonly used expression (WCP - 55, 1983) is a modified Gamma distribution

$$n(r) = \frac{d\,N(r)}{d\,r} = A\,r^{\alpha}\exp(-br^{\nu}) \qquad (2.3.7.2)$$

This distribution has a number of distinct advantages. First it does not require any cut offs. Second, it has been shown experimentally to be a fairly good approximation (Deirmendjian, 1969). Third it has been demonstrated by Kuriyan and Sekera (1974) to be equivalent to the other distribution. Another commonly used size distribution is log-normal distribution, it reads

$$\frac{dN\,(r)}{d(\log r)} = \sum_{i=1}^{3} \frac{1}{\sqrt{2\pi}\,\log(\sigma_i)}\,n_i \exp\left[\frac{-(\log(r)-\log(R_i))^2}{2(\log(\sigma_i))^2}\right] \qquad (2.3.7.3)$$

With n_i being the integral over the individual log-normal distribution, σ_i is the geometric standard deviation, and R_i the geometric mean radius. In the present study, Eq.(2.3.7.2) is used

for a stratospheric aerosol. Continental, marine and desert aerosol size distributions are based on Eq.(2.3.7.3). The Mie-code used here achieved an accuracy of 1% when compared with the results reported in WCP-55 (see table 2). Parameters for the desert are from D'Almeida(1987). For clouds, the size distribution is calculated from Eq.(2.1.7). The refractive index of water droplets is taken from Hale and Qerry (1973).

Table 2. Comparisons of aerosol radiative characteristics between the results of the WCP-55 (1983) report (WCP) and of the present (P) Mie code calculations at wavelength λ = 0.55 μm. (Extinct. coef. a(b) = a 10^{b})

	ω		g		extinction coeff.	
Aerosol Type	WCP	P	WCP	P	WCP	P
soot	.209	.209	.34	.34	5.58(-7)	5.55(-7)
oceanic	1.	1.	.78	.78	3.71(-3)	3.70(-3)
dustlike	.653	.653	.88	.88	1.86(-2)	1.87(-2)
water soluble	.957	.956	.63	.63	5.38(-7)	5.47(-7)
H_2SO_4 75%	1.	1.	.73	.73	1.10(-4)	1.09(-4)
volcanic	.947	.946	.70	.69	9.01(-5)	8.95(-5)

2.4 Description of parameters in the radiation models

2.4.1 Longwave part

For the longwave part two different methods were used: a narrowband model (Two - Stream - Approximation) developed by Schmetz (1986) for the non-scattering cases and the Matrix-Operator-Method for scattering cases. The description of gas absorption within the non-scattering model is also used in the Matrix-Operator-Method. The atmospheric absorbers considered in the present scheme are: (a) the water-vapour continuum absorption after Grassl(1976), (b) exponential-sum fits to the water-vapour line absorption from Lowtran-5 data (Kneizys et. al., 1980), (c) CO2 and O3 absorptions. The water-vapour line and CO2 line are treated by an exponential-sum fit (Wiscombe and Evans, 1977). The atmospheric profile is divided into 40 homogeneous layers.

2.4.2 Shortwave part

The Matrix-Operator-Method is used for the shortwave part. It was made available to us by Dr. J.Fischer (GKSS), and it was extended with analytical expressions for the transmission and reflection matrices and rewritten for this study. In our version, the solar spectral range from 0.2 μm to 3.58 μm is divided into 37 intervals. Spectral data of the extraterrestrial solar spectrum are taken from Labs and Neckel (1968) and Neckel and Labs (1984). These data are based on a solar constant of S_o = 1357 W/m^2. Due to the expansion of transmissivity data for water vapour and carbon dioxide into exponential series, the total spectral intervals increase to 135. The model atmosphere, absorption coefficients of absorbing gases, the surface mean albedo data set and the vertical distribution of aerosol amounts are taken from the two-stream model of Kerschgens et al. (1976) and Schmetz (1984). The surface mean albedo for ocean and desert are taken from NASA report 1139 (1985). 10 atmospheric layers are selected. For the cloud case, we

assumed one cloud layer.Calculations were carried out for 3 different cloud types and 2 optical thicknesses: 2 water clouds (stratocumulus and altostratus) and 1 ice cloud (cirrus /cumulonimbus) with optical thicknesses at wavelength λ = 0.55 μm of 4.5 and 45. The underlying surface is taken as a Lambert surface with continental aerosol. All model calculations in the shortwave part are performed for 8 viewing zenith angles, 8 sun zenith angles and 32 relative azimuth angles(see table 3). The Gauss-Lobatto weight is used since it allows calculations at μ = 1 and μ = -1. A delta approximation for the phase function, to remove strong forward scattering properties (Potter, 1970), for clouds and desert is also applied.

Table 3. Angular discrete values

solar zenith θ_o in degree	viewing zenith θ in degree	relative azimuth $\phi_o - \phi$ in degree	
0.	0.	0.	180.00
14.17	14.17	10.58	201.18
25.94	25.94	21.17	211.77
37.62	37.62	31.76	222.36
49.27	49.27	42.35	232.95
60.91	60.91	52.94	243.53
72.55	72.55	63.52	254.12
84.18	84.18	74.11	264.71
		84.70	275.30
		95.29	285.89
		105.88	296.48
		116.47	307.06
		127.05	317.65
		137.64	328.24
		148.23	338.83
		158.82	349.42

3. Satellite data

3.1 METEOSAT data

The geostationary satellite METEOSAT observes the Earth with an imaging radiometer in three channels: (1) in the solar spectrum (VIS) between 0.4 μm and 1.1 μm; (2) in the infrared (IR) window region between 10.5 μm and 12.5 μm, and (3) in the water vapour (WV) absorption band between 5.7 μm and 7.1 μm. Images are taken at half-hourly intervals and the spatial resolution at the sub-satellite point is 2.5 x 2.5 km^2 for VIS and 5 x 5 km^2 in the IR and the WV channels.

3.2 METEOSAT Climate Data Set

The original METEOSAT observations are operationally processed to derive the climatological data set (CDS). The data contains segments of 32 x 32 pixels corresponding to about 160 x 160 km^2 at the subsatellite point. A multispectral image analysis is applied to these segments (Tomassini, 1981). A similar method (the asymmetric Gausian histogram analysis of Simmer, Raschke and Ruprecht, 1982) has been used in the International Satellite Cloud Climatology Project (ISCCP) cloud algorithm intercomparison(Rossow et al., 1985). The multispectral analysis begins with the computation of two-dimensional IR/VIS and IR/WV histograms. The basic concept of the applied cluster analysis is that peaks in the one-dimensional histogram can be approximated by Gaussian distribution functions. A successive application of the one-dimensional histogram analysis to each spectral range leads to an extraction of a cluster from the two-dimensional histogram. After the elimination of this cluster from the segment the procedure is repeated. Each of the extracted clusters are identified with a certain scene. These scenes can be sea, various types of land, and different clouds. A cluster is characterized by its mean count (uncalibrated radiance), standard deviation, and the number of pixels. The CDS gives at most three cloud types in a

segment: high clouds (above 400 hPa), medium clouds (between 400 and 700 hPa) and low clouds(below 700 hPa).The CDS is derived eight times per day (at 3-hour intervals from 02:00 to 23:00 UTC), which is sufficient to resolve the diurnal cycle in the longwave part.

3.3 Calibration

The quantitative extraction of meteorological information from satellite radiometer data requires an absolute calibration of the radiometer. The calibration establishes a functional relationship between the satellite measured digital counts and the physical value radiance. METEOSAT-2 has an onboard calibration system for IR. But no such onboard calibration system for VIS and WV. The VIS and WV channels of the METEOSAT-2 radiometer are calibrated by the method of "vicarious calibration by means of calculated radiances" (Koepke, 1983; Schmetz, 1989), although for the CDS data used here (April 1985) the WV calibration followed a less rigorous approach (see discussion in Schmetz et al., 1990). The accuracy of the calibration is about 10% for the METEOSAT-2 VIS channel and about 5% for METEOSAT-2 WV channel. The onboard calibration system for the IR channel does not provide an absolute calibration since the system does not include the whole optical system used for the real-time observations. Therefore alternative vicarious methods based on radiative transfer calculations for the IR (Gaertner, 1989) and WV channel (Schmetz, 1989) are used for calibration on a daily basis. Calibration coefficients for METEOSAT VIS channel are not determined operationally. The calibration coefficient from Koepke (1983) is used here.

The calibration form for METEOSAT data is taken as

$$R_{ir} = CALi\ FAG\ (C_{ir} - C_{oir}) \qquad (3.3.1)$$

$$R_{wv} = CALw\ (C_{wv} - C_{owv}) \qquad (3.3.2)$$

$$R_{vis} = CALv\ (C_{vis} - C_{ovis}) \qquad (3.3.3)$$

with

CALi : calibration coefficient for IR channel
CALw : calibration coefficient for WV channel
CALv : calibration coefficient for VIS channel
FAG : gain factor.
C_{ir} , C_{wv} , C_{vis} are the radiometer count for IR, WV and VIS channels, respectively.

C_{oir}, C_{owv} , C_{ovis} are space count for IR, WV and VIS channels, respectively.

For CDS of April 1985, we take the following calibration parameters

$$R_{ir} = 0.049 \ (C_{ir} - 5 \times FAG) \qquad (3.3.4)$$

$$R_{wv} = 0.00785 \ (C_{wv} \times 4 - 6) \qquad (3.3.5)$$

$$R_{vis} = 2.3 \ C_{vis} \cos(\theta_o) \qquad (3.3.6)$$

with FAG = 0.875

It is worth to mention that the cluster mean counts C_{ir} and C_{vis} , provided by archived CDS, include already the FAG and normalization with the cosine of the solar zenith angle.

4. Estimation of the radiation budget components from METEOSAT

The aim of this study was to develop an operational method to calculate the two radiation budget components at the top of the atmosphere using the METEOSAT Climate Data Set. Since the method should be operational it has to be very fast. Thus, the radiative transfer model discussed in the previous chapters can not be used directly. Besides not all information needed in the radiative transfer model are actually available. The approximation which is applied here is based on the analysis of the "correct" results of the calculations from the radiative transfer model. For the

outgoing longwave radiation flux a regression equation is derived, which is based on the commonly used limb darkening function.

A different approach is used for the planetary albedo: look-up tables are calculated for different scenes and mean atmospheric state. For the determination of the actual planetary albedo the deviation of the broadband radiances between the estimated value from METEOSAT observations and the mean value from the look-up tables is used.

4.1 Outgoing longwave radiation

The method (Schmetz and Liu, 1988) to convert METEOSAT IR and WV radiances into outgoing longwave radiation flux (OLR) is based on regression equations with a total of 19 regression coefficients. These regression equations can be derived in an analytical way by using empirical limb darking functions which are commonly applied in remote sensing (Abel and Gruber, 1979).

The expression for OLR in the regression equation is

$$OLR = \xi_o + \sum_{i=1}^{3} \xi_i F_{ir}^{i} + \sum_{i=1}^{3} \eta_i F_{wv}^{i} \qquad (4.1.1)$$

where the narrowband fluxes F_{ir} and F_{wv} are calculated from the measured radiances R_{ir} and R_{wv} according to

$$F_{ir} = a(\theta) \times R_{ir} + b(\theta) \qquad (4.1.2)$$

$$a(\theta) = k_1 + k_2 (\sec\theta - 1) + k_3 (\sec\theta - 1)^2 \qquad (4.1.3)$$

$$b(\theta) = k_4 + k_5 (\sec\theta - 1) + k_6 (\sec\theta - 1)^2 \qquad (4.1.4)$$

$$F_{wv} = c(\theta) \times R_{wv} + d(\theta) \qquad (4.1.5)$$

$$c(\theta) = l_1 + l_2 \ (\sec\theta - 1) + l_3 \ (\sec\theta - 1)^2 \qquad (4.1.6)$$

$$d(\theta) = l_4 + l_5 \ (\sec\theta - 1) + l_6 \ (\sec\theta - 1)^2 \qquad (4.1.7)$$

with θ : satellite zenith angle.

Table 4. Regression Coefficients to Model the Limb Darkening of the Satellite-Observed IR and WV Radiances.

IR	WV
k1 = 10.8597	l1 = 7.1183
k2 = 1.0178	l2 = 2.2350
k3 = -0.1163	l3 =-0.3495
k4 = 2.8466	l4 = 0.2877
k5 = -3.5113	l5 =-0.7389
k6 = 0.4823	l6 = 0.1332

Table 5. Regression Coefficients for the Conversion of Narrowband IR and WV Fluxes into a Broadband Flux.

	ζ_0 = 71.1730	
ζ_1 = 2.96836	ζ_2 = -0.008023	ζ_3 = 0.000012
η_1 = 3.54529	η_2 = 0.365618	η_3 = -0.018409

The regression coefficients (see tables 4 and 5) are determined by a statistical analysis of the results of the longwave radiation transfer model. The calculations are carried out for 200 radiosonde ascents and with 15 zenith angles, which produce 3000 samples. The coefficients were checked against 200 independent radiosonde data. The narrowband radiances R_{ir} and R_{wv} and the OLR are calculated

with the Two-Stream Model for these 200 additional radiosondes. Then the calculated R_{ir} and R_{wv} are used in the regression model to estimate OLR. Table 6 shows a comparison of both OLR. Since the values shown in table 6 agree quite well (about 1%) , we conclude that the regression coefficients are stable and applicable to different atmospheric conditions. The above 400 radiosonde ascents are taken from a TOVS package, a global data set covering all seasons. One should note that the regression coefficients depend on the filter function of the satellite's radiometer. Values given here pertain to the METEOSAT-2 WV and IR-1 channels, respectively.

In order to demonstrate the contribution of the WV channel to the accuracy of the OLR estimates by the regression model, a simple model was derived using only the IR channel radiances. We carried out a similar calculation as described above. The error increased by about 75% in the mean rms and about 40% in the maximum (Table 6). The additional observations in the WV channel are very helpful for conversions of the filtered narrowband radiances to the unfiltered broadband fluxes (see comments in section 8).

Table 6. The rms Error and Maximum Error between the "Exact" OLR from a Radiation Transfer Model and the OLR Estimated with the Regression Technique for 200 independent radiosonde data.

IR and WV Observations		IR Observations only	
rms Error W/m^2	Maximum Error W/m^2	rms Error W/m^2	Maximum Error W/m^2
3.15	12.40	5.47	16.95

Another regression method to derive OLR from METEOSAT data has been reported by Cheruy et al.(1990). They select predictor variables and regression coefficients based on statistical analyses of simultaneous collocated METEOSAT data and ERBE radiant exitant data. Their method and our method give a good agreement with Lowtran calculations even for extreme atmospheric conditions (see table 7). These profiles include: very humidity profile (No. 31) and very dry profile (No. 55) in the high troposphere; dry atmosphere with low surface temperature (No. 56) and high surface temperature (No. 63).

Table 7. Radiances in the IR and WV channels of METEOSAT and OLR(L) calculated with the Lowtran program for different TIGR profiles (see Cheruy, 1990) and OLR calculated with the regression of Cheruy(1990) (C) and with our method(P).

Prof. No.	altitude of cloud (km)	IR $W/sr/m^2$	WV $W/sr/m^2$	OLR L	OLR C	OLR P
31	0.	5.98	0.639	264.	259.	263.
55	0.	5.95	1.506	300.	294.	298.
56	0.	4.407	1.375	251.	253.	257.
63	0.	6.33	1.470	304.	302.	305.
115	0.	7.12	0.70	302.	285.	290.
125	0.	4.02	0.637	219.	207.	217.
24	0.	6.29	0.635	267.	277.	270.
24	1.042	6.28	0.635	265.	277.	270.
24	2.907	5.40	0.635	247.	256.	250.
24	5.530	4.01	0.633	215.	220.	216.
24	7.971	2.92	0.598	184.	189.	187.
24	9.518	2.36	0.517	166.	169.	168.
24	11.001	1.90	0.406	147.	150.	151.

4.2. Planetary albedo

Multiple scattering of aerosols and surface reflection play an important role within the shortwave range. Therefore, the planetary albedo depends on scenes which are a combination of aerosols, atmospheric profiles and surface reflections. The METEOSAT CDS contains 14 distinct clusters. For the calculations of the look-up tables we extended the 14 clusters to 17 scenes, since we distinguish between thick and thin clouds i.e. optical thickness 45 and 4.5, respectively (see table 8).

The definition of planetary albedo is

$$\alpha = \frac{1}{\mu_o E_o} \int_o^{2\pi} \int_o^{\pi/2} Ib(\theta_o,\theta_v,\phi,s) \sin(\theta) \cos(\theta) \, d\theta_v \, d\phi$$

$$= \frac{\pi \, Ib(\theta_o,\theta_v,\phi,s)}{\mu_o E_o A} \qquad (4.2.1)$$

where Ib is the broadband radiance, and A is the anisotropic factor defined as

$$A = \frac{Ib(\theta_o,\theta_v,\phi,s)}{\frac{1}{\pi} \int_o^{2\pi} \int_o^{\pi/2} Ib(\theta_o,\theta_v,\phi,s) \sin(\theta) \cos(\theta) \, d\theta_v \, d\phi} \qquad (4.2.2)$$

θ_v : viewing zenith angle, ϕ : sun/ satellite relative azimuth angle, s : scene index.

Table 8. Scenes for look-up tables (anisotropic factors)

Cluster Index	Scene	Cluster Type Classification
1	A	Sea
2	B	Mountains free of snow
3	C	Mountains cover with snow
4	D	Savannah
5	E	Desert, bright sand
6	F	Desert, dark rock
7	G	Mediterranean vegetation
8	H	Coniferous forest
9	H	Equatorial forest
10	I	Pasture, dark, no vegetation
11	C	Snow on plain ground
12		no data
13		no data
14	J	Stratocumulus water cloud (opt. dep. = 4.5)
	K	Stratocumulus water cloud (opt. dep. = 45)
15	L	Altostratus water cloud (opt. dep. = 4.5)
	M	Altostratus water cloud (opt. dep. = 45)
16	N	Cirrus and cumulonimbus ice cloud(opt. dep.= 4.5)
	O	Cirrus and cumulonimbus ice cloud(opt. dep.= 45)

The above scenes are:

A: U.S. Standard atmos. profile, marine aerosol
B: U.S. Standard atmos. profile, continent aerosol, bare land
C: U.S. Standard atmos. profile, continent aerosol, snow
D: U.S. Standard atmos. profile, continent aerosol, savannah
E: Tropic summer dry profile, desert sand storm aerosol, desert
F: Tropic summer dry profile, desert background aerosol, desert
G: U.S. Standard atmos. profile, continent aerosol, vegetated land
H: U.S. Standard atmos. profile, continent aerosol, coniferous forest
I: U.S. Standard atmos. profile,continent aerosol, pasture land
J
-O: U.S. Standard atmos. profile,continent aerosol for different cloud types and thicknesses.

The anisotropic factor is the ratio of the broadband anisotropic radiance Ib to the broadband isotropic radiance. Since actual anisotropic factors are unknown, we replace A by mean anisotropic factors Am in equation (4.2.1) as an approximation. That is

$$\alpha = \frac{\pi\ Ib(\theta_o,\theta_v,\phi,s)}{\mu_o\ E_o\ A_m} = \alpha_o + \frac{Ib(\theta_o,\theta_v,\phi,s) - Ibo(\theta_o,\theta_v,\phi,s)}{Ibo(\theta_o,\theta_v,\phi,s)}\ \alpha_o \qquad (4.2.3)$$

with

$$A_m = \frac{Ibo(\theta_o,\theta_v,\phi,s)}{\frac{1}{\pi}\int_o^{2\pi}\int_o^{\pi/2} Ibo(\theta_o,\theta_v,\phi,s)\ \sin(\theta)\ \cos(\theta)\ d\theta_v\ d\phi} \qquad (4.2.4a)$$

and

$$\alpha_o = \frac{\pi\ Ibo(\theta_o,\theta_v,\phi,s)}{\mu_o\ E_o\ A_m} \qquad (4.2.4b)$$

Ibo and α_o were precalculated for several scenes based on radiation model calculations, and stored in look-up tables. With this approximation - using Am instead of A in the denominator of equation (4.2.1) - α can be calculated by (small) relative differences between observations and precalculated parameters.

The broadband radiance Ib is calculated from METEOSAT VIS radiance R_{vis} according to

$$Ib = Fsol \times R_{vis} \qquad (4.2.5)$$

The conversion factor Fsol, which converts filtered narrowband radiance into unfiltered broadband radiance, has to take into

account for all observational conditions such as observed geometry parameters, aerosol type and its distribution, and the optical properties of the underlying surface itself. An empirial conversion factor F_{sol} for METEOSAT provided by Stum et. al. (1985) is a function of geometry angles, water vapour amount, spectral averaged surface albedo and spectral band ratio. The latter three parameters are difficult to obtain in an operational scheme. Therefore, we choose following form for F_{sol}

$$F_{sol} = a_0 + a_1 (\theta_0 - 20) + a_2 (\theta_0 - 20)^2 + a_3 (\theta_v - 23) + a_4 (\theta_v - 23)^2 + a_5 \sin(\theta) \sin(\theta_0) \cos(\phi) + a_6 \sin(\theta) \sin(\theta_0) \cos(\phi) \cos(\phi) \qquad (4.2.6)$$

The above regression coefficients a_i were determined by statistical analysis of model results for each scene. Thus a_i include scene dependent mean information on surface, aerosol and water vapour amount. F_{sol} ranges between 2 and 4. Using an empirial expression such as Eq.(4.2.6) for the conversion factor F_{sol}, improves the solar broadband radiance estimation (see table 9) from METEOSAT visible observations compared with using scene dependent but constant conversion factors (Koepke, 1983).

Ibo and α_o are calculated for 8 viewing zenith angles, 8 sun zenith angles and 32 relative azimuth angles and are extended with cubic interpolations to 10 x 10 x 37 tables with 10 degree interval for zenith angles and relative azimuth angles. A solar constant 1357 W/m^2 is used. One should also note that the above regression coefficients depend on the filter function of the satellite's radiometer.

Table 9. Error analysis of the calculated planetary albedo based on 2 regression models.
A: with conversion factor (see Eq.4.2.6).
B: with scene dependent but constant conversion factors.

Scene	A		B	
	bias	RMS	bias	RMS
ocean	.067	.815	.791	2.575
steppe	.026	.412	.546	1.829
desert	.030	.728	.488	1.715
pasture	.037	.803	1.006	3.334
snow	.005	.524	.005	.570

5. Validation - Comparison with ERBE data

5.1 ERBE data

The Earth Radiation Budget Experiment (ERBE) includes three satellites in different sun synchronous orbits. The space shuttle Challenger launched the first of three satellites, Earth Radiation Budget Satellite (ERBS) in October 1984; the second satellite NOAA-9 was launched in December 1984 and the third satellite NOAA-10 was launched in July 1986. In our study, we used ERBE data for April 1985 gathered by ERBS and the NOAA-9 satellite. Each satellite contains a pair of instrument packages: a scanner and a nonscanner, only the scanner measurements are used here. The scanner instrument consists of three channels: a shortwave channel (0.2 - 5.0 μm), a longwave channel (5.0 - 50 μm), and a total channel which measures all radiation from 0.2 - to more than 50 μm. The ERBE data has a space resolution of about 35 km at the subsatellite point. The individual observations analyzed to produce instantaneous radiant exitances at the top of the atmosphere averaged over 2.5 degree for latitude and 2.5 degree for longitude regions. OLR and planetary albedo were derived from these data by using proper bidirectional models. The results were stored and

named hour box data with 4 scene classifications. The 4 scenes are : clear (cloud cover < 5%), partly cloudy (cloud cover between 5% and 50%), mostly cloudy (cloud cover from 50% to 95%), and overcast (cloud cover > 95%) The monthly mean OLR were calculated from the existing observations through interpolations and extrapolations and a diurnal model, which is just a sinusoidal fit in the case of planetary albedo. The clear cases are evaluated separately to calculate the monthly mean clear sky OLR and planetary albedo.

5.2 Calculation of the mean values for the METEOSAT segments

In order to calculate the mean OLR and planetary albedo of a CDS segment, the regression equations and look-up tables are applied to each cluster separately and the results are averaged according to:

$$OLR = \sum_{i=1}^{N} n_i \, F_{oi} \; / \; \sum_{i=1}^{N} n_i \qquad (5.2.1)$$

$$\alpha = \sum_{i=1}^{N} n_i \, \alpha_i \; / \; \sum_{i=1}^{N} n_i \qquad (5.2.2)$$

with n_i = number of pixels of ith cluster.

The METEOSAT Climate Data Set can represent the original high-resolution data well. For the planetary albedo the results from CDS and of the original high-resolution data should closely agree, since the relationship converting filtered METEOSAT VIS radiance to broadband radiance is linear and the look-up table is scene dependent only. Schmetz and Liu (1988) have demonstrated that the OLR estimation from the CDS agrees with the OLR estimation from the original high-resolution data although the conversion relationship from the narrowband fluxes to the broadband flux is nonlinear. The RMS error between OLR values from the two data sets is 4.1 W m^{-2}, the mean bias is 0.3 W m^{-2}, and the linear correlation coefficient is 0.997.

5.3 Comparison between the results of this method and of ERBE

The ERBE data are considered the most reliable radiation budget data today. Therefore the ERBE data of April 1985 are used for a comparison. Since both data sets have different spatial and temporal resolution and distribution, a certain time and space window had to be defined for the comparison: spatial difference of less than 1 degree longitude/ latitude, temporal difference of less than 1 hour. Due to this fact disagreement can appear at regions where the gradients are large e.g. coast lines and boundaries of cloud fields. The comparisons are performed for the region viewed by METEOSAT, that is the area inside the circle of about 60° around the sub-satellite point (equator, 0°). In the following figures a rectangular is given of 40° N to 40° S and 30° W to 50° E.

5.3.1 Comparison of the outgoing longwave radiation flux

The comparison started with the most homogeneous cases - clear sky and overcast. The scatter diagram (Fig. 4, the lower cluster gives the overcast, the upper the clear sky cases) for all these cases (12744) shows that the agreement is reasonable: RMS difference 9.5 W/m^2 for the clear sky and 14.9 W/m^2 for the overcast cases, bias 3.8 W/m^2 and 2.2 W/m^2, respectively. The overcast situations (determined by CDS) which are considered here, are only for high clouds. If one compares the overcast cases for low and middle clouds the agreement is not as good, as shown in table 10. These situations are examined in more detail. All cases between April 1-15, 1985 which are characterized overcast by ERBE, are plotted in a diagram - albedo against OLR (Fig. 5). The striking feature is that overcast situations with high OLR i.e. low or very thin clouds do not exist in this ensemble, although they exist in the CDS. This points at a discrepancy in the two cloud detection algorithms.

Table 10. Comparisons of OLR determined by ERBE and calculated with our method from CDS for 3 cloud types in overcast situations. Bias = CDS - ERBE

cloud type	N	bias(W/m^2)	RMS(W/m^2)
Stratocumulus	36	66.1	77.5
Altostratus	224	14.3	30.8
Cirrus & Cumulonimbus	1068	2.2	14.9

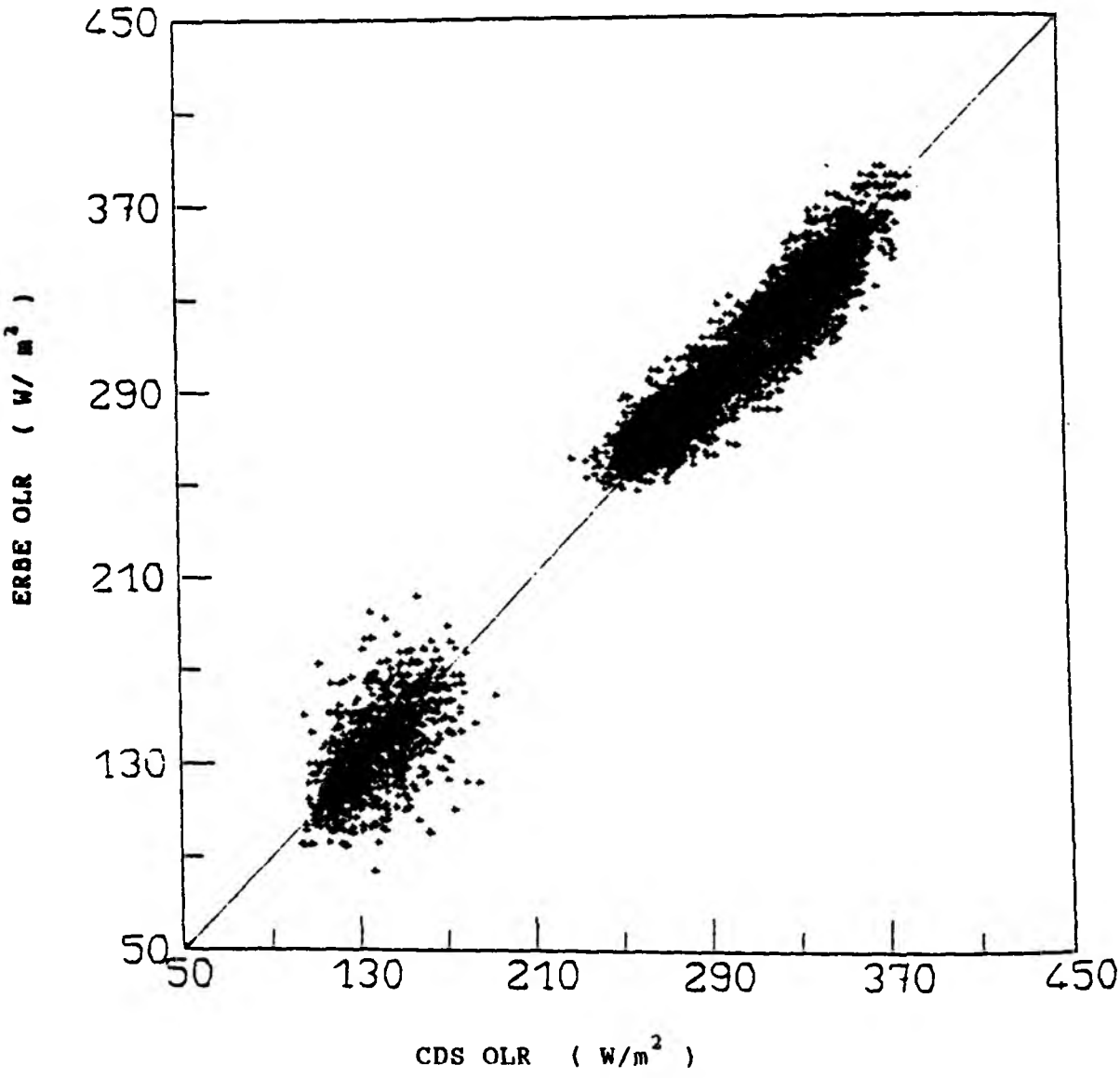

Figure 4.Comparison of the outgoing longwave radiation flux(OLR) estimated from the CDS with the outgoing longwave flux from the ERBE for all clear and overcast cases (only high cloud) in April 1985.
Sample number N = 12744, Correlation coef. = .98,
RMS = 10.0 W/m^2, Bias = 0.0 W/m^2.

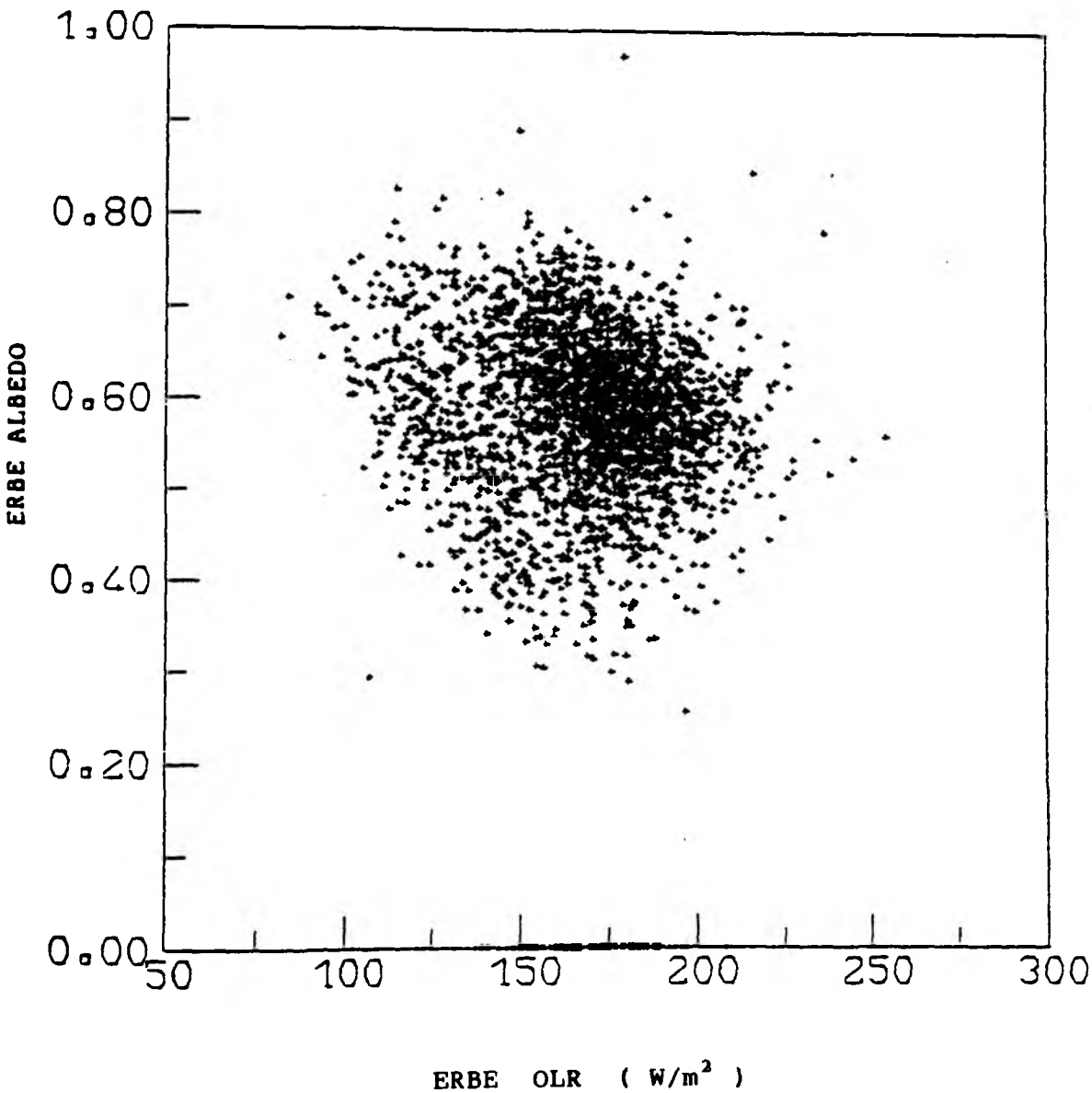

Figure 5.Two dimensional plot for planetary albedo and outgoing longwave radiation flux (OLR) of the ERBE data from April 1, 1985 to April 15, 1985 for overcast cases.

Therefore, direct comparisons between ERBE overcast and the CDS data, with cloud cover greater than 95%, will give a systematic bias due to cloud inhomogeneity and variability. The cloud detection might be a problem for the METEOSAT algorithm too. As an example table 11 lists OLR and planetary albedo at satellite nadir for clear sky pixels which are determined by the METEOSAT cluster analysis. It can be seen that the data for April 11 must be cloud contaminated. To limit the effect of cloud contamination, we considered as clear sky only such cases for which the whole segment was cloud free. The monthly mean distribution of OLR for cloud free situations derived from ERBE and from CDS is given in figures 6a-b. As already seen in figure 4 large differences do not appear. The general structure of the OLR fields are almost the same and resemble nearly the lower tropospheric temperature distribution with a maximum in Sahara desert. The minimum near the equator is caused by high water vapour content and lower surface temperature in the tropical forest area (cloud contamination cannot be excluded). There is almost no bias (0.0 W/m^2) between the ERBE data and the CDS data and the RMS is 4.9 W/m^2 . With cloudy cases, the largest difference between the two data sets is founded in ITCZ area. The difference is caused by the different methods how to prescribe the underlaying surface in strongly variing situations and by the different cloud detection methods. Since it affects only small area the large scale OLR distribution is not severely influenced. Comparisons of OLR with all cloud types for April 1985 give a bias of 4.0 W/m^2 and RMS of 6.9 W/m^2 (see figures 7a-c). This is acceptable for applications.

Table 11. Outgoing longwave radiation flux (OLR) and planetary albedo α (in %) estimated from the CDS at subsatellite point (0.65 S, 0.65 W) at 14 UTC in April 1985 for the clear condition of the CDS.

Day	OLR	α	Day	OLR	α
1	283.0	4.2	16		
2			17		
3	288.2	5.9	18		
4	279.4	7.0	19	273.7	8.1
5			20		
6	281.4	4.7	21	273.2	5.9
7	286.3	4.7	22	274.5	6.5
8	284.6	5.9	23	285.2	5.4
9			24	285.3	7.9
10			25		
11	246.5	8.3	26		
12	275.4	5.5	27	283.3	5.3
13	270.9	6.1	28	278.0	6.2
14			29	286.1	7.6
15	275.4	4.7	30		

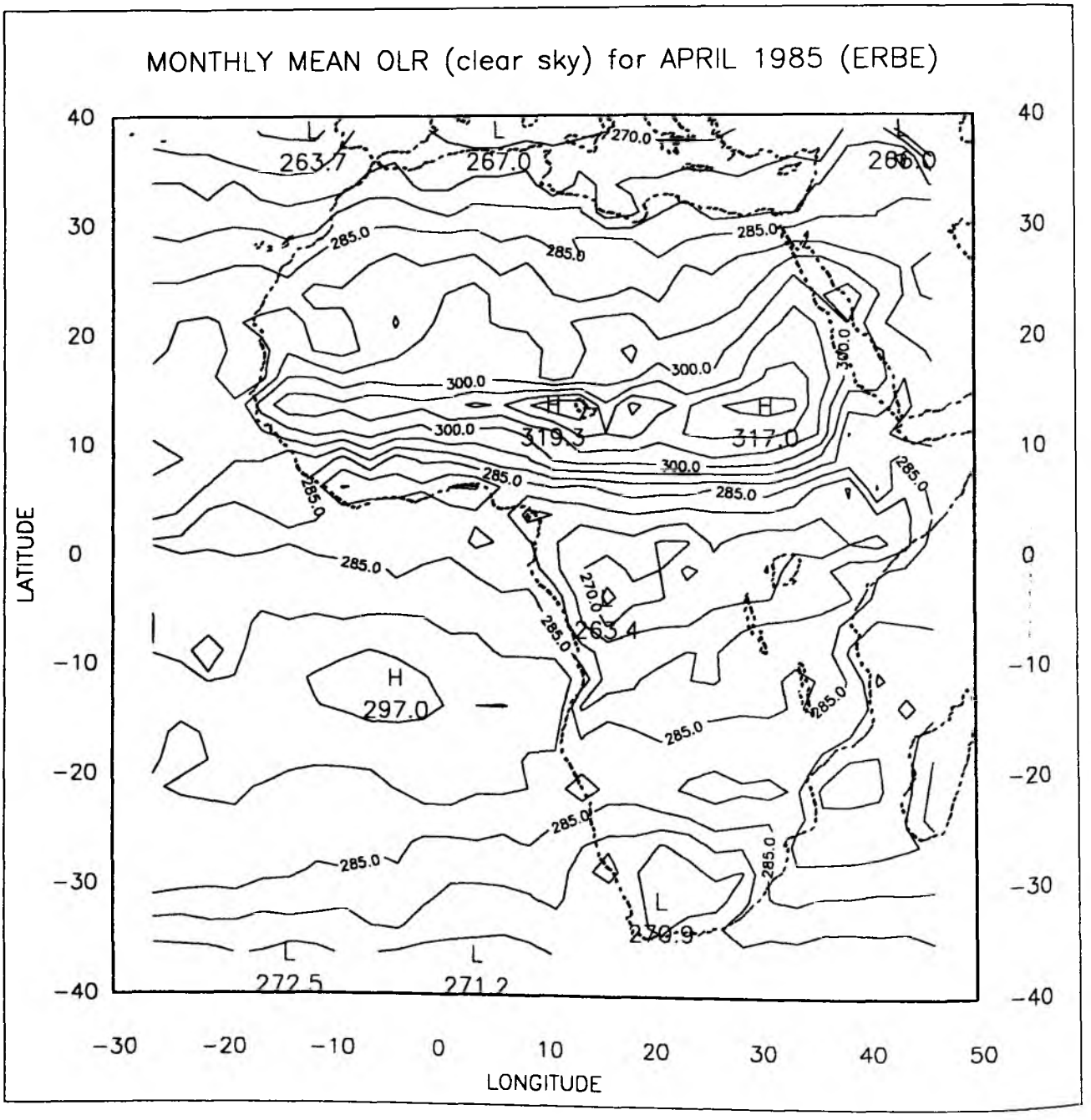

Figure 6a. Monthly mean clear sky OLR from the ERBE in April 1985. The plot interval is 5 W/m^2.

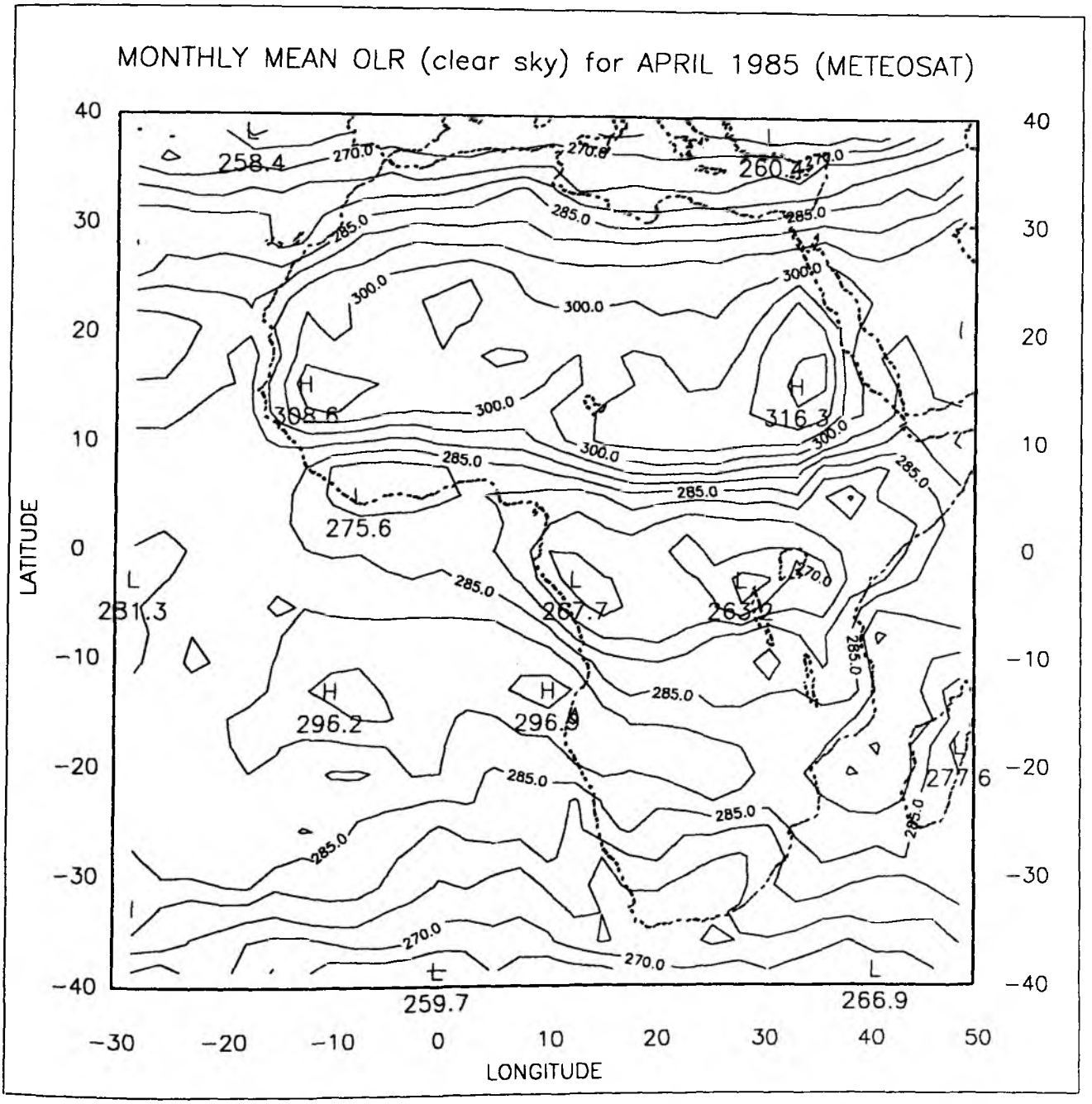

Figure 6b. Monthly mean clear sky OLR from the CDS in April 1985. The plot interval is 5 W/m^2.

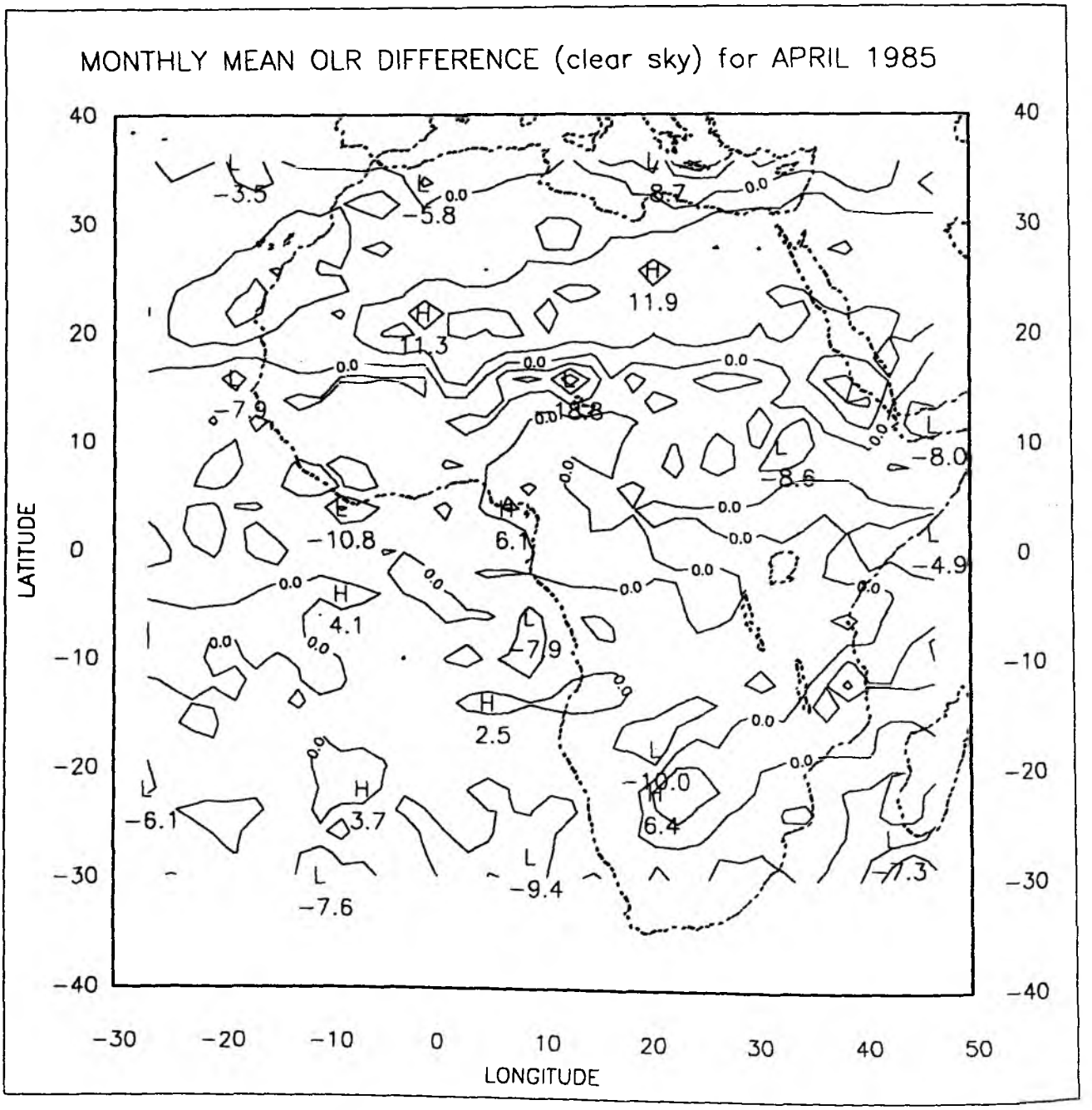

Figure 6c. Differences of monthly mean clear sky OLR between the CDS and the ERBE in April 1985 (CDS-ERBE). The plot interval is 5 W/m².

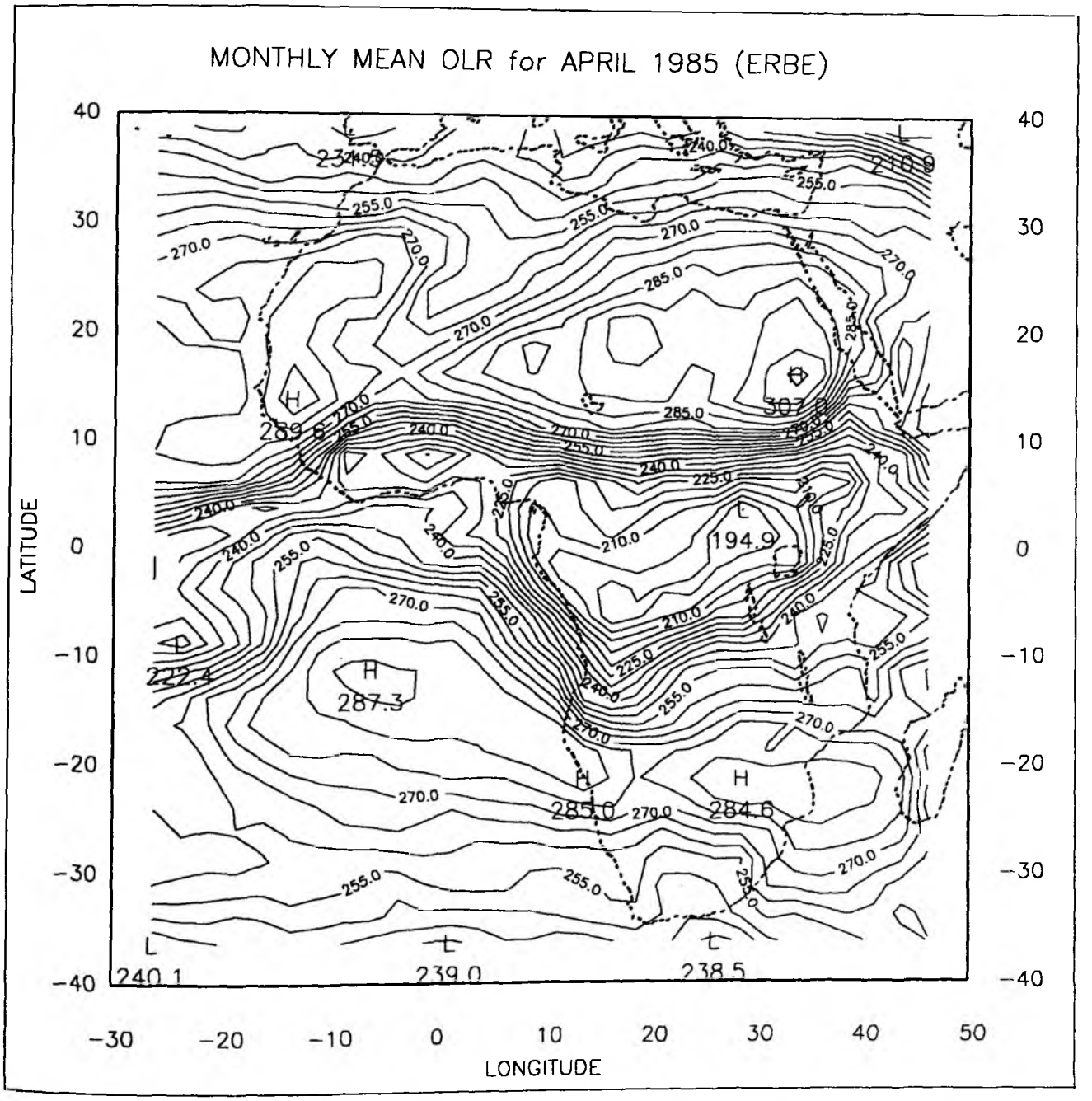

Figure 7a.Monthly mean OLR from the ERBE in April 1985. The plot interval is 5 W/m^2.

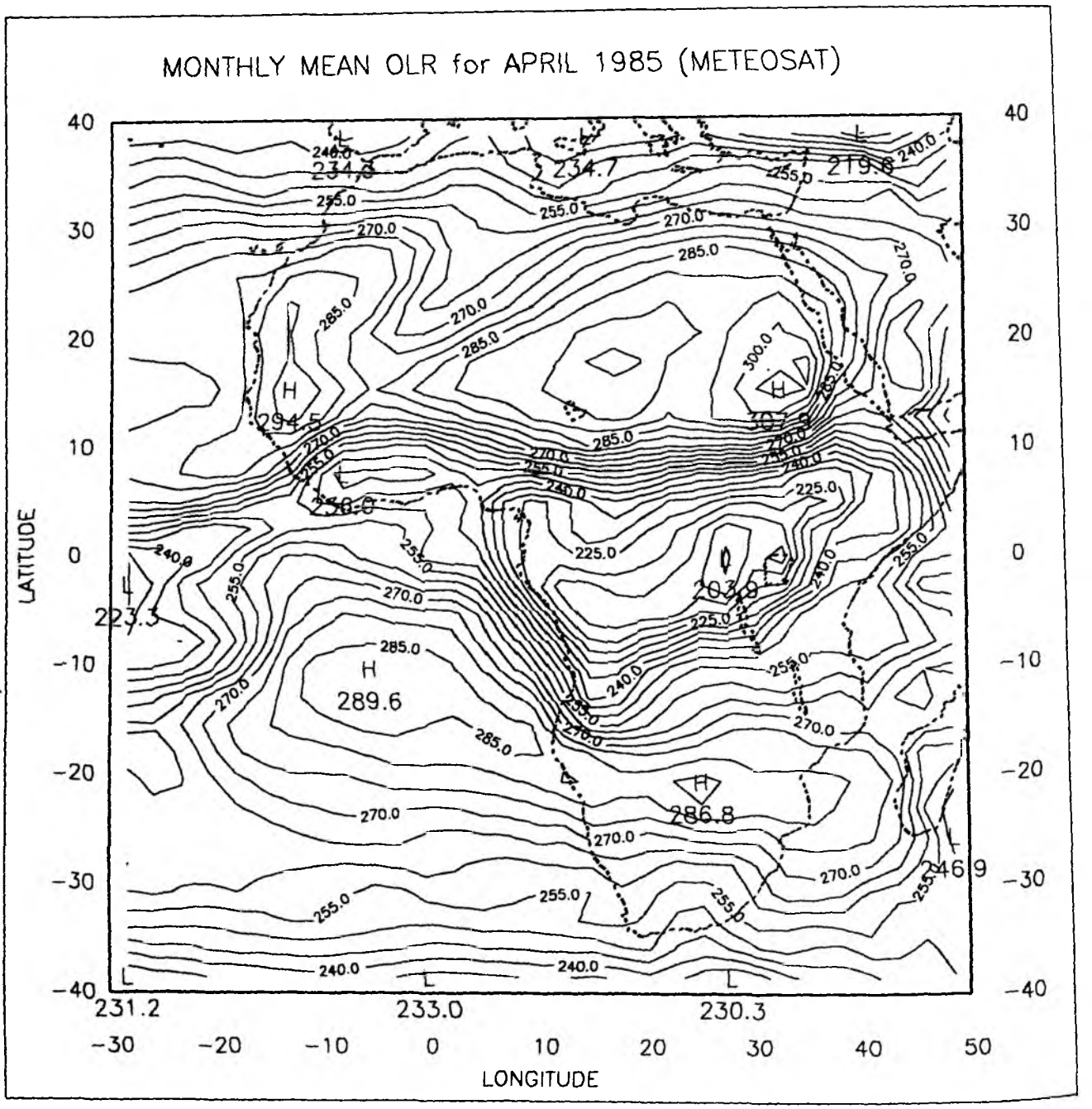

Figure 7b.Monthly mean OLR from the CDS in April 1985. The plot interval is 5 W/m^2.

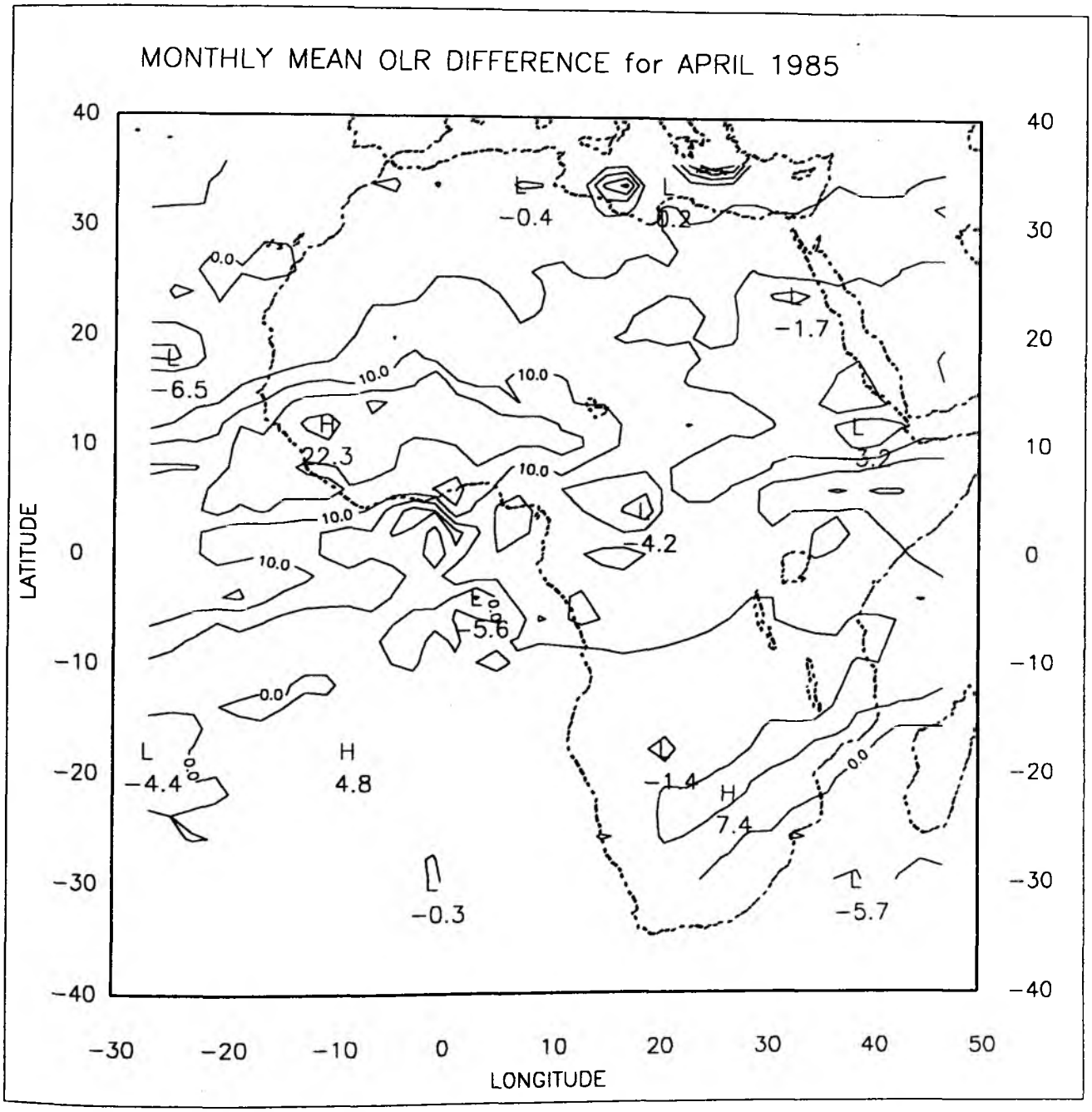

Figure 7c.Differences of monthly mean OLR between from the CDS and from the ERBE in April 1985(CDS-ERBE). The plot interval is 5 W/m^2.

Part of the difference between CDS and ERBE derived OLR may be due to the temporal resolution of the data. The monthly mean value for ERBE data is calculated by data interpolation, and a diurnal model fit for the day time. This treatment without data between morning and noon is about equivalent to the assumption that clouds are the same before noon and after noon. By a simple average of the OLR calculated from observations from CDS between 14:00 UTC and 23:00 UTC for the whole month gives similar values and geographical structures as the ERBE monthly mean OLR. Averaging over all available data of ERBE (hour box) without the interpolations and the diurnal model fit, gives also quite similar results(Figures 8a-c). The strong convection in the afternoon and relatively little convection in the morning in this area is not realistically described by the diurnal model fit.

5.3.2 Comparison for the planetary albedo

For the reasons we discussed in the previous section the comparison was repeated with the clear sky cases and overcast situation (only high clouds). Fig. 9 shows that the scatter of the planetary albedo for the cloudy cases is larger than that of the OLR (Fig. 4), but in general the agreement is reasonable. The monthly mean values show no great differences neither for the clear sky nor for the total mean (Fig. 10a,b and 11a,b). The clear sky albedo based on the CDS depicts some irregularities at the coast lines (Fig. 10a), a problem which was mentioned earlier. Otherwise the two data sets agree well qualitatively - e.g. locations of minima and maxima and also quantitatively. Only in equatorical Africa and at the coast of the Gulf of Guinea are the CDS derived albedos larger than the ERBE values; here the CDS radiances are probably cloud contaminated. This hypothesis is supported by the results in Fig. 11a,b (all situations, clear and cloudy) which agree quite well in that region. The results are reasonable considering 10% calibration error of the METEOSAT visible channel and other unknown factors. Another reason for the deviation of the monthly mean planetary albedo is due to sampling. CDS provides 3

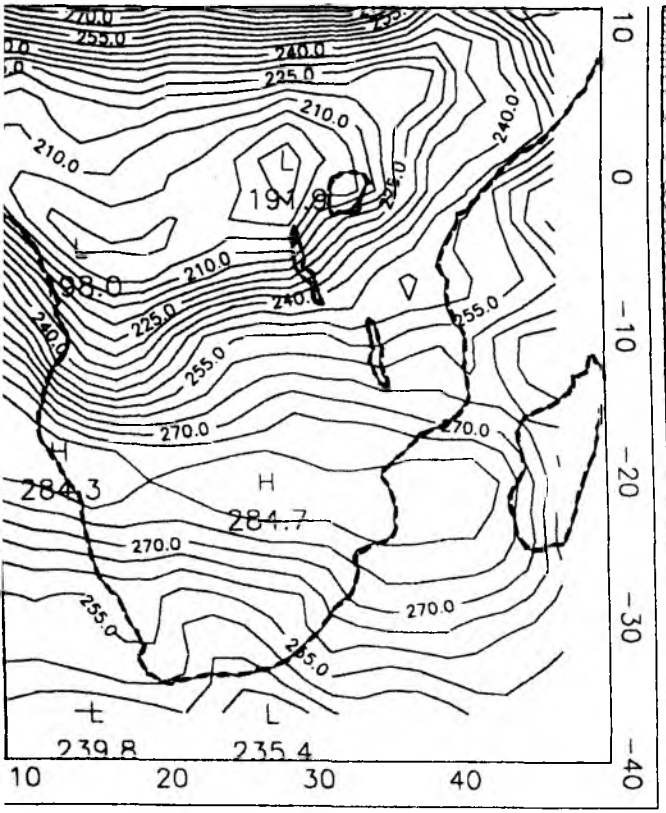

Figure 8a. Monthly mean OLR over deep convective cloud area averaged over all available data of the ERBE (hourly box data) for April 1985. The plot interval is 5 W/m**2.

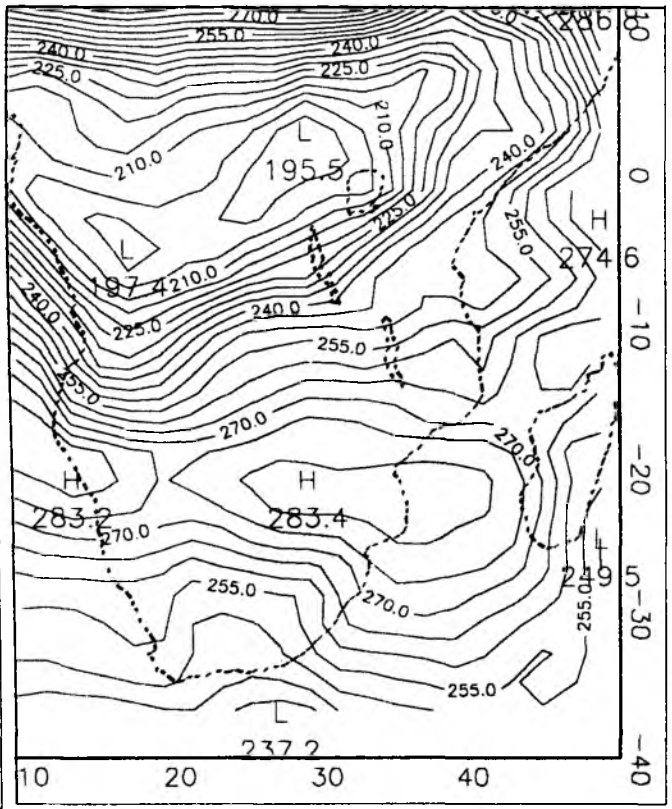

Figure 8b. Monthly mean OLR over deep convective cloud area from the ERBE monthly OLR (application of the diurnal model fit) for April 1985.
The plot interval is 5 W/m**2.

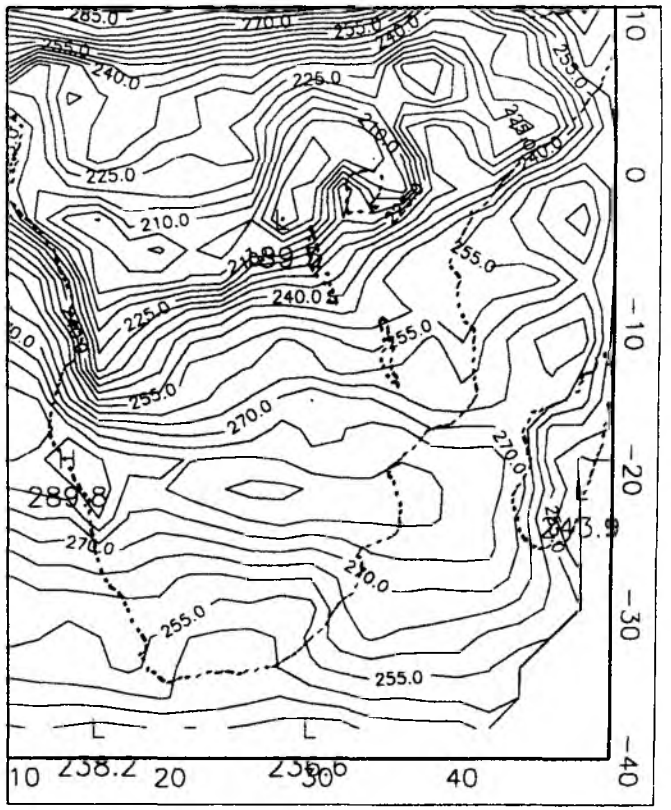

Figure 8c. Monthly mean OLR over deep convective cloud area calculated from the summarized CDS observations at 14, 17, 20, 23 UTC for April 1985.
The plot interval is 5 W/m**2.

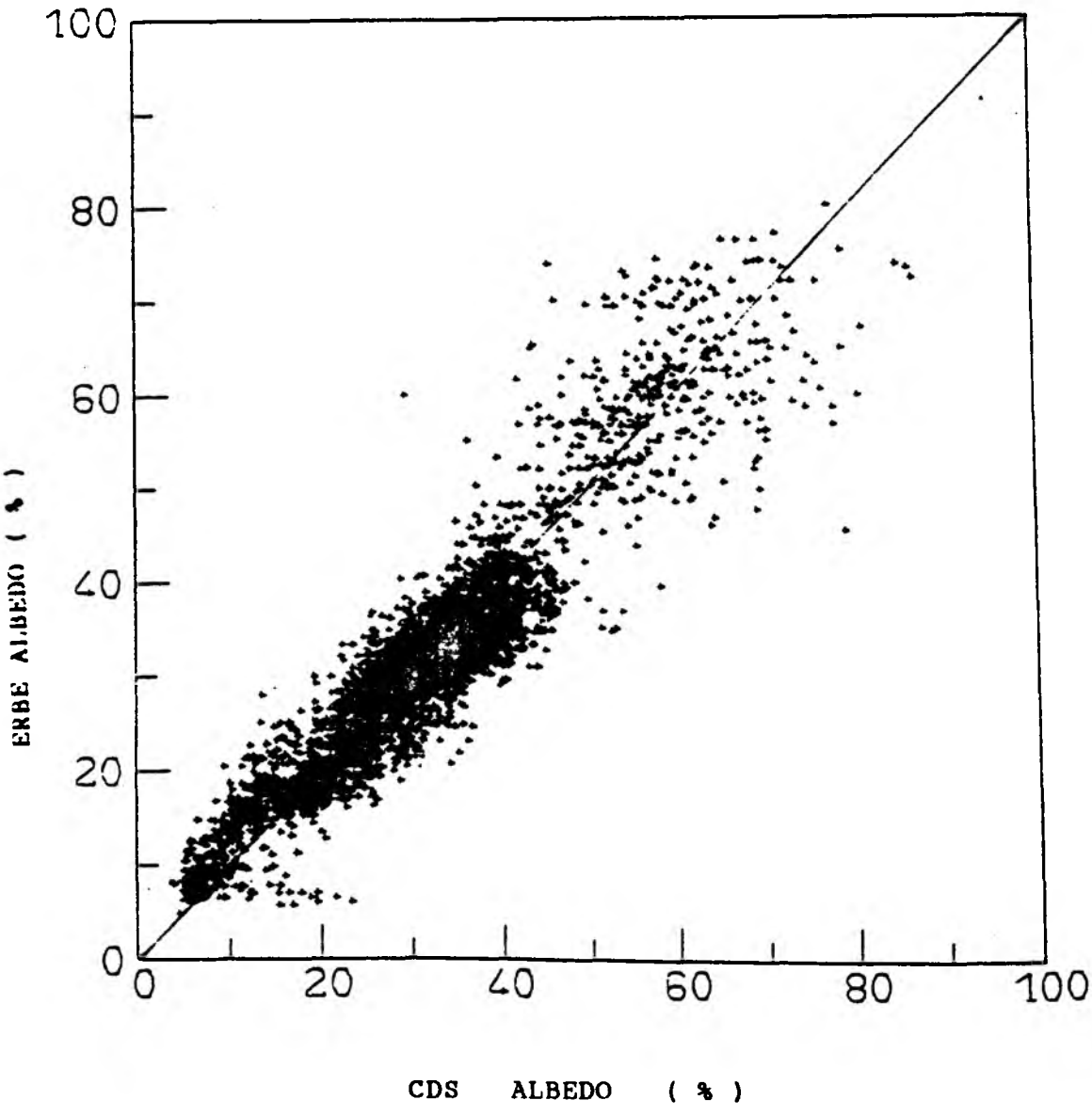

Figure 9. Comparison of the planetary albedo estimated from the CDS with that of ERBE for clear and overcast (only high clouds) cases in April 1985. Sample number N = 4851. Correlation coef. = .94 RMS = 4.33 and bias = -0.1 in absolute value.

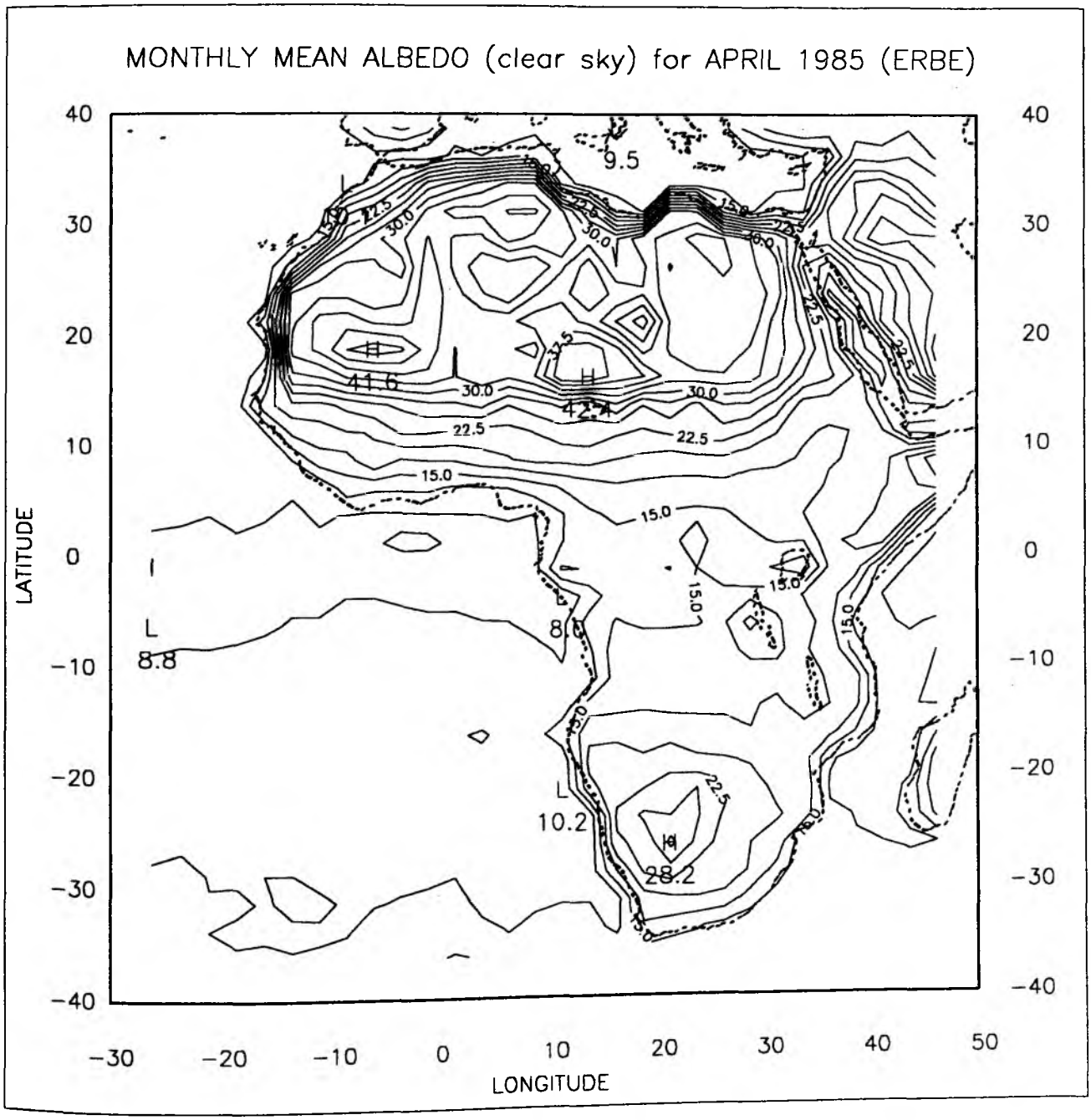

Figure 10a Monthly mean planetary albedo for clear sky from the ERBE in April 1985. The plot interval is 2.5 %.

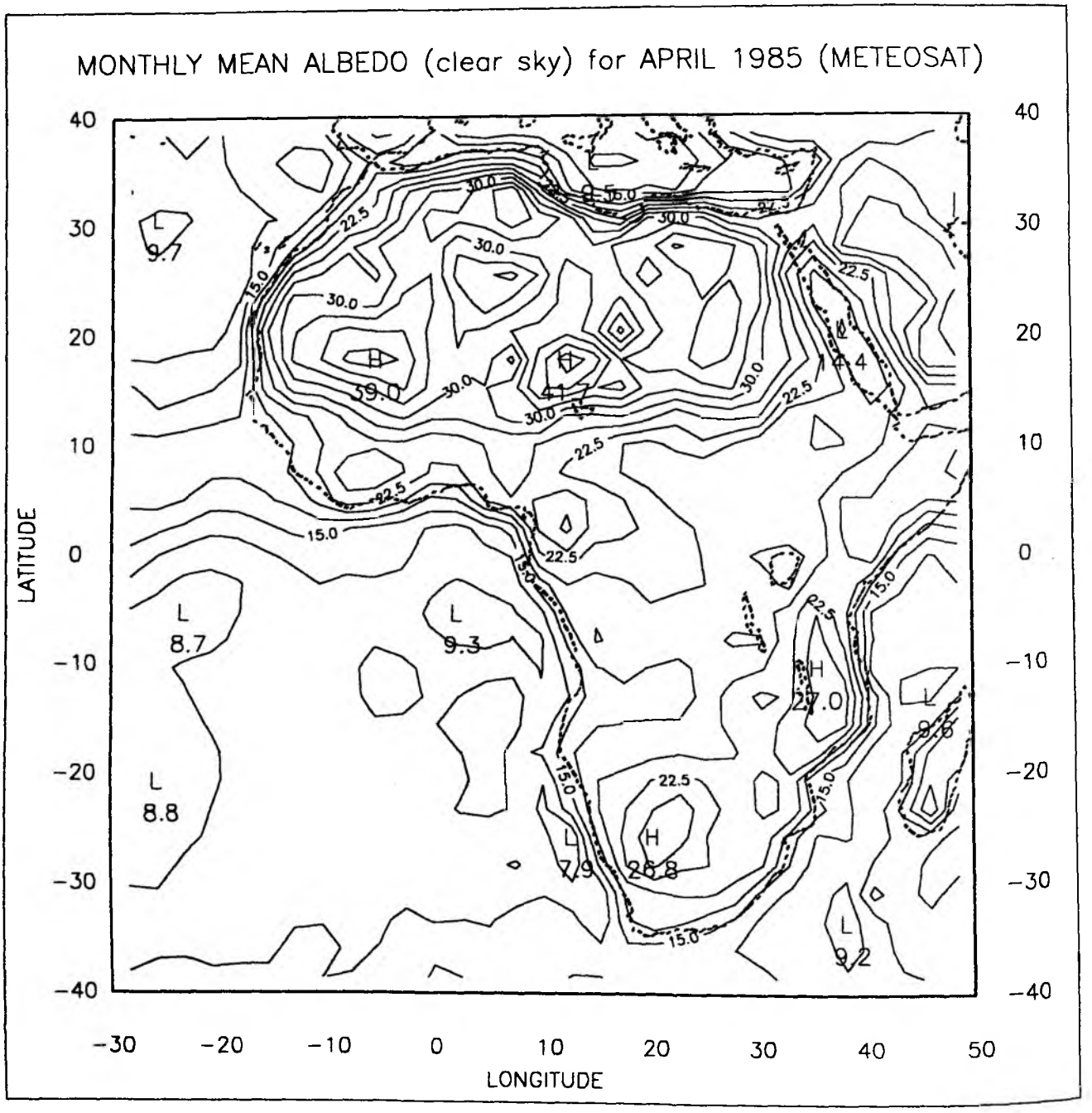

Figure 10b Monthly mean planetary albedo for clear sky from the CDS in April 1985. The plot interval is 2.5 %.

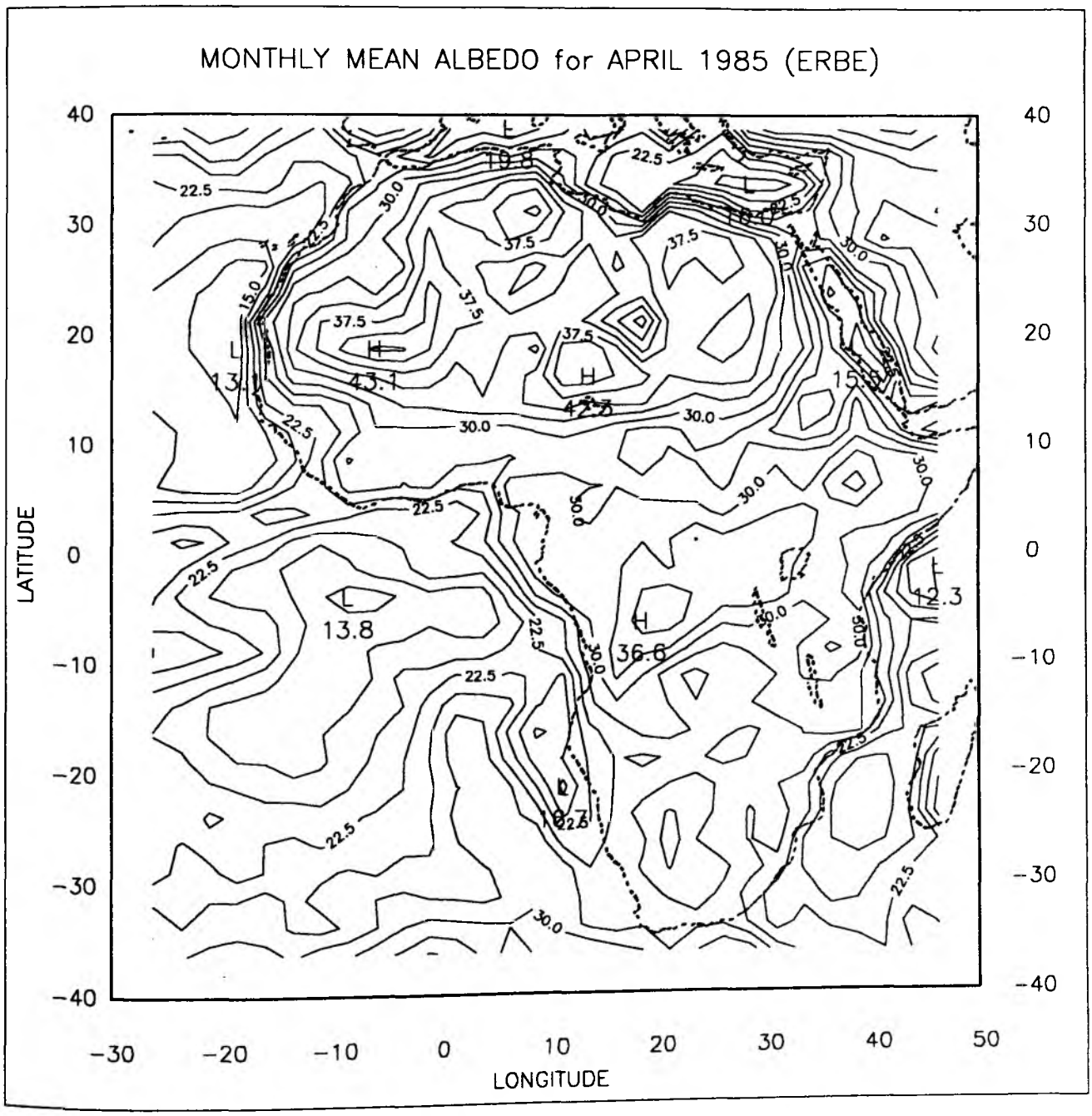

Figure 11a Monthly mean planetary albedo from the ERBE in April 1985. The plot interval is 2.5 %.

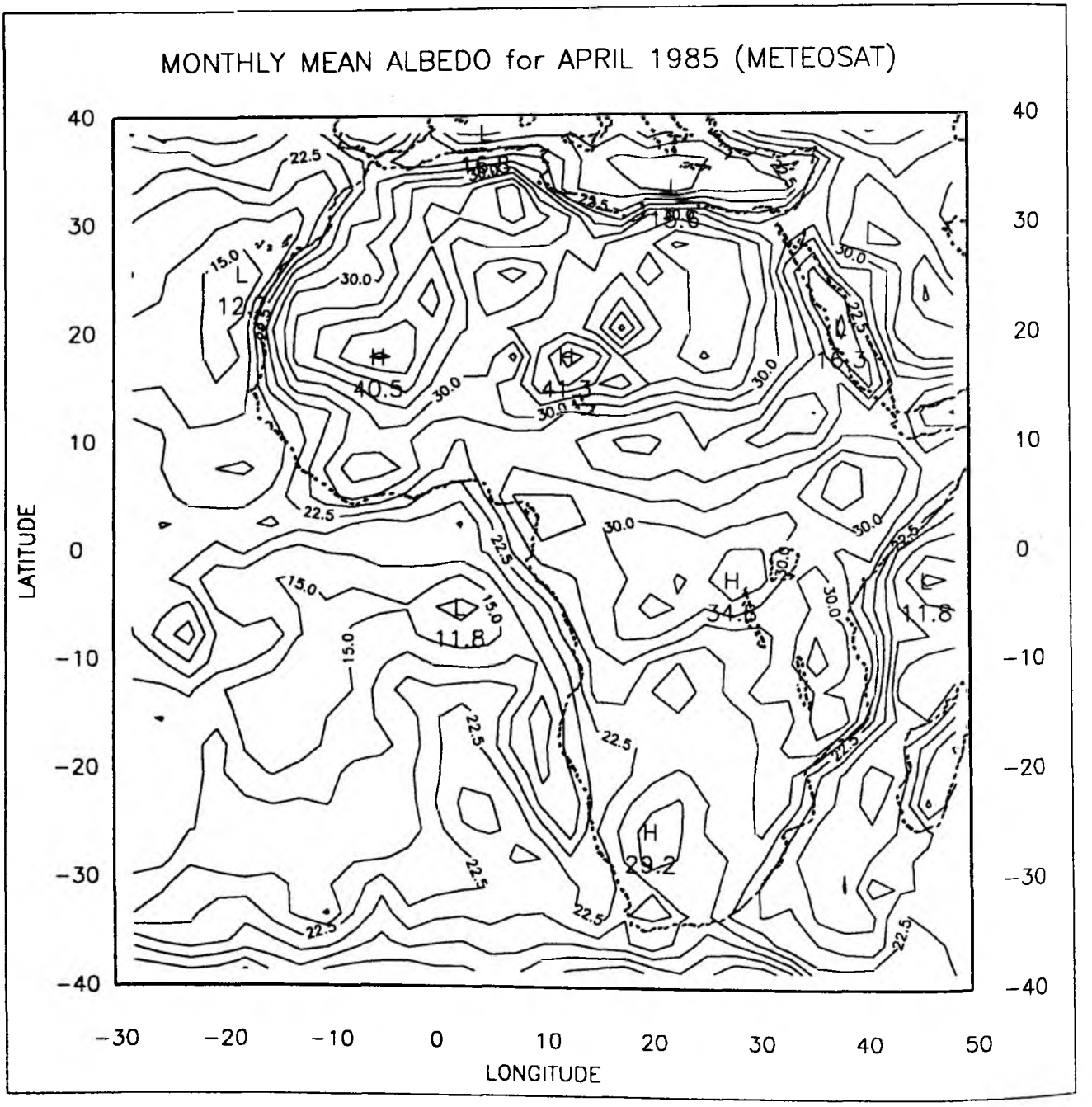

Figure 11b Monthly mean planetary albedo from the CDS in April 1985. The plot interval is 2.5 %.

useful measurements during day time in the solar spectral range. This appears to be insufficient for deriving the monthly mean planetary albedo. We computed the monthly mean values in a simple way, by averaging the albedo calculated from the CDS. ERBE yields often only one or two observations during day time however, but applies a diurnal model to the data. Another error may arise from the solar constant which varies from 1323.5 W/m^2 to 1414.9 W/m^2 during a year with a value at 1 AU (sun-earth distance) of 1368 W/m^2. The solar constant of 1357 W/m^2 used here could cause a bias error, however, this will be corrected for in the operational software package. An adjustment for the solar constant can be performed according to the sun-earth distance.

The monthly mean distribution for clear sky cases (see figures 10a-b) shows planetary albedos of the ocean between 8 and 15 percent whereby the largest values are found at the coasts only. Also very low values (about 15 percent) are calculated for the equatorial forest area. The largest planetary albedos occur at Sahara desert area. Comparing with Sahara desert, the vegetated land absorbs more solar energy and emitts less longwave radiation. Therefore, the vegetated land receives much more radiative energy to put it into the atmosphere (in form of sensible and latent energy).

6. Some results from the METEOSAT radiation budget index

6.1 Diurnal variation

Geosynchronous satellites provide a unique tool for observing diurnal change, as they typically complete a full earth scan in 30 minutes. Minnis and Harrison (1984a,b) have investigated the diurnal variation of cloud distribution and radiation budget from GOES data. Duvel and Kandel (1985) studied specific areas in the METEOSAT field of view for a 3 day period, and Schmetz and Liu (1988) derived the mean OLR diurnal variation for July 1983. We

studied the diurnal variations of the OLR and cloud distribution for April 1985.

The cloud cover given in the CDS is averaged over the whole month of April 1985 and displayed in Fig.12a. The monthly mean over Africa and the adjacent ocean varies between 0.8 in central Africa and off the coast of South-West Africa and cloud free areas in the central Sahara. In order to describe the diurnal variation the monthly average at a 3 hour interval is given in Fig. 12b-i (02, 05, 08, ... 23 UTC). The maximum over central Africa reaches even 1 during the night (23, 02, 05 UTC). The monthly mean OLR has a very similar distribution as the cloud cover. We selected three typical areas - desert (19.7 N, 20.8 E) , marine stratocumulus (16.7 S, 10.3 W) and tropical cloud convection within the ITCZ (7.3 S, 25.4 E). In the desert area, a minimum OLR occurs in the early morning about 3 local time and the maximum OLR at about local noon (Fig. 13) (the cloud cover varies from 2% to 8%). In the marine stratocumulus area, the monthly mean cloud cover reaches 42% (Fig. 14). The OLR varies from 278.7 W/m^2 to 281.4 W/m^2 with a monthly mean value of 279.7 W/m^2. These clouds do not produce a large greenhouse effect since they are very low and the temperature contrast between cloud top and sea surface is very small . In the tropical convection area, the OLR minimum is shifted to the late afternoon due to the maximum cloud development at that time (Fig. 15).

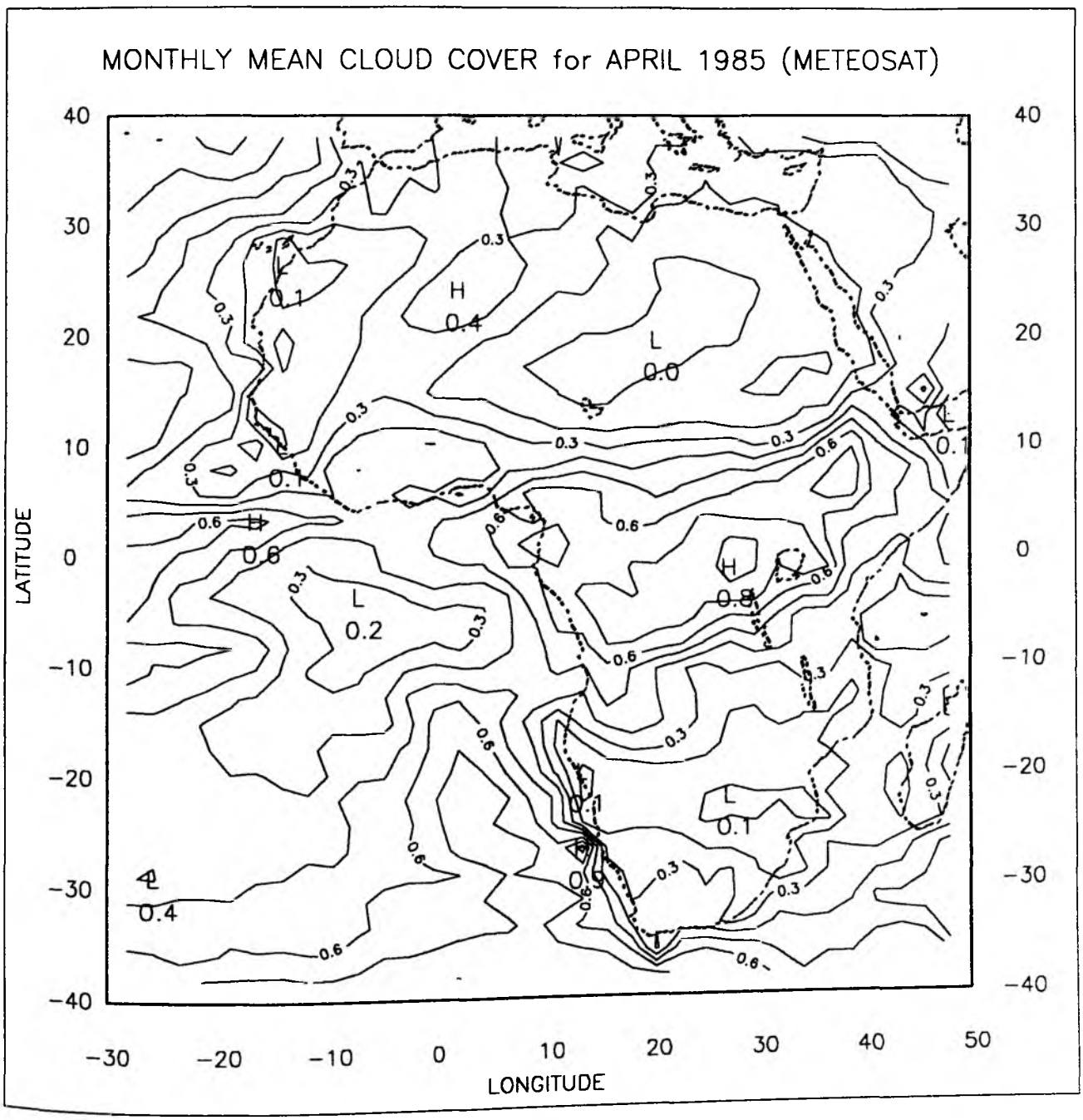

Figure 12a. Monthly mean cloud cover derived from the CDS. The plot interval is 0.1.

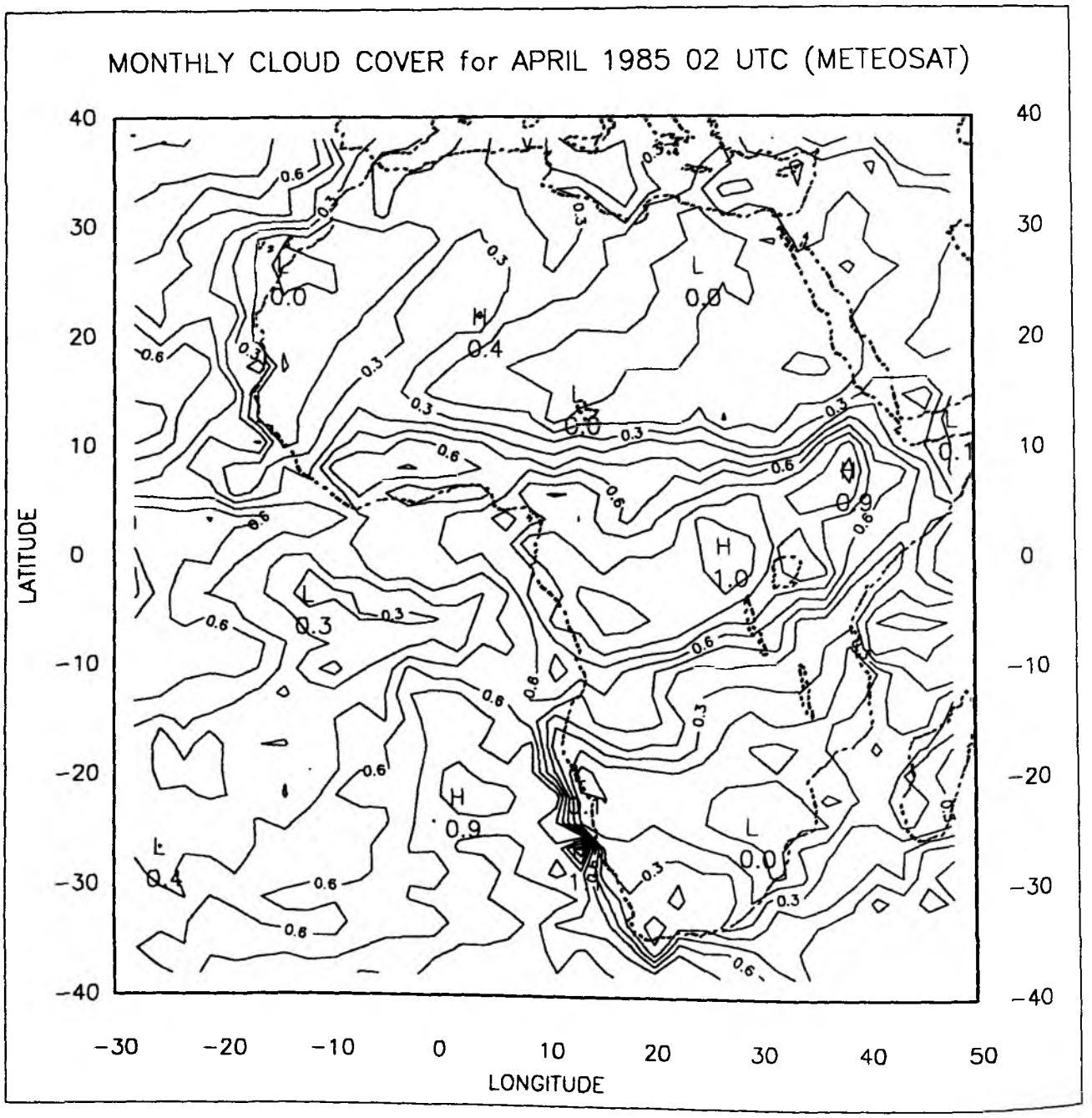

Figure 12b. Same as Fig. 12a but at 02 UTC.

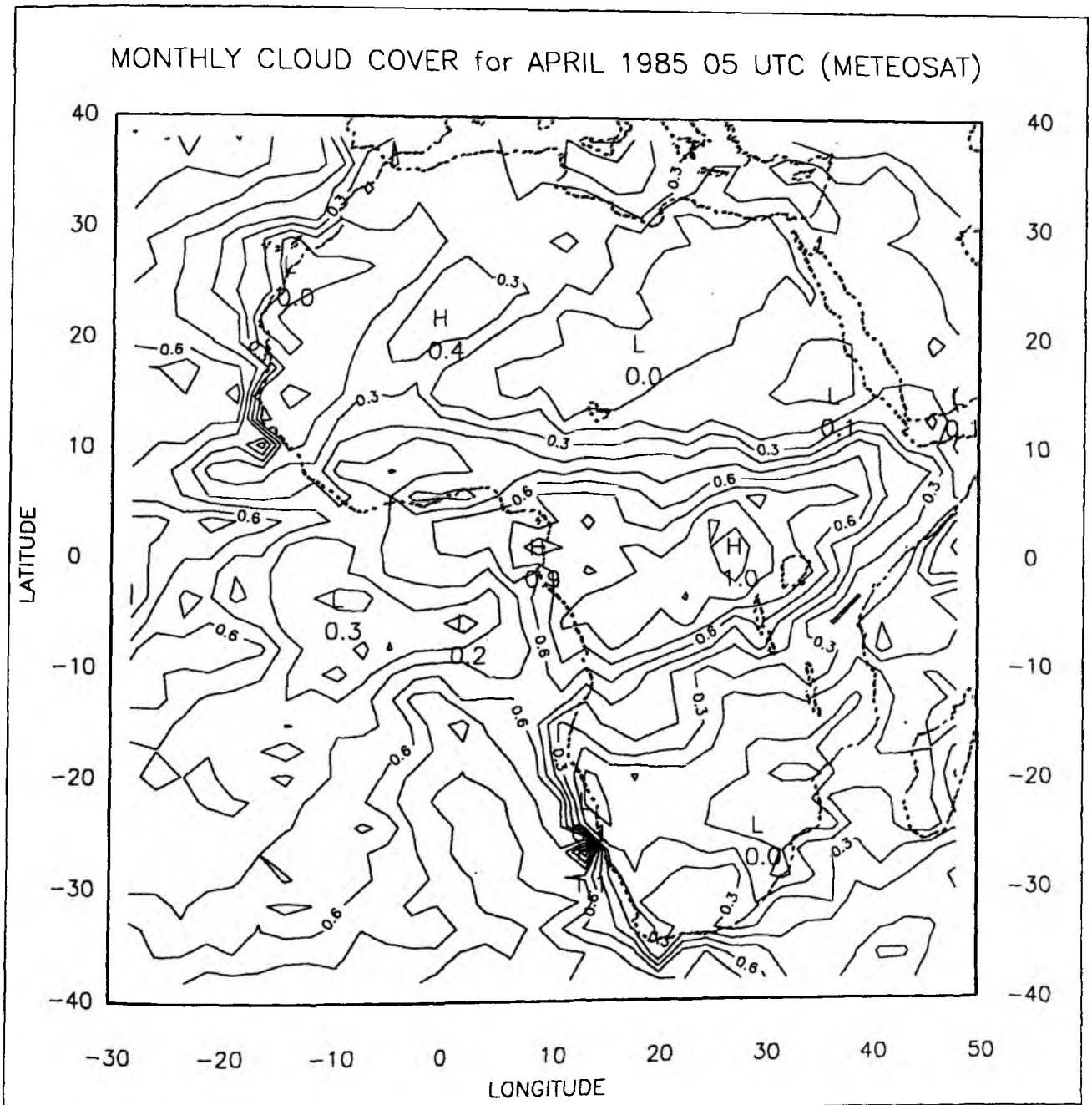

Figure 12c. Same as Fig. 12a but at 05 UTC.

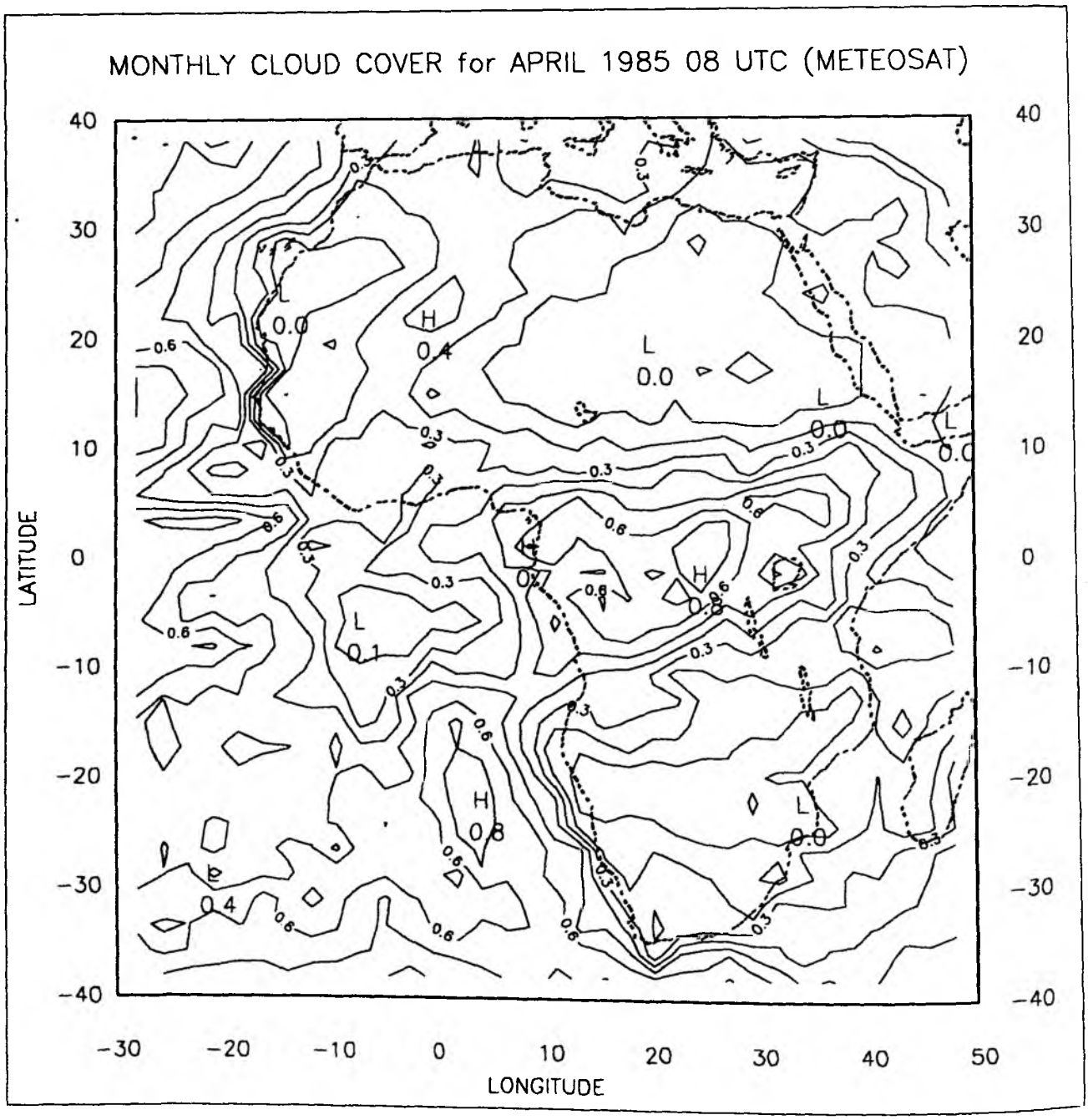

Figure 12d. Same as Fig. 12a but at 08 UTC.

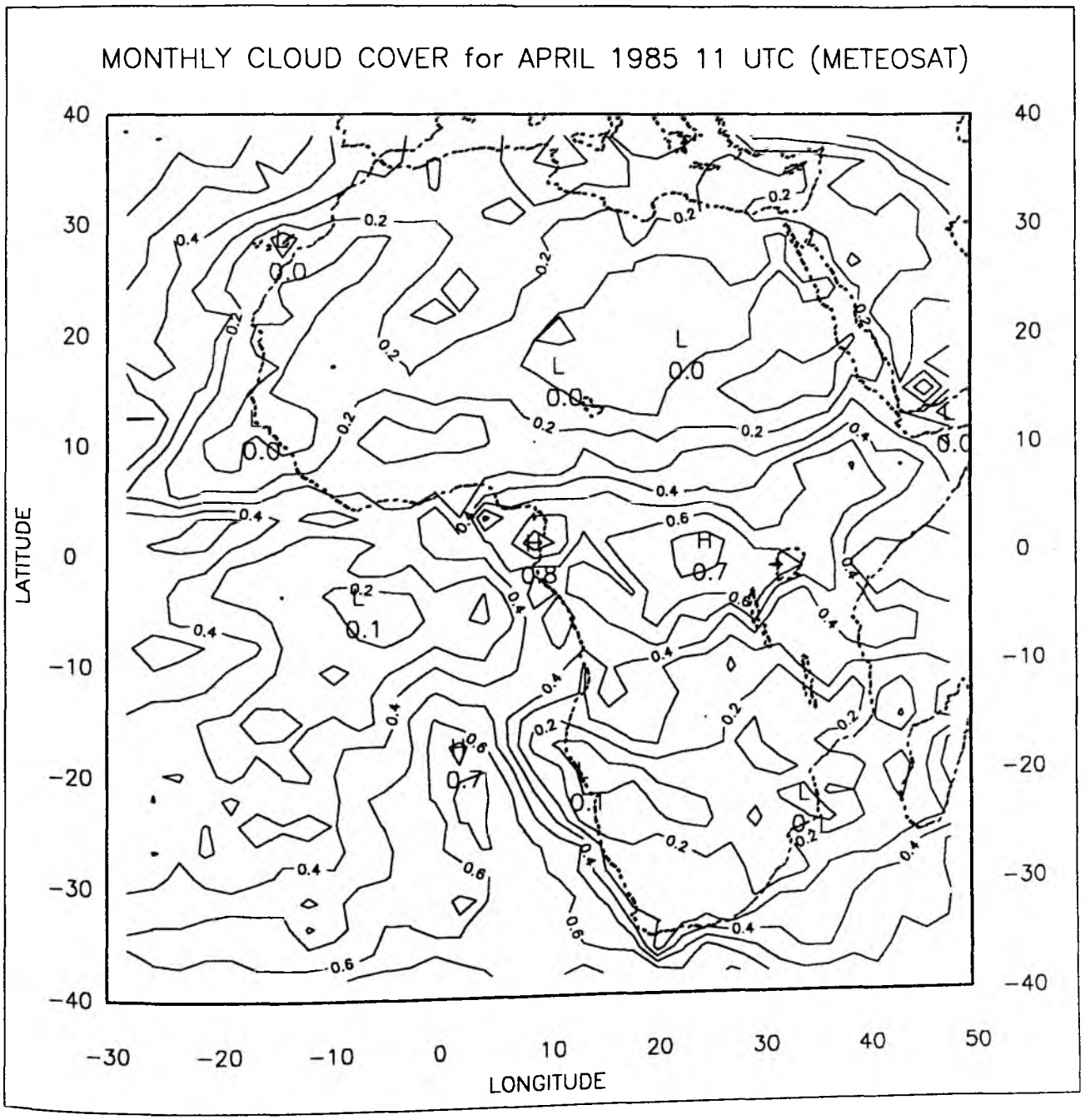

Figure 12e. Same as Fig. 12a but at 11 UTC.

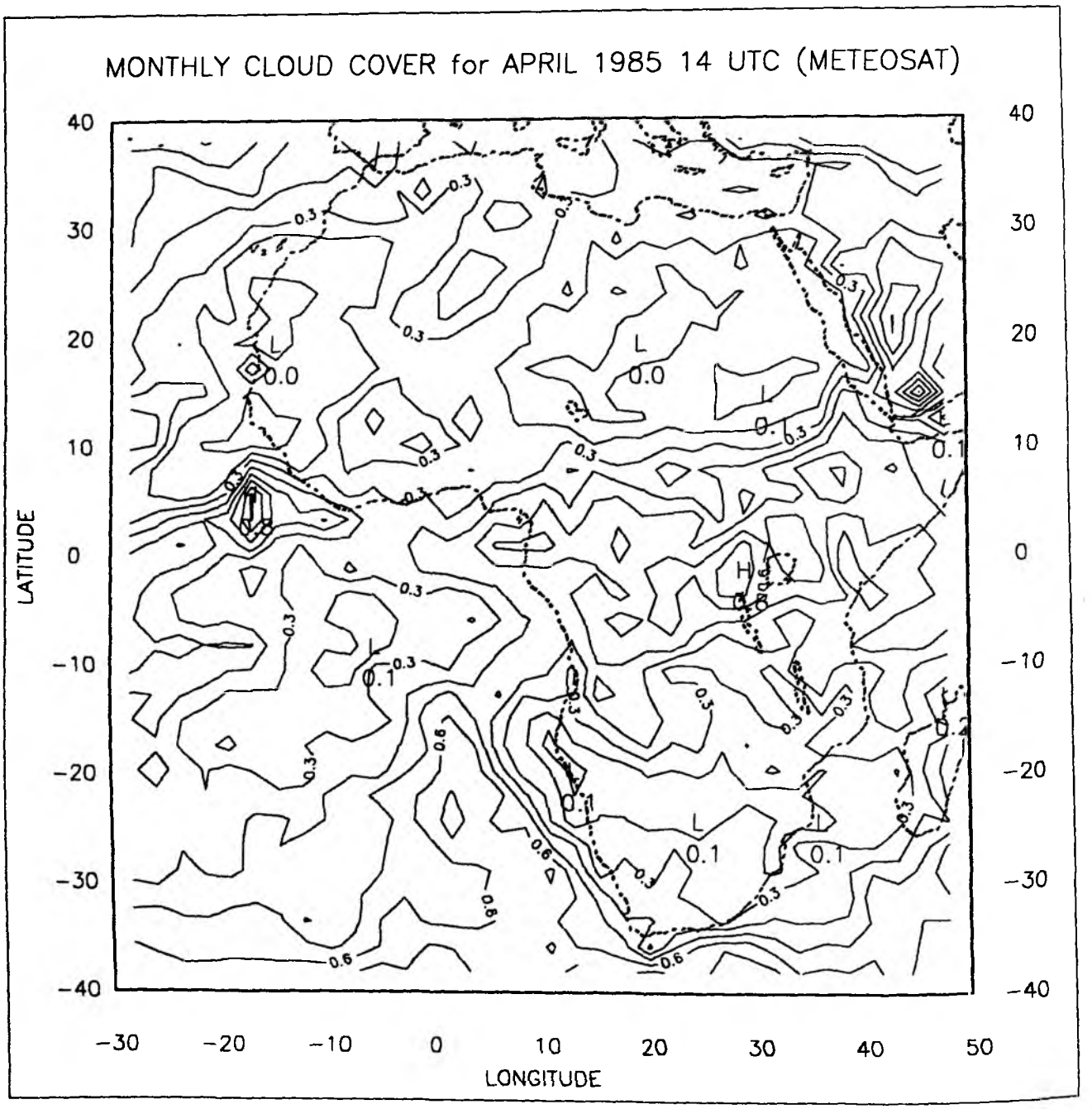

Figure 12f. Same as Fig. 12a but at 14 UTC.

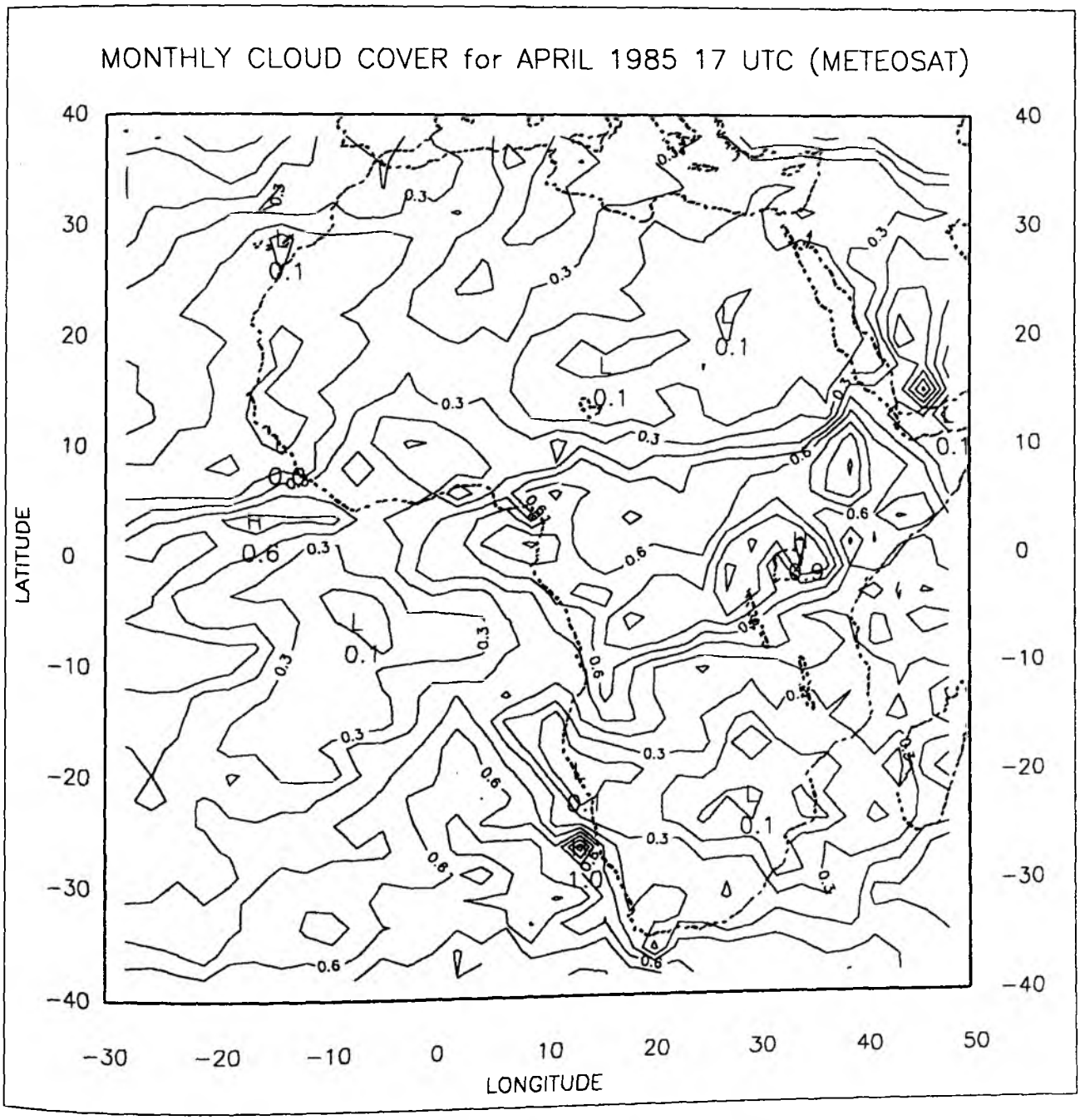

Figure 12g. Same as Fig. 12a but at 17 UTC.

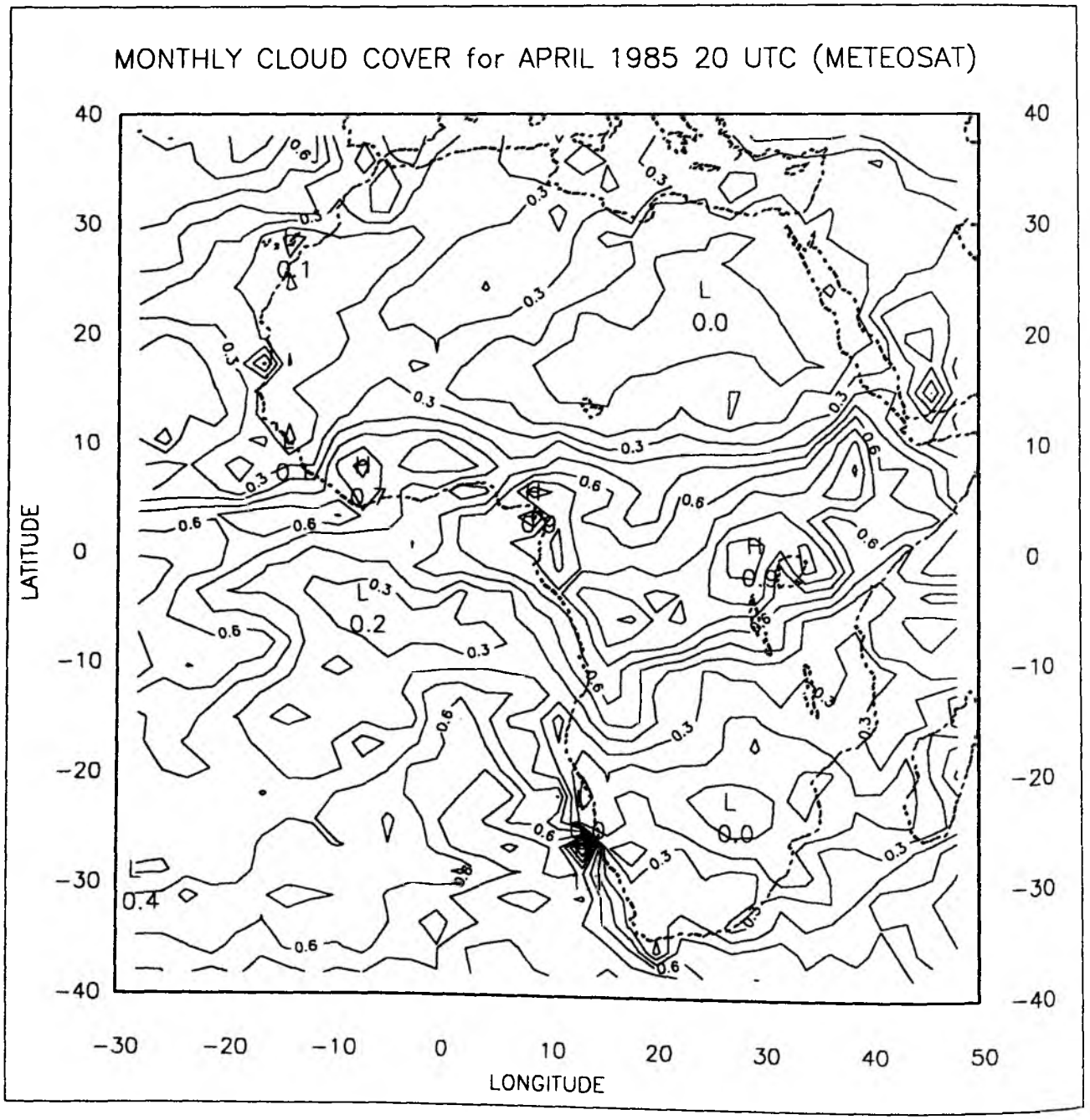

Figure 12h. Same as Fig. 12a but at 20 UTC.

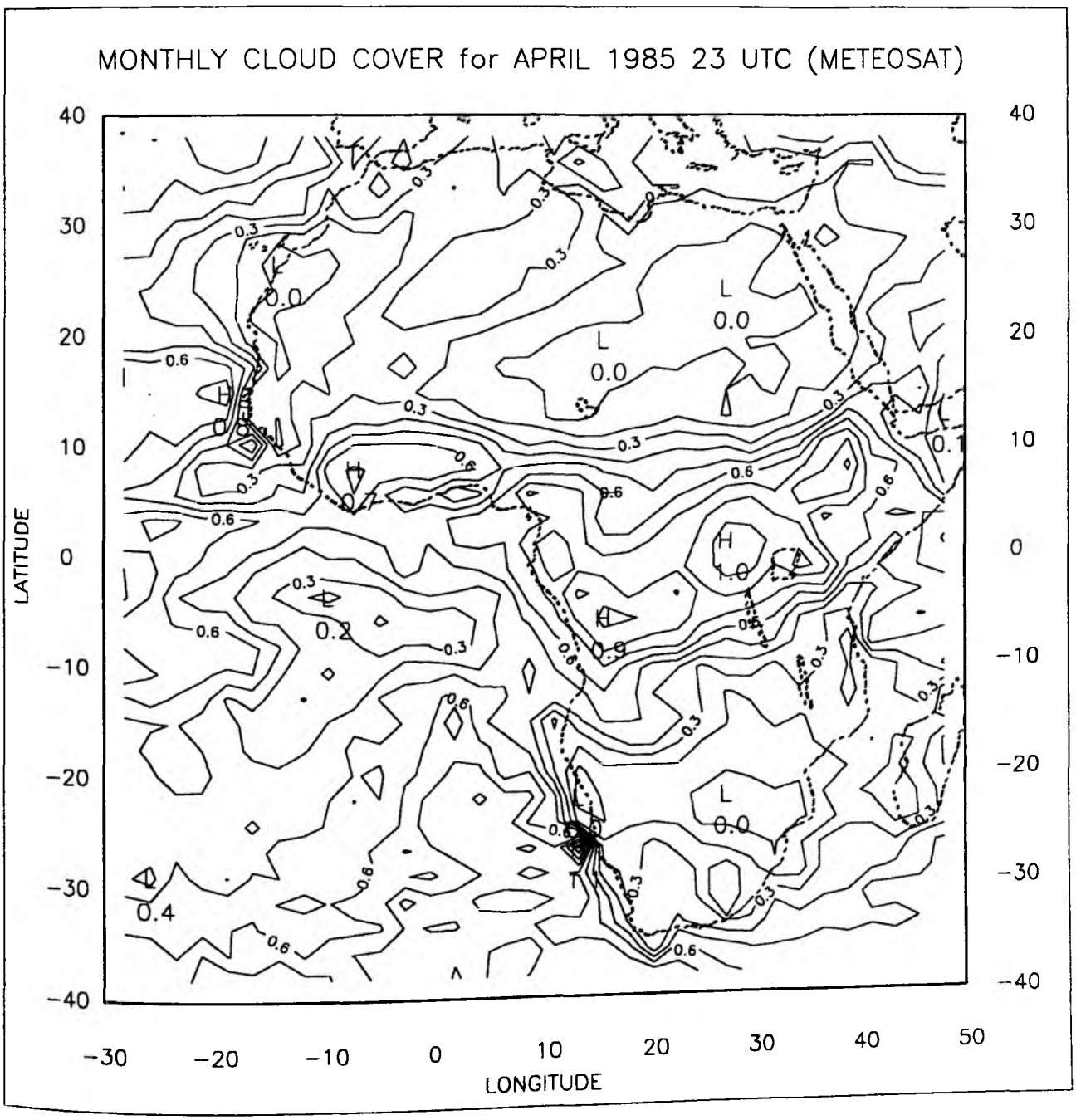

Figure 12i. Same as Fig. 12a but at 23 UTC.

6.2 Cloud forcing

The study of climate and climate change is hindered by a lack of information on the effects of clouds on the radiation budget of the earth, referred to as the cloud-radiative forcing. Here we demonstrate on a few examples how the new data set can be used for this purpose. The longwave cloud-radiative forcing is shown only, and is defined as the difference between the outgoing longwave radiation flux for clear sky and that for the cloudy case. The monthly mean longwave cloud-radiative forcing derived from CDS and from ERBE are given in Fig. 16a-b. Their pattern agree very well, both data sets have maximums and minimums in the same geographical locations. For a large part of the Sahara, the cloud radiative-forcing is less than 5 W/m^2. Exceptions are the region where jet stream cirrus occurs. The largest longwave cloud radiative-forcing appears in the ITCZ and the tropical deep cloud convection regions, which is expected. The monthly averaged longwave cloud-radiative forcing over the METEOSAT observing area (about 50 N - 50 S, 50 W - 50 E) is estimated at 26.2 W/m^2 from the CDS and 29.5 from the ERBE data. The largest differences of more than 10 W/m^2 occur over central Africa in areas of deep convection. That temporal sampling errors partly causes these differences can be shown. This area has been studied in detail. Fig. 17a-h give the monthly mean longwave cloud radiative-forcing for central Africa at 3 hourly intervals (02,05,08,...,23 UTC). The maximum over central east Africa has a large diurnal variation with values around 60 W/m^2 in the morning and over 80 W/m^2 in the late afternoon. However, two polar orbiting satellites, only provide observations 4 times daily (about 01:30,13:00,21:00, 23:00 UTC). This can explain the large differences of OLR and also the cloud radiative-forcing in this region. Therefore, the differences are drastically reduced, when we averaged the CDS results only over the

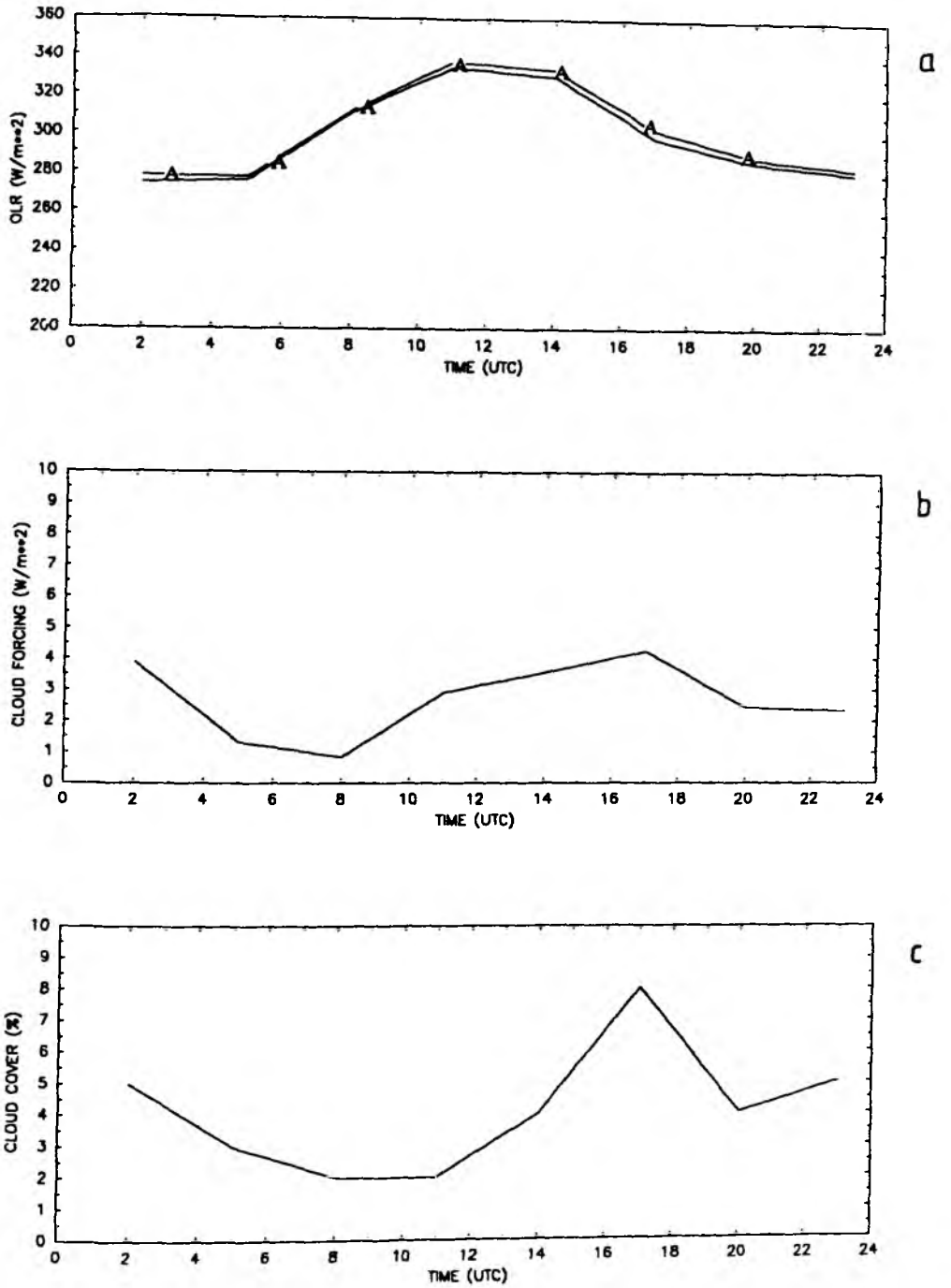

Figure 13.Monthly mean diurnal variation over the desert area at 19.7 °N, 20.8 ° E for April 1985 of a) OLR for clear sky situations (marked with A), and with clouds (solid line), b) cloud forcing, c) cloud cover in %.

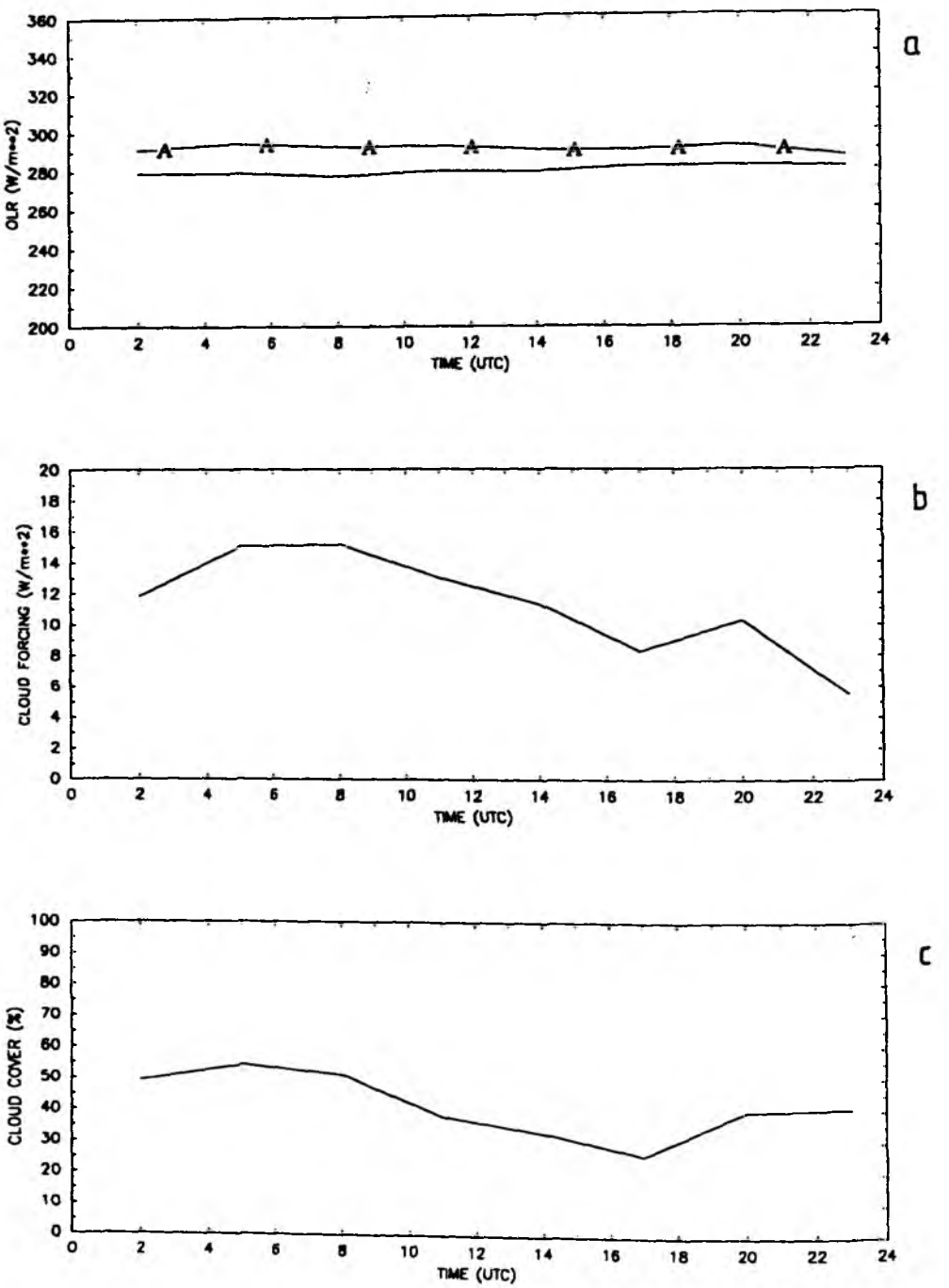

Time (UTC)

Figure 14. Same as Fig. 13, except for a marine stratocumulus region (16.7 ° S, 10.3 ° W).

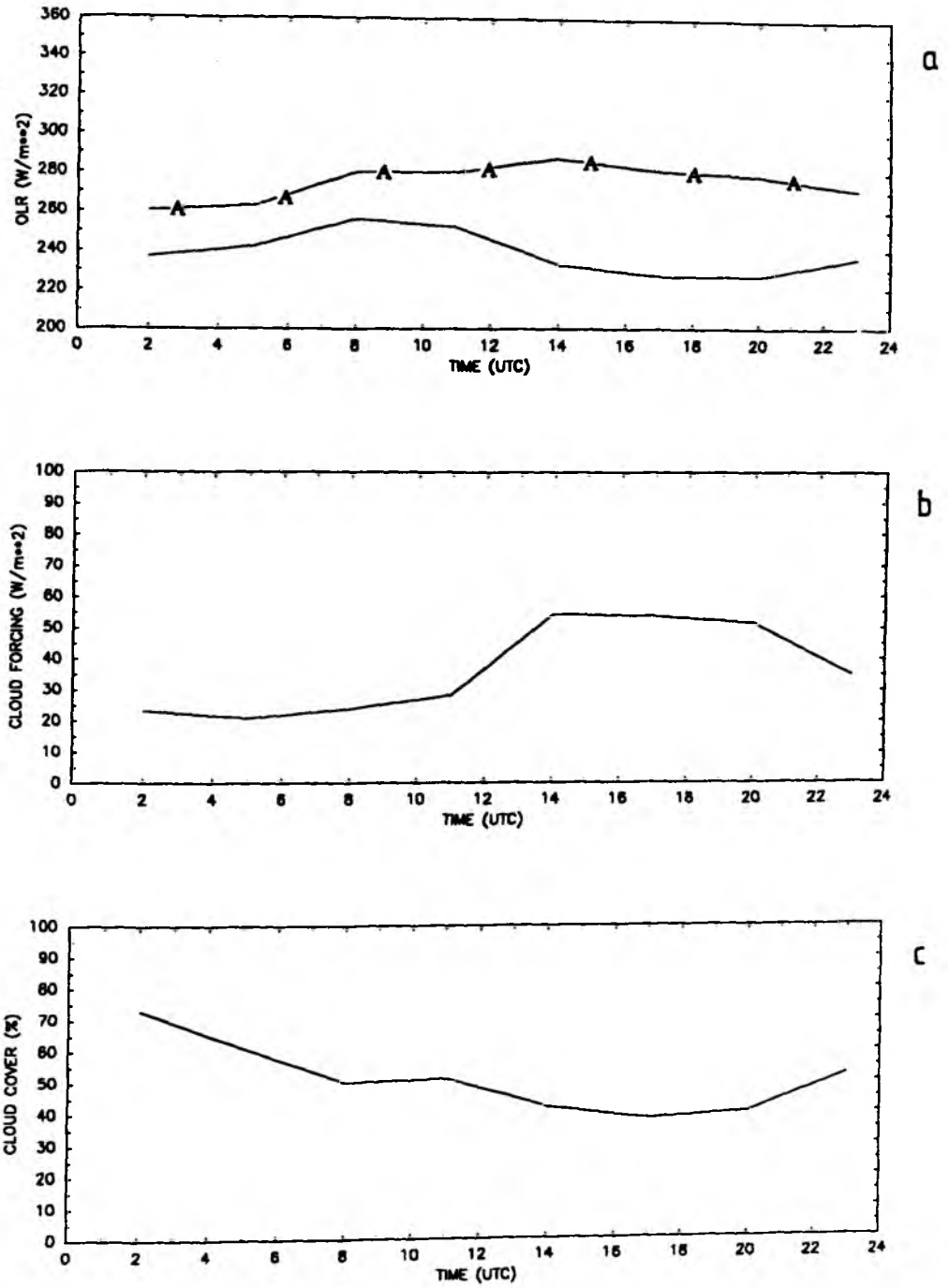

Time (UTC)

Figure 15. Same as Fig. 13, except for a convection area (7.3 ° S, 25.4 ° W).

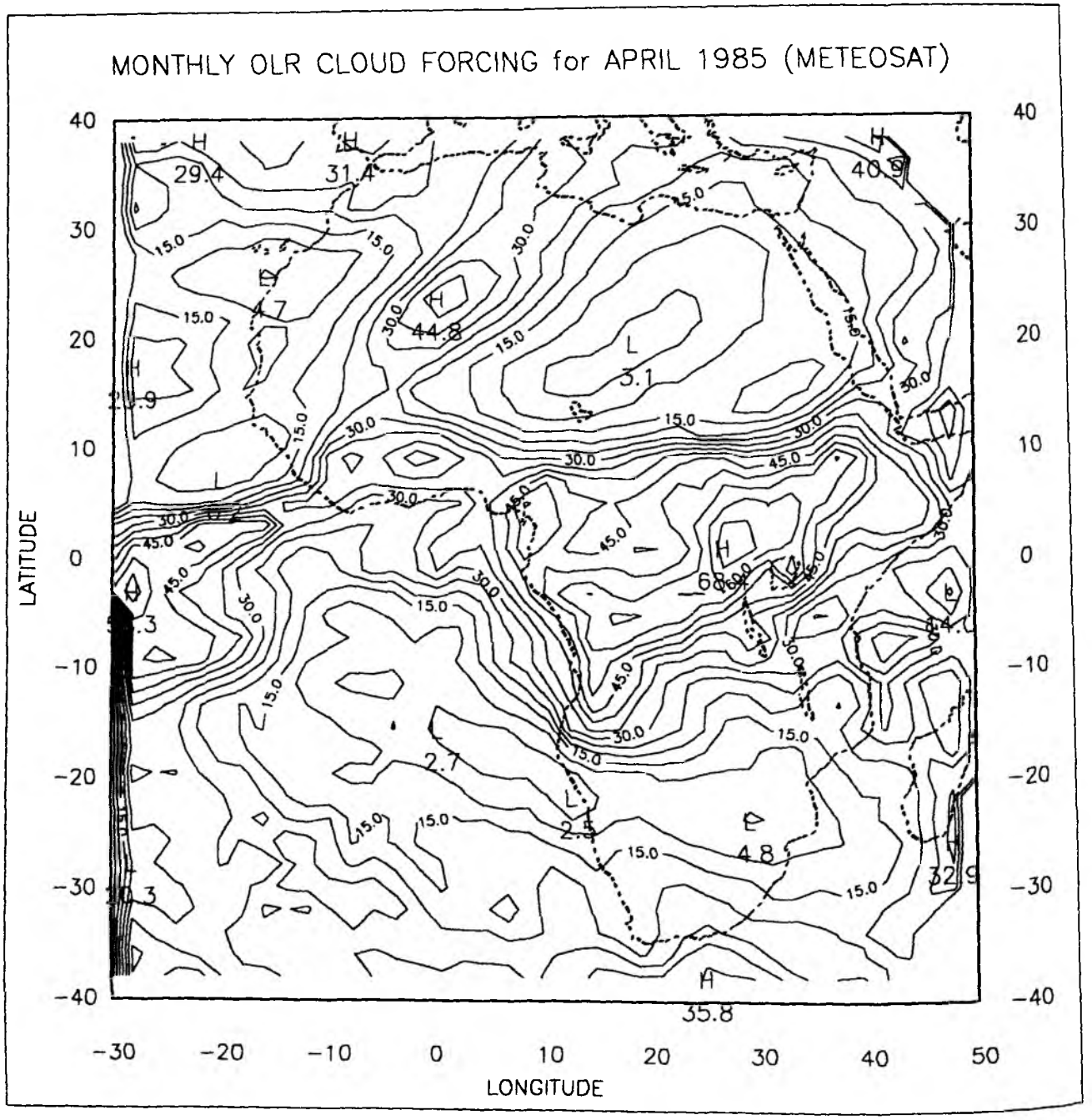

Figure 16a. Monthly mean cloud radiative-forcing (longwave) calculated from the CDS for April 1985. The plot interval is 5 W/m^2.

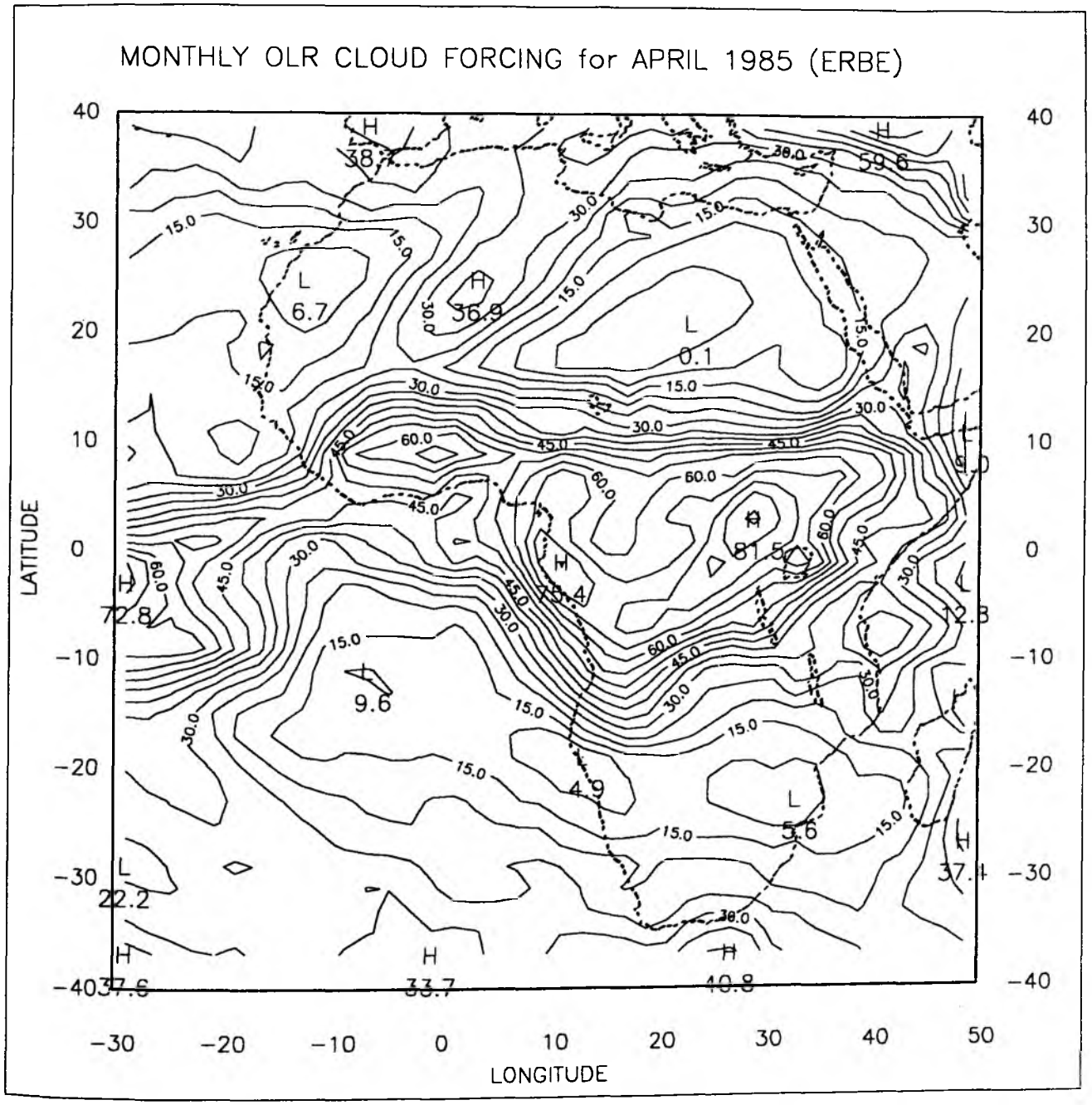

Figure 16b. Monthly mean cloud radiative-forcing (longwave) calculated from the ERBE for April 1985. The plot interval is 5 W/m^2.

4 times 14, 17, 20, and 23 UTC and compare it with ERBE (Figures 18a-c). That means, ERBE might give too large a longwave cloud radiative-forcing in this area. Although the ERBE data are regarded as the best radiation budget data available today, CDS derived OLR are more useful for the study of diurnal variations.

6.3 Net radiation flux and net cloud radiative-forcing

The net radiation flux, or radiation budget at the top of the atmosphere largely varies with season, geography and depends on clouds. The energy emitted by the earth / atmosphere system depends on the temperature and of course on the absorbing gases. The extraordinary importance of water for the heat budget of the earth is obvious for the following reasons. For steep solar incidence, i.e. in the tropical region, the albedo of water is very low, hence absorption of the sun's radiation is high. The polar ice caps with high albedo reflect a large amount of the solar energy and produce a negative radiation budget. Not only the surface with its various albedos affects the global heat budget, in addition the atmosphere is an important and highly variable intervening medium. Water vapour causes wavelength-selective absorption and re-emission of radiation, and clouds cause efficient reflection of visible and infrared radiation due to scattering by droplets. Strong water vapour and cloud concentrations for example take place

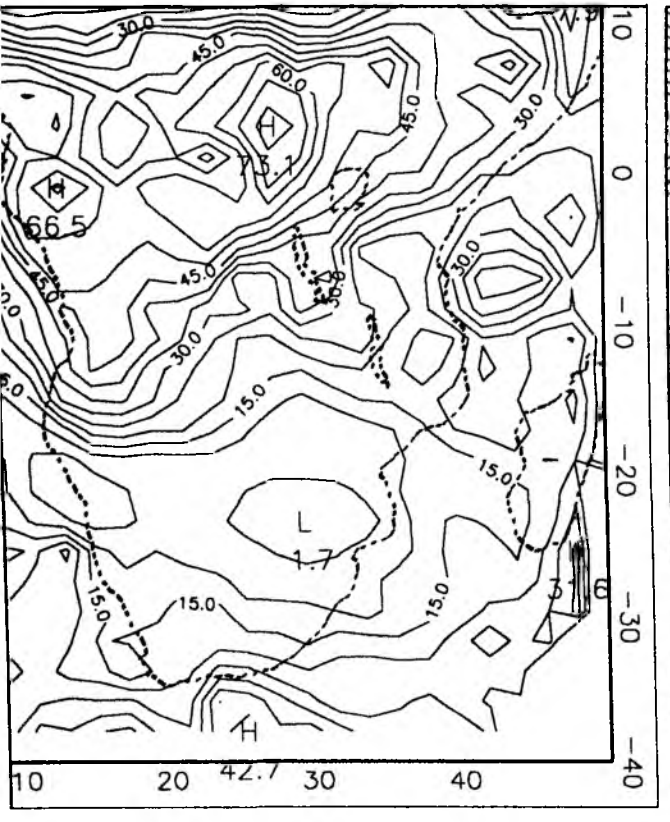

Figure 17a. Monthly mean cloud radiative-forcing over the deep convective cloud area calculated from the CDS at 02 UTC for April 1985. The plot interval is 5 W/m**2.

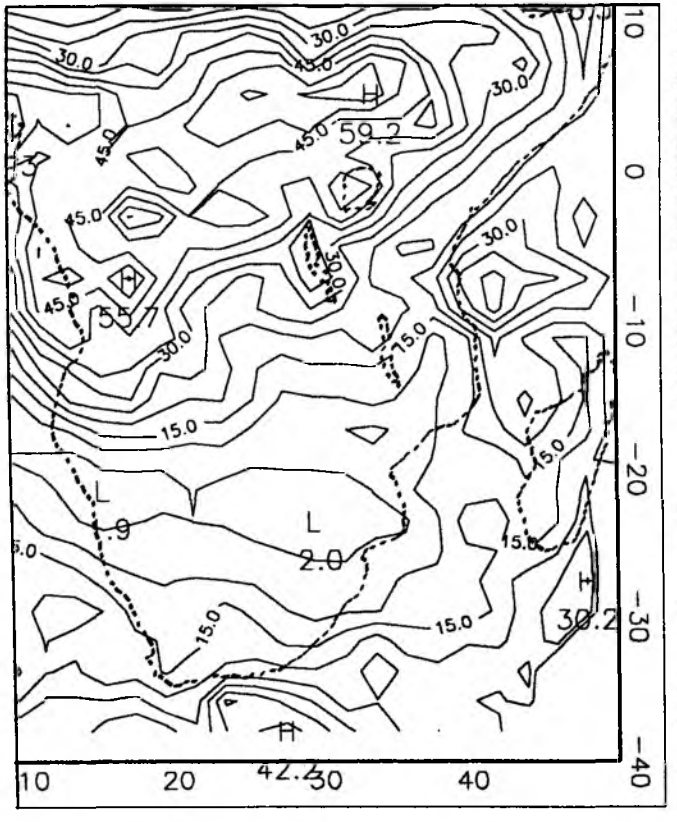

Figure 17b. Monthly mean cloud radiative-forcing over the deep convective cloud area calculated from the CDS at 05 UTC for April 1985. The plot interval is 5 W/m**2.

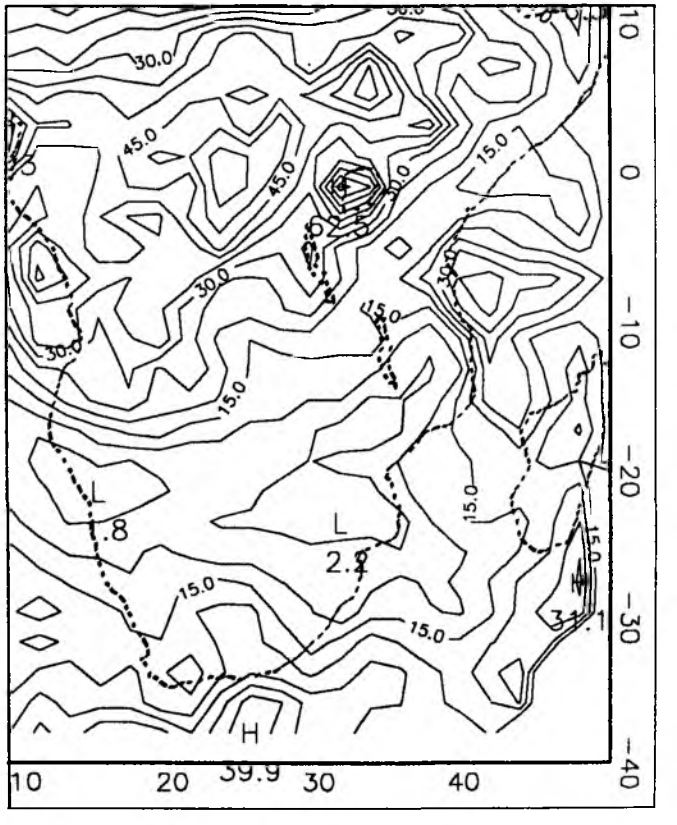

Figure 17c. Monthly mean cloud radiative-forcing over the deep convective cloud area calculated from the CDS at 08 UTC for April 1985. The plot interval is 5 W/m**2.

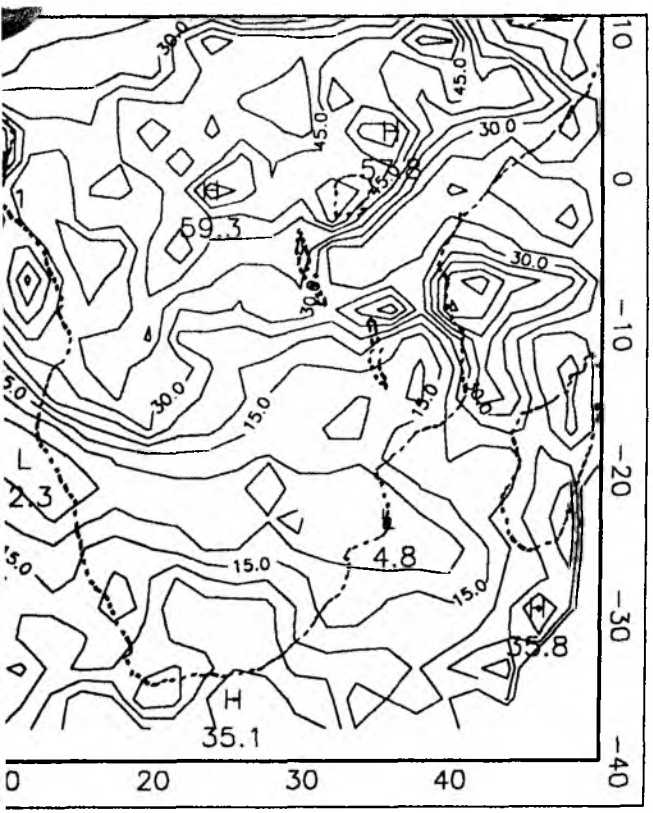

Figure 17d. Monthly mean cloud radiative-forcing over the deep convective cloud area calculated from the CDS at 11 UTC for April 1985. The plot interval is 5 W/m**2.

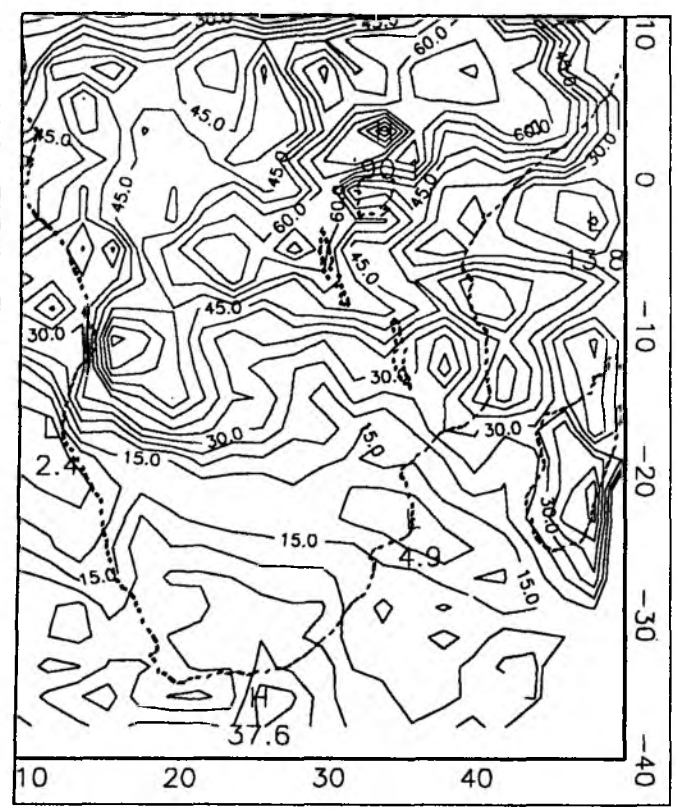

Figure 17e. Monthly mean cloud radiative-forcing over the deep convective cloud area calculated from the CDS at 14 UTC for April 1985. The plot interval is 5 W/m**2.

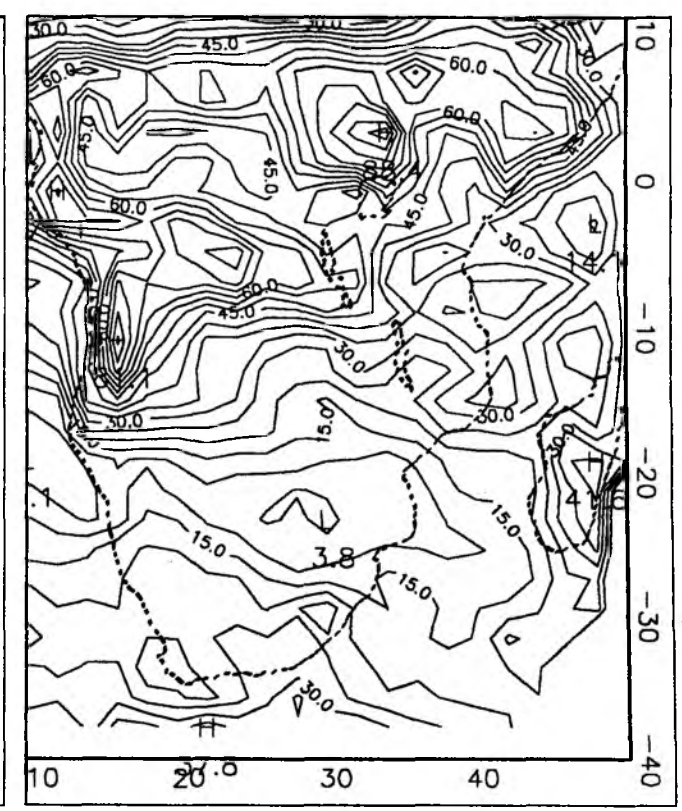

Figure 17f. Monthly mean cloud radiative-forcing over the deep convective cloud area calculated from the CDS at 17 UTC for April 1985. The plot interval is 5 W/m**2.

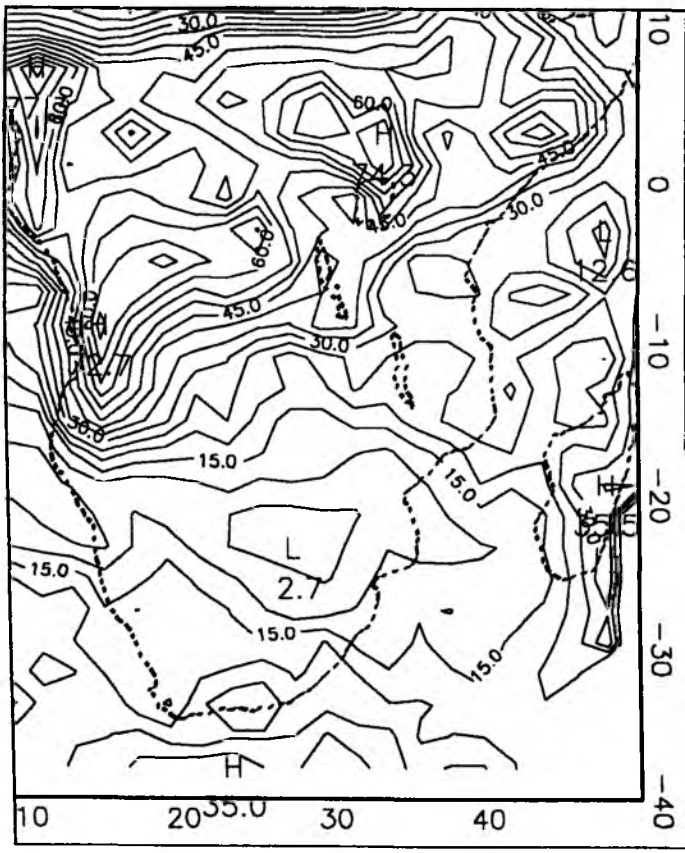

Figure 17g. Monthly mean cloud radiative-forcing over the deep convective cloud area calculated from the CDS at 20 UTC for April 1985. The plot interval is 5 W/m**2.

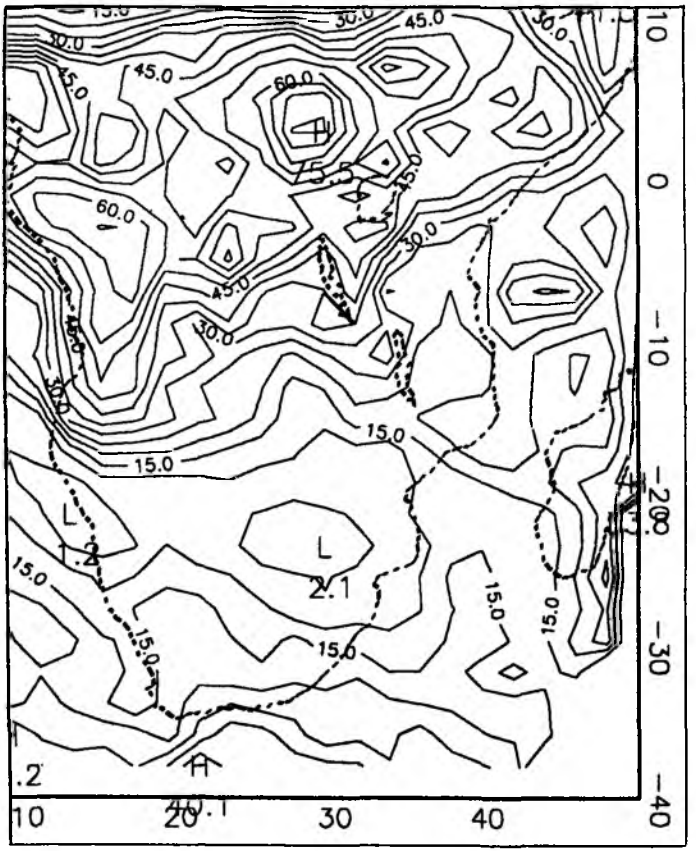

Figure 17h. Monthly mean cloud radiative-forcing over the deep convective cloud area calculated from the CDS at 23 UTC for April 1985. The plot interval is 5 W/m**2.

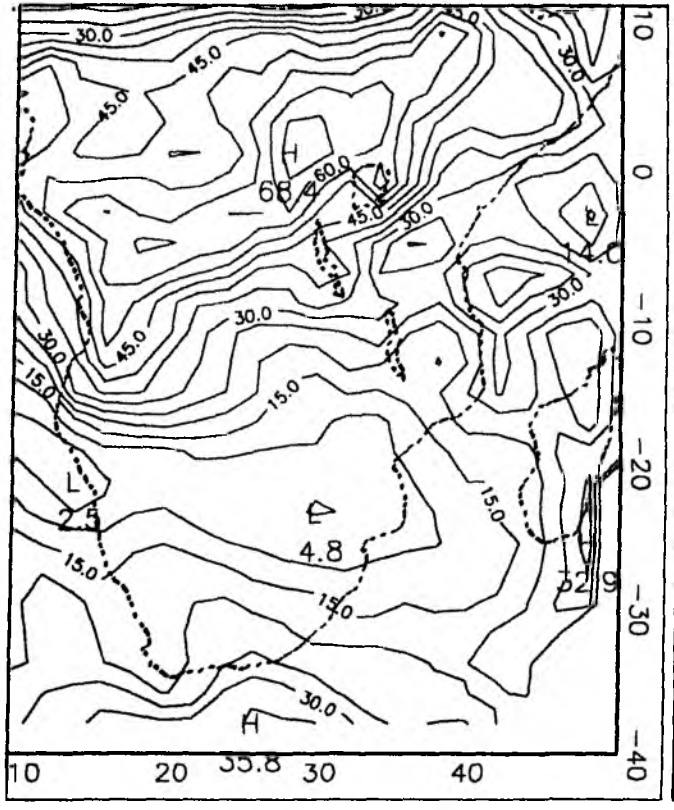

Figure 18a. Monthly mean cloud radiative-forcing over the deep convective cloud area calculated from the CDS for April 1985. The plot interval is 5 W/m**2.

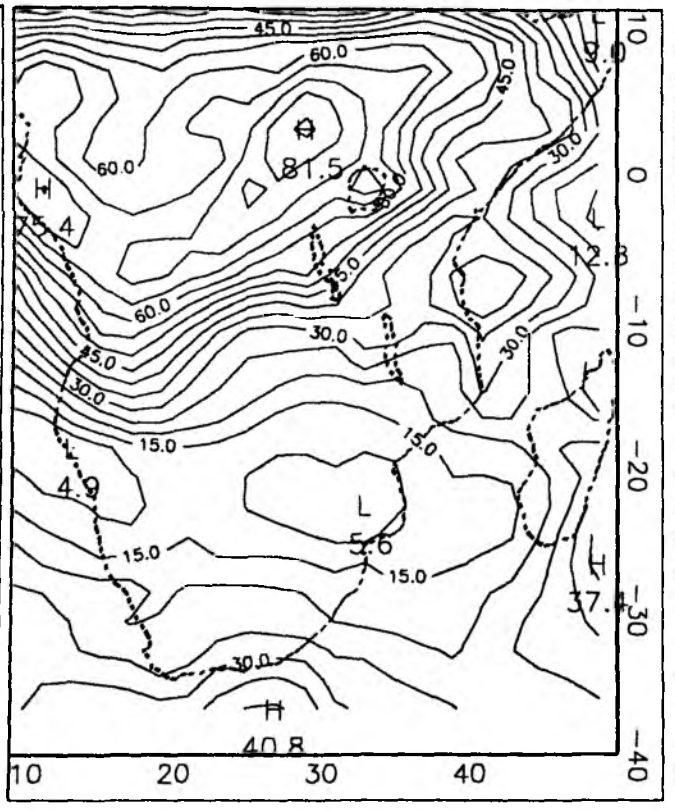

Figure 18b. Monthly mean cloud radiative-forcing over the deep convective cloud area from the ERBE monthly data for April 1985. The plot interval is 5 W/m**2.

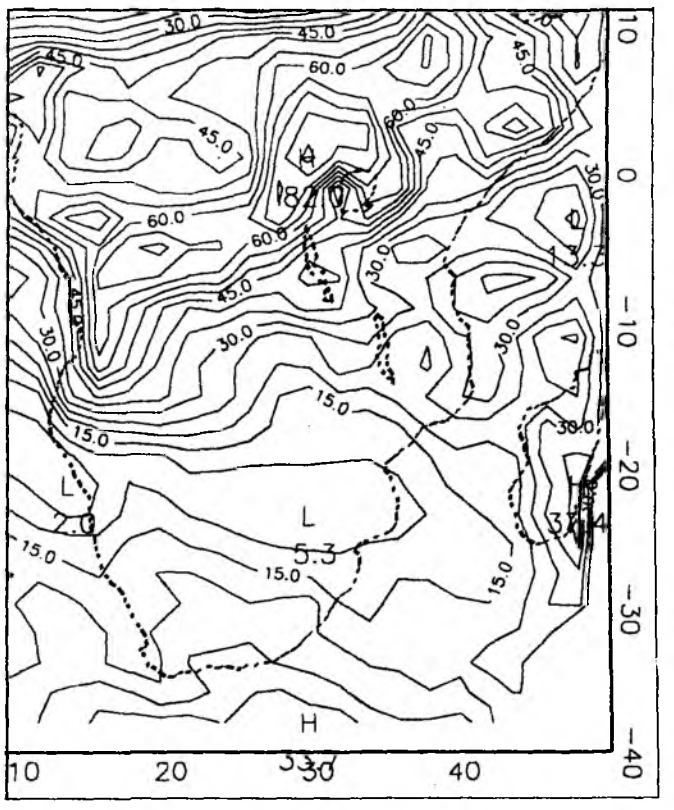

Figure 18c. Monthly mean cloud radiative-forcing over the deep convective cloud area calculated from the CDS at 14, 17, 20 23 UTC . The plot interval is 5 W/m**2.

predominantly in the intertropical convergence zone. The unequal latitudinal distribution of water in the solid, liquid and gaseous state causes an imbalance of the radiative flux of heat on earth (see Fig. 19). This imbalance must be compensated by a poleward transfer of energy in the atmosphere and ocean. Figure 20 (Schanda, 1987) presents the yearly average of this imbalance and consequent transfer, which was done by Iribarne and Cho (1980).

Here we shall discuss the results from April 1985 in detail. In April, the maximum values of insolation lies between 30° N and 0° N (see Fig. 21). For Sahara desert observations show negative net fluxes (see Fig. 22), which are completely different from its zonal average (see Fig. 19). Raschke et al. (1970, 1973) have explained the anomalous cases. Their physical reasons are: 1. high surface albedo (Nacke, 1989), which reflected more than 40% of the incoming solar energy back to space; 2. high surface temperature and low water vapour density, which produces the largest OLR. Therefore, in the Sahara desert the outgoing longwave radiation is larger than the absorbed solar radiation.

Without clouds, the radiation balance of the earth-atmosphere system has a strongly seasonal signal. With clouds, an additional variation is introduced. Ramanathan et al. (1989) found that the magnitude of the observed net cloud forcing is about four times as large as the expected radiative forcing from a doubling of CO2. The shortwave and longwave components of clouds forcing are about 10 times as large as those for a CO2 doubling. Therefore, cloudiness is pivotal variable for the radiation budget. Clouds reflect incoming solar radiation, therefore reducing absorbed solar radiation. On the other hand they absorb longwave radiation emitted at relatively high temperature by the Earth's surface. They then reradiate to space at lower temperatures, depending on cloud height and optical thickness. Since clouds have two competing

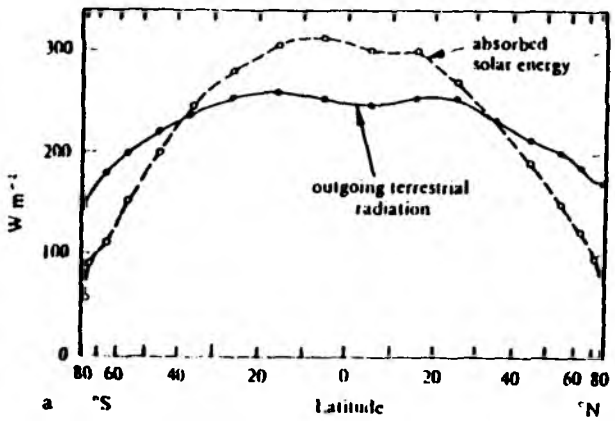

Figure 19. Solar energy absorbed and terrestrial radiative energy emitted by earth-atmosphere system (Von der Haar and Suomi, 1971).

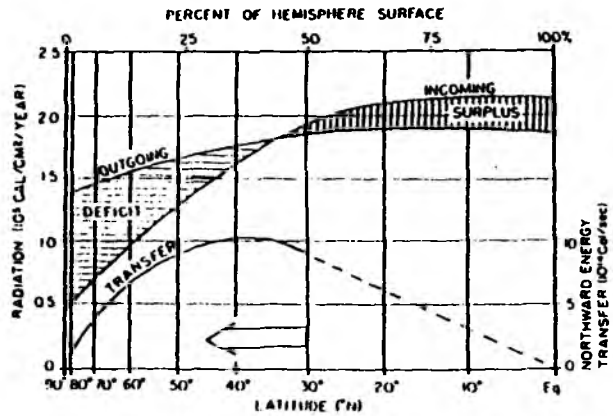

Figure 20. Meridional transport of energy. (Schanda, 1987)

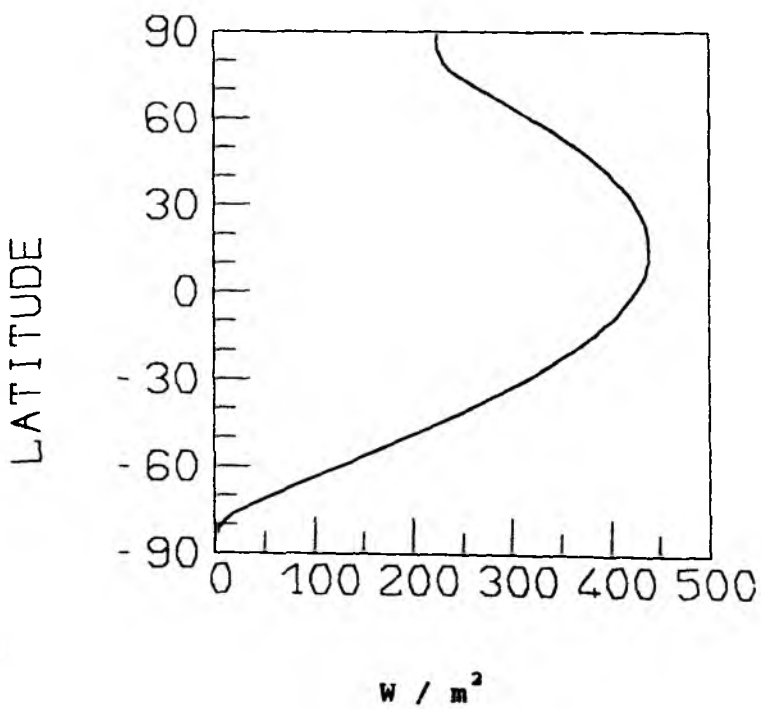

Figure 21. Latitudinal variation of solar insolation for April.

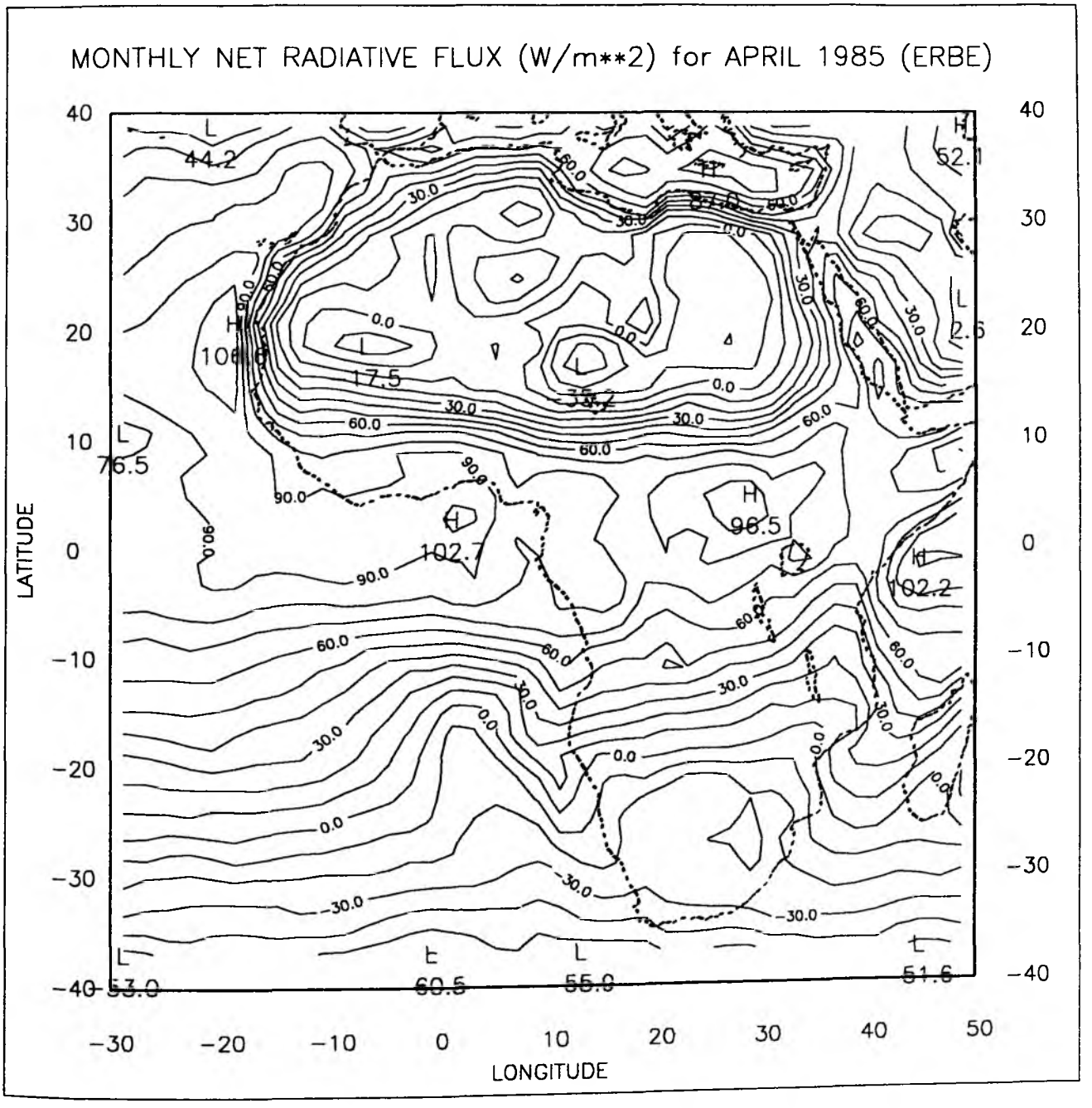

Figure 22. Net radiation flux from the ERBE data for April 1985. The plot interval is 10 W/m^2.

effects on the earth radiation balance budget, there is a key climatic question whether clouds, on the average, increase or decrease the earth net radiation. Globally and annually, clouds produce a net cooling of Earth-atmosphere system (Harrison et al., 1990) (increase CO2 produces a net warming). For April 1985, clouds reduce net radiation flux from 22.1 W m^{-2} to 4.8 W m^{-2} (net radiation flux = absorbed solar energy - emitted longwave radiation flux). This difference of -17.3 W m^{-2} equals to the net cloud radiative-forcing. It is composed of the longwave component and the shortwave component ot cloud forcing. Locally, clouds could produce a net warming or cooling. Negative net cloud radiative-forcing occurs primarily over marine stratocumulus system (see Fig. 23). Since marine stratocumulus contain low clouds, the longwave cloud forcing is small (see Fig. 14). But it does produce a large shortwave cloud forcing. Thus the clouds can not be well developed when considering radiative energy only. But other factors (e.g. latent energy of clouds, convergence of air mass) could develop the stratocumulus. For the African area of deep convection the negative net cloud forcing is due to the fact that the clouds are very thick so that shortwave component of cloud forcing is larger than that of longwave component. The negative net cloud forcing should hinder convection, while METEOSAT observations(Fig. 15 and Figs. 17a-h) show a strong cloud convection in afternoon. Therefore, convergence below the clouds must exist. The convergent air mass is from Sahara desert. Generally, cloud development cannot be determined from the cloud radiative-forcing alone since many factors affect clouds. The positive net cloud radiative-forcing appears in areas where cirrus associated with jet stream occurs (e.g. 30° N, 0° E). The optical thin cirrus clouds are not in contrast to the high surface albedo so that they cannot be seen at the figures of planetary albedo (see Figs. 11a,b). They are clearly recognized in OLR distributions (see Fig. 7a,b). Thus the longwave component of cloud forcing is larger than that in the shortwave part.

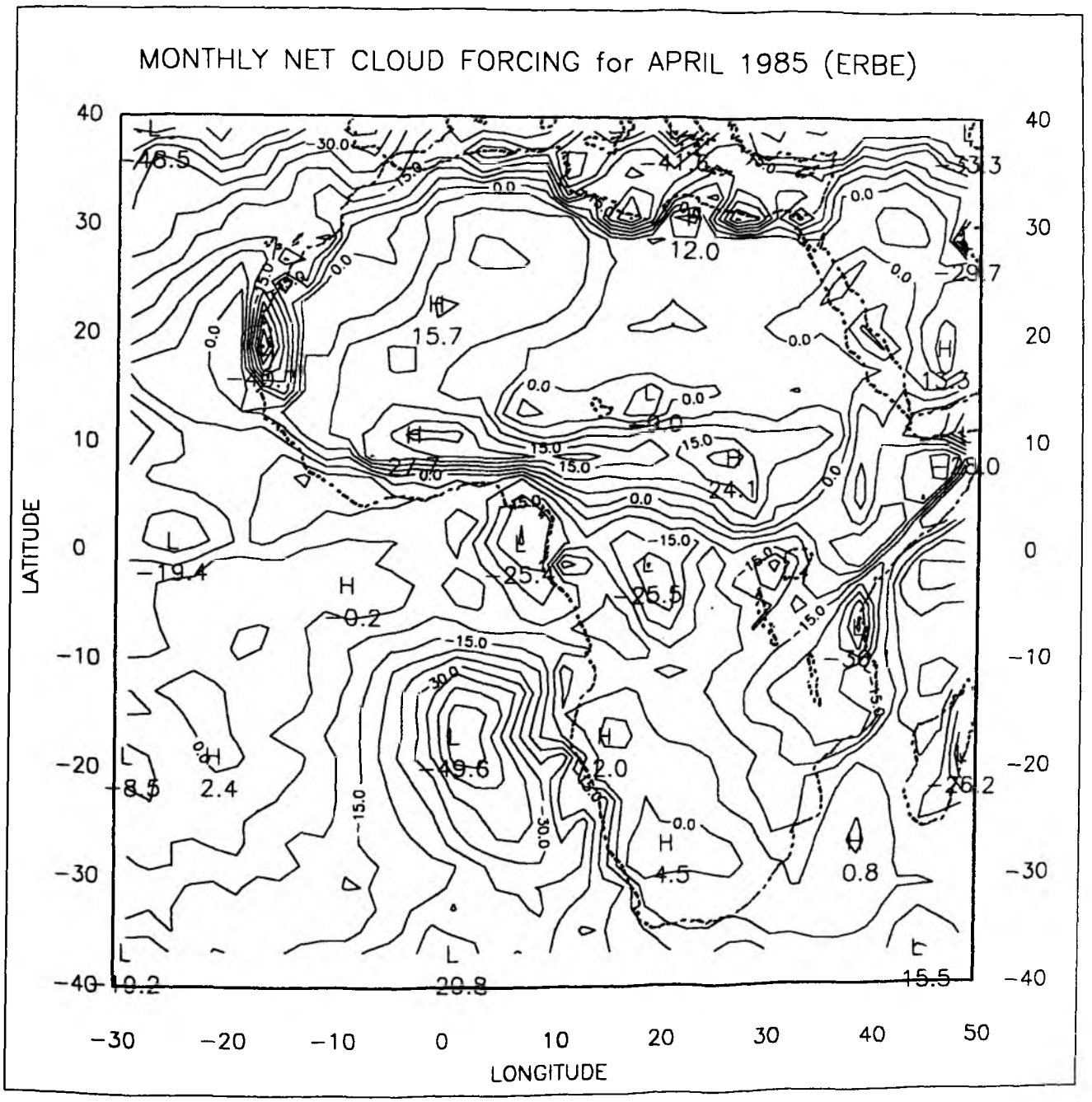

Figure 23. Net cloud radiative-forcing from the ERBE data for April 1985. The plot interval is 5 W/m^2.

7. Conclusion

The outgoing longwave radiation flux (OLR) estimated from the METEOSAT Climate Data Set shows a good agreement with the ERBE OLR with a RMS of 6.9 W/m^2 for monthly mean values of April 1985. Thus the OLR estimated from the CDS meets the accuracy required for applications. For the tropical deep cloud convection area, the longwave cloud-radiative forcing from the ERBE data might be too high due to the fact that there are no ERBE observations between morning and noon. The longwave cloud-radiative forcing between morning and noon in this region is smaller than that in afternoon. METEOSAT suffers from shortcomings in the calibrations and uncertainties related to the influence of broadband fluxes from the filtered narrowband radiances, where errors could appear in the present regression technique.

The monthly mean planetary albedo estimated from the CDS for April 1985 shows also a good agreement with the ERBE results. Both data sets have the same structures e.g. the same geographical locations for maxima and minima . Comparisons of the monthly mean planetary albedo of the two data sets give a RMS of 3.6 % and a bias of -2.4 % . The deviation is probably related to the time sampling of the CDS which on average only provides 3 useful measurements around noon . This appears to be insufficient for deriving the monthly mean planetary albedo. The negative bias is to be expected since the 3 measurements around noon from the CDS, generally give a minimum planetary albedo. The cloud contamination of the CDS is not a critical problem for the OLR estimation (though it is a serious problem for studying the longwave cloud-radiative forcing), but is problematic for estimating the planetary albedo from the CDS since the estimation algorithm is scene dependent. The calibration error of METEOSAT VIS also causes uncertainties. Nevertheless the guaranteed continuity of observations from operational meteorological satellites qualifies those radiation observations as a useful complement to dedicated scientific

experiments like ERBE. The usefulness will be enhanced with the advent of a new generation of satellite with better calibration and more imaging channels, the latter potential giving better scene identification. The bidirectional model needs also to be improved.

8. Suggestion for further work

Although the present study demonstrated that the estimated outgoing longwave radiation flux from the METEOSAT CDS achieves the required accuracy for applications, technical improvements to the radiometer can reduce the errors. The METEOSAT water vapour channel observations improve the accuracy of the OLR estimation from the CDS, although this 6.3 μm water vapour channel only accounts for about 3% of the OLR. This is because the emission of the 20 - 40 μm water vapour absorption band, which contributes about one third to the OLR , is highly correlated to the emission in the WV channel. Using both IR and WV observations, reduces the bias of the clear sky OLR estimations from -8.2 W/m^2 (9.8 W/m^2 for cloud case), to 0.0 W/m^2 (2.4 W/m^2 for cloud case) . More imaging channels would improve the accuracy of OLR estimates derived from METEOSAT data.

For opaque water clouds, the results obtained from the present regression technique, using the same regression coefficients as for clear sky, and from the Matrix-Operator-Method with scattering for arbitrary viewing zenith angles agree within 2 W/m^2 (see table 12). This means the regression coefficients in the longwave part for clear sky are stable and suitable for clear sky and opaque clouds. It is recognized from radiation model calculations that the present regression algorithm overestimates the OLR for very thin clouds at small viewing zenith angles and underestimates at large viewing zenith angles(see figure 19). It is also recognized that the surface emissivity in the longwave part could modify the

outgoing longwave radiation flux(see figure 20). To consider these effects, more imaging channels are required. Further studies on this topic are warranted.

Table 12. Comparison of OLR for the atmosphere with a opaque water cloud layer between 547 - 627 h Pa calculated with the same regression equation but different coefficients A: regression coefficients for clear sky and B: regression coefficients for cloudy cases for different satellite zenith angle θ. OLR from Matrix-Operator-Method calculation is 213.76 W/m^2 .
Cir, Cwv = percent contribution to OLR from IR, WV channel respectively.

θ in degree	A			B		
	OLR	Cir	Cwv	OLR	Cir	Cwv
0.	215.17	74.6	25.4	212.35	43.0	57.0
14.	215.18	74.6	25.4	212.41	43.0	57.0
25.	215.14	74.6	25.4	212.50	43.0	57.0
37.	215.09	74.5	25.5	212.68	43.0	57.0
49.	214.88	74.4	25.6	212.89	43.0	57.0
60.	214.24	74.3	25.7	213.06	43.0	57.0

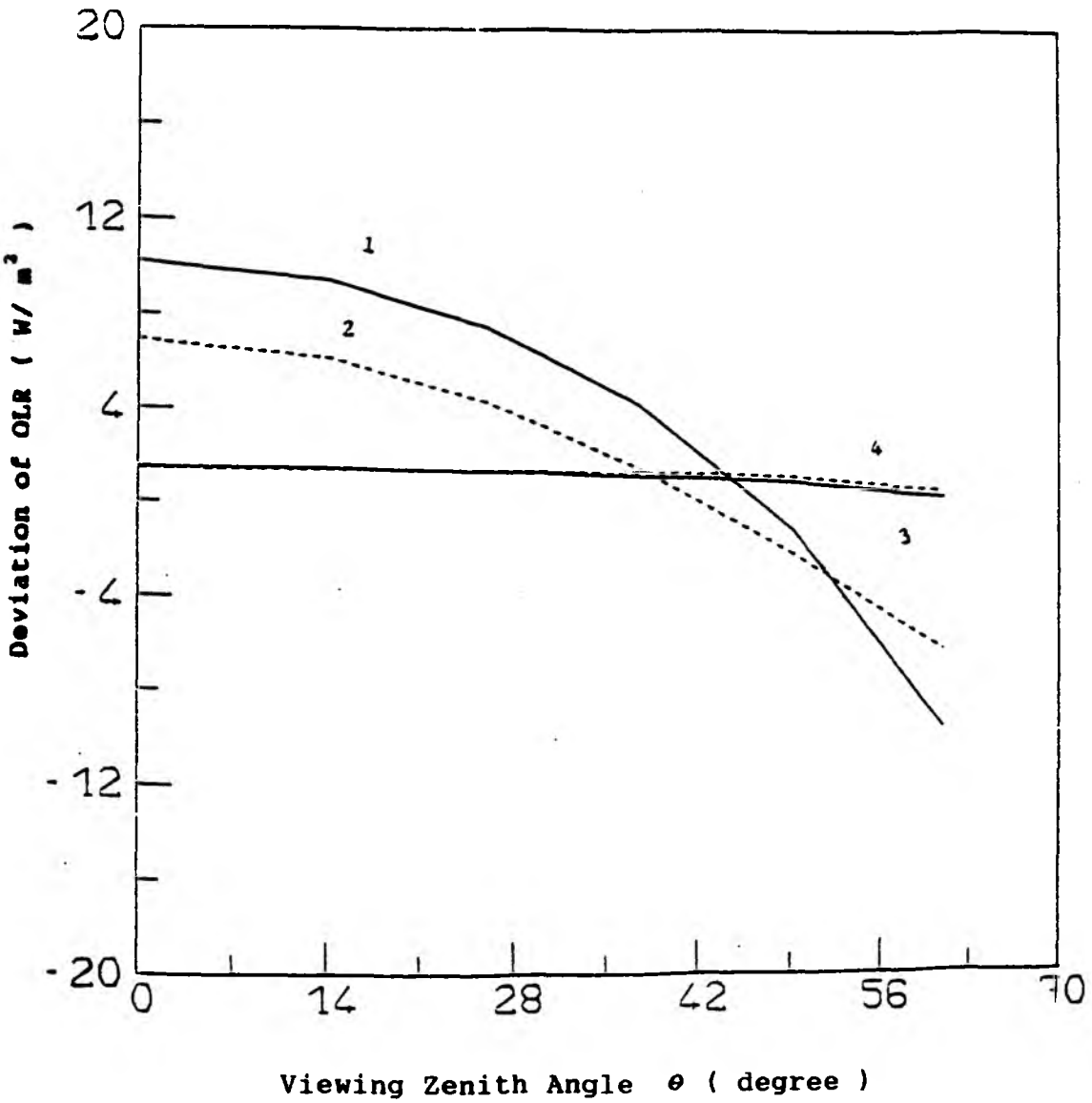

Figure 24. Deviations of the OLR calculated with the regression technique from the Matrix-Operator-Method calculations as a function of the viewing zenith angle θ for the tropical dry summer atmosphere with a water cloudy layer between 500 hPa and 630 hPa.
Curve 1 with cloud optical depth δ = 0.66 at λ =10.55 μm.
Curve 2 with cloud optical depth δ = 1.98 at λ =10.55 μm.
Curve 3 with cloud optical depth δ = 6.6 at λ =10.55 μm.
Curve 4 with cloud optical depth δ = 66 at λ =10.55 μm.

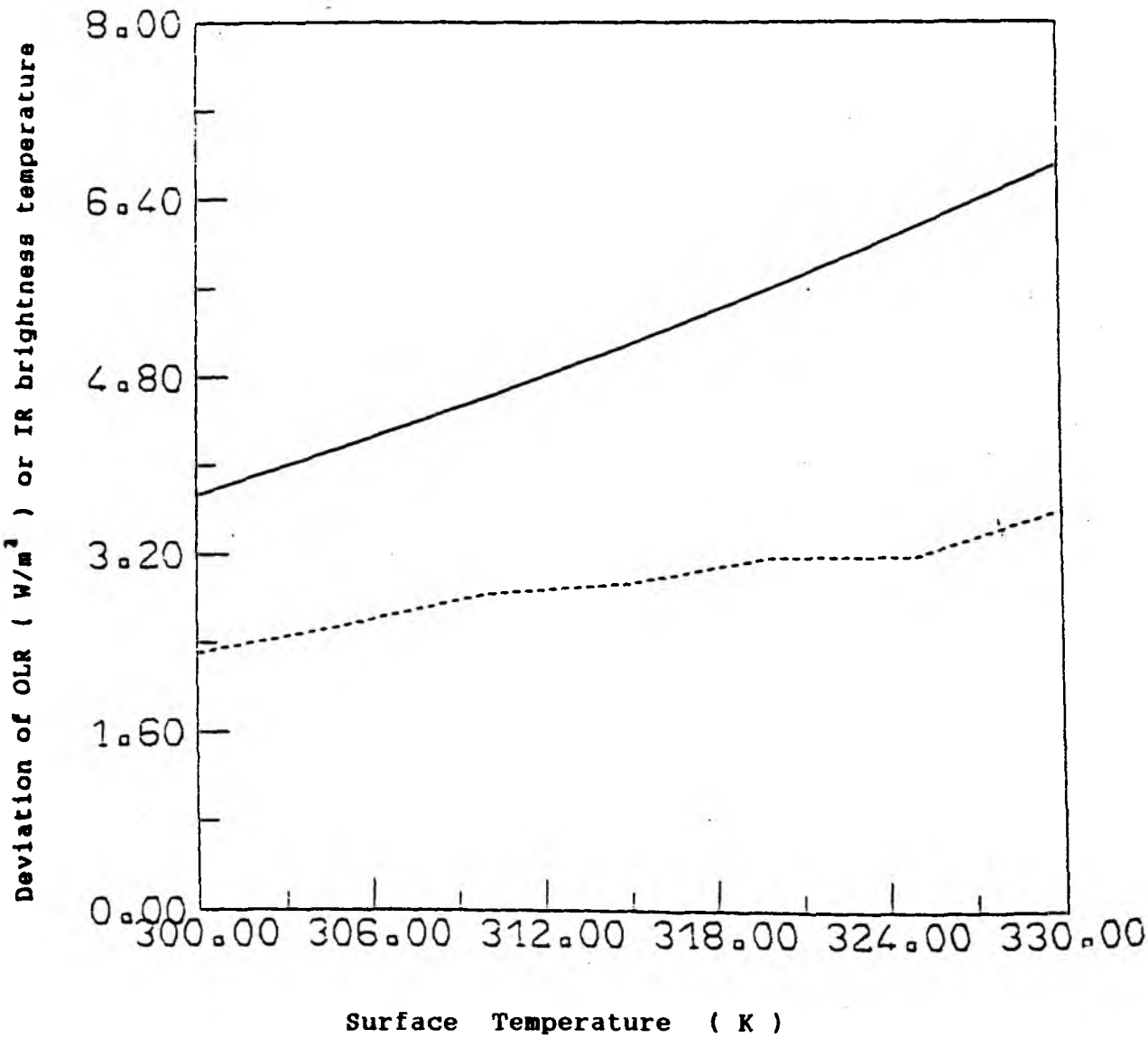

Figure 25. Difference between IR brightness temperatures (dashed line) at the top of the atmosphere (nadir viewing) and between the OLR (solid line) for different surface emissivities (ε = 1 and ε = 0.9) for a tropical dry summer atmosphere as a function of surface temperature.

For the planetary albedo estimation, a new generation of satellite with onboard calibration and more observing channels would be advantageous. Suggestions for future work, using data from the current generation of METEOSAT satellites, are as follows:

1. Include water vapour amount in the conversion factor(Eq. 4.2.6) to improve the conversion accuracy from METEOSAT filtered narrowband VIS radiance into the solar broadband radiance. The conversion factor may be extended thus:

$$F^{*}_{sol} = F_{sol} + a_7 \, (W - 3 \text{ cm}) + a_8 \, (W - 3 \text{ cm})^{2} \qquad (8.1)$$

The water vapour amount W can be obtained from ancillary data (e.g. forecasting profiles).

2. Improve the look-up tables using a better resolution geography, with collocated mean aerosol types , better atmospheric profiles, and surface reflection factors. At the same time, that requires METEOSAT data to provide more scenes with the high resolution geography.

3. Include in the look-up table ice clouds and water clouds with various cloud thicknesses over different surfaces.

4. Increase the angle resolution in the radiation transfer model to a 5 degree interval for both zenith angles and sun/satellite relative azimuth angle(present interval is about 11 degree for the zenith angles and 15 degree for the relative azimuth angle).

5. Use daily METEOSAT VIS, WV and IR observations to determine the optical depth and temperature of the clouds, and temperature of the surface by regression techniques and the look-up tables for middle and high clouds, which influence the accuracy for the OLR estimations. The low clouds have little effect on the OLR estimation. This treatment might also improve the accuracy of the planetary albedo estimation.

6. Calculate several regression coefficient sets for the OLR estimation for different surfaces especially for the desert area, where a hot surface skin temperature and a surface emissivity of about 0.87 can occur.

Danksagung

Meinem Doktorvater, Herrn Prof. Dr. Ruprecht, danke ich für viele Anleitungen und für die Betreuung dieser Dissertation.

Herrn Dr. J. Fischer bin ich dankbar, daß er mir das Strahlungstransportmodell überließ.

Bei Herrn Dr. C. Simmer möchte ich mich für viele hilfreichen Diskussionen bedanken.

Bei Frau Dr. Gudrun Nacke möchte ich mich für viele Hilfe in Computer und Strahlungstransportmodell bedanken.

Mein besonderer Dank gilt Dr. J. Schmetz aufgrund vieler richtungsweisender Diskussionen über diese Arbeit.

Abschließend sei der European Space Agency (ESA) gedankt, die diese Arbeit unter dem Vertrag (No. 7905/88/D/ MD (SC)) finanziell unterstützt hat.

Annex

Acronyms and Abbreviations

CDS	Climate Data Set
ERBE	Earth Radiation Budget Experiment
ERBS	Earth Radiation Budget Satellite
ESSA	Environmental Sciences Service Administration
GKSS	Gesellschaft für Kernenergieverwertung in Schiffbau und Schiffahrt mbH
IR	Infrared
ISCCP	International Satellite Cloud Climatology Project
LW	Longwave
MOM	Matrix-Operator-Method
MRIR	Medium Resolution Infrared Radiometer
NASA	National Aeronautics and Space Administration
NOAA	National Oceanics and Atmospheric Administration
OLR	Outgoing Longwave Radiation Flux
RTM	Radiation Transfer Model
TIROS	Television Infrared Observational Satellite
VIS	Visible
WV	Water Vapour

References

Abel, P. G., and A. Gruber, 1979: An improved model for the calculation of longwave fluxes at 11 um, NOAA Tech. Rep., NESS 106, 24 pp.

Abramowitz, M., amd I. A. Stegung, 1965: Handbook of Mathematical Functions. Dover Pub., Inc., New York, 1046 pp.

Arking, A., and S. Vemury, 1984: The Nimbus 7 ERB data set: A critical analysis. J. Geophys. Res., 89, D4, 5089-5097.

Barkstrom, B. R., and G. L. Smith, 1986: The Earth Radiation Budget Experiment (ERBE), Bull. Am. Meteorol. Soc., 65, 1170-1185.

Bowker, E.D., and Richard E. Davis, 1985: Spetral Reflectances of Natural Targets for Use in Remote Sensing Studies., NASA Reference Publication 1139.

Cheruy , F., R.S. Kandel, and J. P. Duvel, 1990: Outgoing Longwave Radiation and its diurnal variation from combined ERBE and METEOSAT observations. Submitted to J. Geophys. Res.

Cox, C., and W. Munk, 1954: Measurement of Roughness of Sea Surface from Photographs of Sun's Glitter. J. Opt. Soc. Am., 44 , 838-850.

D'Almeida, G. A., 1987: On the variability of desert aerosol radiative characteristics., J. Geophys. Res., 92(D3), 3017-3026.

Deirmendjian, D., 1969: Electromagnetic scattering on spherical polydispersions, American Elsevier Publ. Co., Inc., New York, 290 PP.

Duvel, J. P., and R.S. Kandel, 1985: Regional-Scale diurnal variations of outgoing infrared radiation observed from METEOSAT. J. Clim. Appl. Meteorol., 24, 335-349.

Eaton, F. D., and I. Dirmhirn, 1979: Reflected irradiance indicatrices of natural surfaces and their effect on albedo. Appl. Optics,18,994-1008.

Fischer, J., and H. Grassl, 1984: Radiative transfer in an atmosphere-ocean system: an azimuthally dependent matrix-operator approach. Appl. Optics, 23, 1032-1039.

Gaertner, V., 1989: MIEC IR calibration coefficients derived from cloud free sea pixels, Proc. of the Seventh METEOSAT Scientific User' Meeting, Madrid, Eumetsat, EUM P 04, 15-18.

Grassl, H., 1976: A New Type of Absorption in the Atmospheric Infrared Window due to Water Vapor Polymers. Beitr. Phys. Atmosph., 49, 225-236.

Gruber, A., and J. S., Winston, 1978: Earth radiative heating based on NOAA scanning radiometer measurements. Bull. Am. Meteorol. Soc., 59, 1570-1573.

Gube, M., 1982: Planetary Albedo Estimates from Meteosat. ESA JOURNAL, 6, 53-69.

Hale, G. M., and M. R. Querry, 1973: Optical constants of water in the 200-nm to 200-um wavelength region. Appl. Optics, 12, 555-563.

Hansen, J. E., 1971: Multiple scattering of polarized light atmospheres, Part II. Sunlight reflected by terrestrial water clouds. J. Atmosph. Sci., 28, 1400-1426.

Harr, T. H. von der, and V. E. Suomi, 1971: Measurements of the earth's radiation budget from satellites during a five-year period. Part I: Extended time and space means. J. Atmos. Sci., 28, 305-314.

Harrison, E. F., P. Minnis, B. R. Barkstrom, V. Ramanathan, R. D. Cess, and G. G. Gibson, 1990: Seasonal variation of cloud radiative forcing derived from the earth radiation budget experiment. J. Geophys. Res., 95, D11, 18687-18703.

Hartmann, D. L., V. Ramanathan, A.Berroir and G.E. Hunt, 1986: Earth Radiation Budget Data and Climate Research., Rev. Geophys., 24, 439-468.

House, F.B., A. Gruber, G.E. Hunt, and Ann T. Mecherikunnel, 1986: History of Satellite Missions and Measurements of the Earth Radiation Budget (1957-1984). Review Geophysics, 24, 357-377.

Iribarne, J.V., and H.R. Cho, 1980: Atmospheric Physics, Reidel, Dordrecht Boston.

Jacobowitz, H., W. L. Smith, H. B. Howell, F. W. Nagle, and J. R. Hickey, 1979: The first 18 month of planetary radiation budget measurements from the Nimbus-6 ERB Experiment. J. Atmos. Sci., 36, 501-507.

Jacobowitz, H., H. V. Soule, H. L. Kyle, F. B. House, and the Nimbus-7 ERB Experiment Team, 1984: The Earth Radiation Budget (ERB) Experiment: On overview. J. Geophys. Res., 89, D4, 5021-5038.

Junge, C. E., 1963: Air Chemistry and Radioactivity., Academic Press, 382 pp.

Kandel, R. S., and J. P. Duvel, 1987: Diurnal variation of earth radiation budget components above Africa and the neighboring atlantic ocean; Changes between 1983 and 1985, estimated from Meteosat Observations adjusted to ERBS data, Adv. Spac. Res., 7, 3179-3186.

Kerschgens, M., E. Raschke, and U. Reuter, 1976: The absorption of solar radiation in model atmospheres. Beitr. Phys. Atmosph. , 49, 81-97.

Kneizys, F. X., E. P. Shettle, W.O. Gallery, J.H. Chetwynd, L.W. Abreu, J.Selby, R.W.Fenn, and R.A.McClatchey, 1980: Atmospheric transmittance/radiance, Computercode Lowtran-5, AFGL-TR-0067, Air Force Geophys. Lab., Bedford, Mass.

Koepke, P., 1983: Calibration of the VIS-Channel of Meteosat-2., Adv. Space Research, 2, 93-96.

Koepke, P. and K.T. Kriebel, 1978: Influence of measured reflection properties of vegetated surface on atmospheric radiance and its polarization., Appl. Optics, 17, 260-264.

Kriebel, K. T., 1979: Albedo of vegetation surfaces: Its variability with differing irradiances. Rem. Sens. of Env., 8, 283-290.

Kuriyan, J.G., and Z. Sekera, 1974: Scattering in liquid haze - analytical approximations, Quart. J. Roy. Meteorol. Soc., 100, 67-75.

Labs, D., and H. Neckel, 1968: The radiation of the solar photosphere from 2000 A to 100 um, Astrophys., 69, 1-75.

Liou, K.N. 1980: An Introduction to Atmospheric Radiation, Academic Press, New York, 392 pp.

Liu, Q., 1990: An analytical solution of transmission and reflection operators for homogeneous atmospheres. Beitr. Phys. Atmosph. , 63, 128-133.

Liu, Q., and J. Schmetz, 1988: On the Problem of an Analytical Solution to the Diffusivity Factor. Beitr. Phys. Atmosph.,61, 23-29.

Liu Q., C.Simmer and E.Ruprecht,1991:
A general analytical expression of the radiation source function for emitting and scattering media within the matrix operator method. Submitted to Beitr. Phys. Atmosph. .

Minnis, P., and E. F. Harrison, 1984a: Diurnal variability of regional cloud and clear-sky radiative parameters derived from GOES data, II, November 1978 cloud distribution
J. Clim. Appl. Meteorol., 23, 1013-1031.

Minnis, P., and E. F. Harrison, 1984b: Diurnal variability of regional cloud and clear-sky radiative parameters derived from GOES data, III, November 1978 radiative parameters.
J. Clim. Appl. Meteorol., 23, 1032-1051.

NASA 1985: Spectral Reflectances of Natural Targets for Use in Remote Sensing Studies. NASA Reference Publication No. 1139.

Nacke, G., 1989: Ableitung der Bodenalbedo aus METEOSAT - Daten. Berichte aus dem Institut fuer Meereskunde an der Universitaet Kiel, Nr. 190.

Neckel, H., and D. Labs, 1984: The solar radiation between 3300 and 12475 A. Solar Physics, 90, 205-258.

Plass, G. N., G. W. Kattawar and F. E. Catchings, 1973: Matrix operator theory of radiative transfer. 1. Rayleigh scattering. Appl. Optics, 12, 314-329.

PLatt C. M. R., and G. L. Stephens, 1980: The interpretation of remotely sensed high cloud emittances. J.Atmosph.Sci., 37, 2314-2322.

Potter, F. J., 1970: , The Delta Function Approximation in Radiative Tansfer Theory. J. Atmosph. Sci., 27, 943-949.

Quenzel, H., and Mueller H., 1978: Optical properties of single Mie particles: Diagrams of intensity, extinction, scattering and absorption efficiencies. Wissenschaftliche Mitteilung Nr. 34, University of Munich, Institute of Meteorology.

Ramanathan, V., R.D. Cess, E. F. Harrison, P. Minnis, B. R. Barkstrom, E. Ahmad, D. Hartmann, 1989: Cloud-Radiative Forcing and Climate: Results from the Radiation Budget Experiment. SCIENCE, 243,57-63.

Raschke, E., and W.R. Bandeen, 1970: The Radiation Balance of the Planet Earth from Radiatiom Measurements of the Satellite Nimbus-II. J. Appl. Met., 9, 215-238.

Raschke, E., T. H. Vonder Haar, W. R. Bandeen, and M. Pasternak, 1973: The annual radiation balance of the earth-atmosphere system during 1969-1970 from Nimbus-3 measurements. J. Atmos. Sci., 30, 341-364.

Rossow, W.B., Mosher, F., Kinsella, E., Arking, A., Desbois, M., Harrison, E., Minnis, P., Ruprecht, E., Seze, G., Simmer, C., and E. Smith, 1985: ISCCP cloud algorithm intercomparison, J. Clim. Appl. Meteorol., 24, 877-903.

Redheffer, R., 1962: On the relation of transmission-line theory to scattering and transter. J. Math. Phys., 41, 1-41.

Rieland, M., 1989: Stichprobenanalysen des Tagesganges der planetaren Strahlungsbilanz. Mitteilungen d. Ins. f. Geophysik u. Meteorologie der Universitaet Koeln, Heft 68.

Schanda, E., 1987: Physical Fundamentals of Remote Sensing. Springer-Verlag, 187 pp.

Schmetz, J., 1984: On the parameterization of the radiative properties of broken clouds. Tellus, 36A: 417-432.

Schmetz, J., 1986: An atmospheric-correction scheme for operational application to meteosat infrared measurements. ESA Journal, 10, 145-159.

Schmetz, J., 1989: Operational Calibration of the Meteosat water vapour channel by calculated radiances. Appl. Optics, 28, 3030-3038.

Schmetz, J., and Q. Liu, 1988: Outgoing Longwave Radiation and Its Diurnal Variation at Regional Scales Derived From METEOSAT. J. Geophys. Res., 93(D9), 11192-11204.

Schmetz, J., M. Mhita, and L. v de Berg, 1990: METEOSAT Observations of Longwave Cloud-Radiative Forcing for April 1985., J. Clim., 3, 784-791.

Simmer C., 1987: Application of Onedant to the Transport of Solar Radiation in the Earth's Atmosphere, LA-UR-87-2749, Los Almos National Laboratory.

Simmer, C., E. Raschke, and E. Ruprecht, 1982: A method for determination of cloud properties from two-dimensional histograms, Ann. Meteorol., 18, 130-132.

Slingo, A., R. C. Wilderspin, and S. J. Brentnall, 1987: Simulation of the diurnal cycle of outgoing longwave radiation with an atmospheric GCM. Mon. Wea. Rev., 115, 1451-1457.

Stephens, G.L., 1980: Radiative Properties of cirrus clouds in the infrared region. J. Atmosph. Sci., 37, 435-446.

Stone, Robert S., Graeme L.Stephens, C.M.R.Platt and S.Banks, 1990:
The Remote Sensing of Thin Cirrus Cloud Using Satellites, Lidar and Radiative Transfer Theory., J. Appl. Meteorol., 29, 353-366.

Stuhlmann, R., Wiegner, M., Knottenberg, H., Wirth, J. and D. Hennings, 1985: Calculations of the planetary albedo from satellite radiance measurements, Adv. Space Res., 5, 133-139.

Stum, J., B. Pinty, and D.Ramodo, 1985: A Parametrization of Broadband Conversion Factors for METEOSAT Visible Radiances., J. Clim. Appl.Meteorol., 24, 1377-1382.

Tomassini, C., 1981: Objective analysis of cloud fields, Proceedings of "Stellite Meteorology of the Mediterranean", ESA SP-159, 73-78, Europ. Space Agency, Paris, France

Ulaby, F. T., Richard K. M., and A. K. Fung, 1986:
Microwave Remote Sensing: Active and Passive, Volume II:
Radar Remote Sensing and Surface Scattering and Emission Theory.
University of California, Santa Barbara, U.S.A, 600 pp.

Van de Hulst. H. C., 1957: Light scattering by small particles, Wiley, New York, 470 pp.

Wiegner, M., and E. Raschke, 1987: Planetary Radiation Budget over North Africa from Satellite Data. Theor. Appl. Clim., 38, 24-36.

Wiscombe, W., and J. Evans, 1977: Exponential-sum fitting of radiative transmission functions. J. Comp. Phys., 24, 416-444.

World Climate Research Programme (WCP-55), 1983
Edited by Adarsh Deepak, Hermann E.Gerber,
Report of the Experts Meeting on Aerosols and their Climatic Effects.

Zdunkowski, W., and G. Korb, 1985:
Numerische Methoden zur Loesung der Strahlungsuebertrangungsgleichung
Promet, 2/3, 26-39.